

UNIVERSIDAD DE INGENIERIA Y TECNOLOGIA



**OPTIMIZATION OF CHAOTIC BIOPRINTING
TO PRODUCE REINFORCED
MULTICHANNEL HYDROGEL FIBERS FOR
THE MATURATION OF SKELETAL MUSCLE
TISSUE UNDER AGITATION**

THESIS

To obtain the Professional Engineering Degree in Bioengineering

AUTHOR

Andrea Cristina Cavero Arrivasplata 

ADVISORS

Julio Valdivia Silva 

Grissel Trujillo de Santiago 

Mario Moises Alvarez 

Lima - Peru

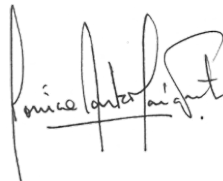
2024

DECLARACIÓN JURADA

Yo, Mónica Cecilia Santa María Fuster identificada con DNI No 18226712 en mi condición de autoridad responsable de validar la autenticidad de los trabajos de investigación y tesis de la UNIVERSIDAD DE INGENIERIA Y TECNOLOGIA, DECLARO BAJO JURAMENTO:

Que la tesis denominada “OPTIMIZATION OF CHAOTIC BIOPRINTING TO PRODUCE REINFORCED MULTICHANNEL HYDROGEL FIBERS FOR THE MATURATION OF SKELETAL MUSCLE TISSUE UNDER AGITATION” ha sido elaborada por la señorita Andrea Cristina Cavero Arrivasplata, con la asesoría de Julio Ernesto Valdivia Silva, identificado con el DNI N°23994395, Grissel Trujillo De Santiago identificada con el CURP TUSG840229MCLRNR00 y Marco Moisés Alvarez identificado con el CURP AAXM691015HCHLXR01 y que se presenta para obtener el grado de Bioingeniero, ha sido sometida a los mecanismos de control y sanciones anti plagio previstos en la normativa interna de la universidad, encontrándose un porcentaje de similitud de 1%.

En fe de lo cual firmo la presente.



Dra. Mónica Santa María Fuster
Directora de Investigación

En Barranco, el 2 de marzo de 2024

Dedication:

*To my father, Eduardo, for his advice and academic support.
To my mother, Hilda, for her wisdom and unconditional love.
To God, who has given me the best gifts in my studies and life.*

Acknowledgments:

I want to recognize the contributions of different people to this project. First, I want to say thank you to Dr. Grissel Trujillo de Santiago and Dr. Mario Moisés Álvarez from Instituto Tecnológico y de Estudios Superiores de Monterrey (ITESM) for allowing me to work in their laboratory and for being excellent academic mentors.

I would also like to recognize Dr. Johana Bolívar and Ph.D. candidate Carlos Ceballos for teaching me cell culturing and different cell staining techniques. Additionally, I want to recognize the work of Irving Rendón in the experimental section of my thesis as a volunteer, as well as Silvana Velásquez for her support in cell culturing.

In general, I would like to thank all the members of the Alvarez-Trujillo Laboratory of Tecnológico de Monterrey for their guidance and support.

A special acknowledgment to my teachers at Universidad de Ingeniería y Tecnología (UTEQ): Dr. Alejandra Ratti, for being the first teacher at the university to believe in me; Dr. Harry Saavedra, for encouraging me to continue my education; Dr. Paul Cárdenas, for encouraging me to present a project for the first time at a conference; and Dr. Julio Valdivia, for his academic guidance. Special thanks to Becas BCP for believing in my talent and financing my studies at UTEQ. Having their support was life-changing, both academically and personally.

A huge thanks to my father, who supported my stay in Mexico. Finally, I want to thank Ph.D. candidate Dariush Ebrahimibagha for introducing me to the research world, and for being my best friend and mentor during this time. His support was essential to the development of this work.

Contents

	Pág.
ABSTRACT	1
RESUMEN	2
INTRODUCTION	3
Presentation of the research topic	3
Description of the problem	4
Problem statement	6
Research Objectives	7
Justification	8
Scope and limitations	9
CHAPTER I CRITICAL LITERATURE REVIEW	10
1.1 3D bioprinting for skeletal muscle tissue engineering	10
1.2 Vascularization strategies using 3D bioprinting	14
1.3 Bioreactors for artificial tissue maturation	15
CHAPTER II THEORETICAL FRAMEWORK	19
2.1 Tissue Engineering	19
2.1.1 Skeletal muscle tissue engineering	20
2.2 Skeletal muscle	21
2.2.1 Structure of the skeletal muscle	22
2.2.2 Maturation of skeletal muscle cells	22
2.3 Vascularization	23

2.4	Biomaterials	24
2.4.1	Polymeric biomaterials	24
2.5	Scaffolds	24
2.6	Hydrogels	25
2.6.1	Mechanical properties of hydrogels	25
2.7	Hydrogel Fibers	26
2.7.1	Multichannel Hydrogel Fibers	27
2.7.2	Reinforced Multichannel Hydrogel Fibers	28
2.8	Cell culture	28
2.9	Bioreactor	29
2.9.1	Rocking bioreactor	29
2.10	3D Bioprinting	30
2.10.1	Stereolithography	31
2.10.2	Inkjet Bioprinting	32
2.10.3	Extrusion-based bioprinting	32
2.10.3.1	Co-extrusion bioprinting	33
2.10.4	3D Chaotic Bioprinting	33
2.11	Bioinks	34
2.11.1	Matrix bioinks	35
2.11.1.1	GelMA	35
2.11.2	Sacrificial bioinks	36
2.11.2.1	Hydroxyethyl cellulose	36
2.11.3	Structural bioinks	37
2.11.3.1	Sodium Alginate	37
2.12	Crosslinking	38
2.12.1	Photocrosslinking	39
2.13	Newtonian fluid	40
2.14	Non-Newtonian fluid	40

2.15 Viscosity	40
2.16 Shear Stress	41
2.17 Reynolds Number	42
2.18 Advection	42
2.18.1 Chaotic Advection	43
2.19 Static Mixers	43
2.19.1 Kenics static mixer	43
CHAPTER III METHODOLOGY	46
3.1 Printing protocols based on chaotic printing	47
3.1.1 KSM Printhead Design	49
3.1.2 KSM Fabrication	51
3.1.3 Preparation of inks	52
3.1.4 Chaotic printing of hydrogel fibers	54
3.1.5 Architectural Characterization	56
3.2 Optimization of mechanical properties	57
3.2.1 Chaotic printing of fibers	57
3.2.2 Tensile Tests	58
3.2.3 Statistical Analysis	61
3.3 Mass degradation of hydrogel fibers in a rocking bioreactor	62
3.3.1 Rocking Bioreactor Set-up	62
3.3.2 Printing of fibers for degradation experiments	64
3.3.3 Degradation of fibers	65
3.4 Evaluation of biological compatibility	66
3.4.1 2D Cell Culture	67
3.4.2 Bioinks preparation	69
3.4.3 3D Bioprinting with cells	70
3.4.4 Static 3D cell culture	72
3.4.5 Cell Viability experiments	72

3.4.6 Statistical Analysis	72
3.5 Cell alignment assesment	73
3.5.1 Actin/DAPI staining	74
3.5.2 Cell orientation assessment	74
3.6 Determination of cell viability in agitated culture	74
3.6.1 Three-D cell culture in a rocking bioreactor	75
3.6.2 Cell Viability experiments	75
3.6.3 Statistical Analysis	76
3.7 Ethical Considerations	76
CHAPTER IV RESULTS AND DISCUSSION	78
4.1 Development of printing protocols	78
4.1.1 Printhead fabrication	80
4.1.2 Chaotic printing of hydrogel fibers	82
4.1.2.1 For solid fibers of Alg(H) only	82
4.1.3 Printing hollow fibers of Alg(H) and HEC	83
4.1.4 Printing hollow fibers of Alg(H), GelMA/Alg(L), and HEC	83
4.1.5 Architectural Characterization	86
4.1.5.1 For solid fibers	87
4.1.5.2 For hollow fibers	89
4.2 Tensile Tests	90
4.2.1 The number of holes	91
4.2.2 The proportion of Alg(H) layers	93
4.2.3 The concentration of Alg(H)	94
4.3 Degradation of fibers under continuous agitation	97
4.4 Cell viability in static culture	99
4.4.1 Chaotic bioprinting	100
4.4.2 Cell viability assessment	101
4.5 Cell alignment in static culture	103

4.5.1 Cell spreading	104
4.5.2 Cell orientation	106
4.6 Cell viability in agitated culture	107
CONCLUSIONS	110
RECOMENDATIONS	112
APPENDICES	129

List of Tables

Table 3.1	Solutions used for experiments without cells	48
Table 3.2	Equipment used for experiments without cells	49
Table 3.3	Solutions used for experiments with cells	67
Table 3.4	Equipment used for cell culturing	68
Table 3.5	Equipment used for 3D chaotic bioprinting	71

List of Figures

Figure 2.1	Components of tissue engineering. Adapted from Valdivia-Silva (2020)	19
Figure 2.2	Tissue engineering approaches[36].	20
Figure 2.3	Structure of skeletal muscle tissue. Image by Lecturio.	21
Figure 2.4	Maturation of skeletal muscle cells[34].	22
Figure 2.5	Mechanisms of vascularization[43].	23
Figure 2.6	Some types of scaffolds[48].	25
Figure 2.7	Differences between a scaffold without vascular networks (i.e., a solid hydrogel fiber) and a scaffold with vascular networks (a multichannel hydrogel fiber resembles this structure)[54].	27
Figure 2.8	a) 2D cell culture and b) 3D cell culture. Adapted from lifeE-TIME CDT.	29
Figure 2.9	Rocking bioreactor. Adapted from [61].	30
Figure 2.10	Different 3D bioprinting strategies[66].	31
Figure 2.11	Chaotic Bioprinting. A. Co-extrusion of two inks through a KSM printhead. B. Geometry of a single KSM mixing element. C. Illustration of the inks division in a KSM printhead[5].	33
Figure 2.12	Composition of a bioink. Adapted from[75].	34
Figure 2.13	Types of bioinks. Adapted from Allevi.	35
Figure 2.14	Gelatin methacryloyl structure[80]	36
Figure 2.15	Hydroxyethyl cellulose structure[83]	37
Figure 2.16	Sodium alginate structure[87].	38

Figure 2.17	Crosslinking of polymeric chains[90].	38
Figure 2.18	Photocrosslinking of GelMA[80]	39
Figure 2.19	Deformation of a rubber block placed between two parallel plates under the influence of a shear force[95].	41
Figure 2.20	Advection of passive particles in an open flow setup with an obstacle[98].	43
Figure 2.21	The partitioned pipe mixer, an example of a static mixer[100].	44
Figure 2.22	KSM inducing chaotic advection for mixing two hydrogels[101].	44
Figure 3.1	Methodology schematic	46
Figure 3.2	Methodology schematic for specific objective N°1.	47
Figure 3.3	Conceptual design of the KSM printhead with 8 inlets and 2 mixing elements.	50
Figure 3.4	Steps for the KSM printhead fabrication.	51
Figure 3.5	Equipment used for KSM fabrication. Form 3+ Resin 3D printer from Formlabs (left) and Formlabs Form Wash to remove resin from the KSM (right).	51
Figure 3.6	Protocol for preparation of Alg _(H) 4% (w/v).	52
Figure 3.7	Protocol for preparation of Alg _(L) 7% (w/v).	53
Figure 3.8	Protocol for preparation of GelMA 3%/Alg _(L) 3.5% (w/v). . .	53
Figure 3.9	Protocol for preparation of HEC 0.6% (w/v).	54
Figure 3.10	Equipment used for chaotic printing. The multichannel pump was adapted for 8 syringes (left), and Omnicure S2000 was used for the photocrosslinking of GelMA (right).	55
Figure 3.11	Schematic representation of the chaotic bioprinting strategy implemented	55
Figure 3.12	Methodology schematic for specific objective N°2.	57

Figure 3.13	Tensile test machine made in the laboratory and its parts (left). Holding grips of the tensile machine with a hydrogel fiber as a sample (right).	59
Figure 3.14	KSM used to print hydrogel fibers with variations in $\text{Alg}_{(H)}$ proportion.	60
Figure 3.15	Methodology schematic for specific objective N°3.	63
Figure 3.16	DIY bioreactor system. A T25 flask was attached using a 3D-printed piece of resin to the magnet connected to the motor. . . .	63
Figure 3.17	Composition of control samples for degradation experiments. . .	65
Figure 3.18	Methodology schematic for specific objective N°4.	66
Figure 3.19	Bioprinting strategy for reinforced hollow fibers (treatment). . .	70
Figure 3.20	Bioprinting strategy for reinforced solid fibers (control).	71
Figure 3.21	Methodology schematic for specific objective N°5.	73
Figure 3.22	Methodology schematic for specific objective N°6.	75
Figure 3.23	3D Cell Culturing Conditions: static (left) and under constant agitation in a rocking bioreactor (right).	76
Figure 4.1	KSM design. a) 3D design of a KSM of eight inlets and two mixing elements. b) Adaptation of 3D KSM design in PreForm to ensure the structural conservation of the object during the printing process.	80
Figure 4.2	KSM just after the printing process was completed (left) and after washing with IPA to remove resin remains (right).	81
Figure 4.3	KSM printhead after removing scaffolds and photocuring (left). Top view (center). Helicoidal mixing elements (right)	81
Figure 4.4	Printing setup for solid hydrogel fibers. a) A multichannel sy- ringe pump with eight syringes loaded with $\text{Alg}_{(H)}$ 4%. b) Connection of silicone tubes with the eight KSM printhead inlets. c) Printhead inlets after printing.	82

Figure 4.5	Printing setup for hollow fibers with two inks. Left: A multi-channel syringe pump and syringes loaded with inks. Right: Printed fiber.	83
Figure 4.6	Chaotic bioprinting system for printing multi-material hollow channels. a) Loading of hydrogels inside the KSM. b) Multichannel syringe pump with loaded syringes connected to KSM during bioprinting. c) Hydrogels used for bioprinting. Alg _(H) is in red, GelMA is in yellow, and HEC is without color.	84
Figure 4.7	Crosslinking of multimaterial hollow fibers. Left: Crosslinking process. Right: Hydrogel fiber after crosslinking.	85
Figure 4.8	Multimaterial hollow fibers (without color).	85
Figure 4.9	Simulation of hydrogel layers arrangement in the head of KSM (left) and in the crosssection of the fiber (right). Courtesy of Diego Quevedo.	86
Figure 4.10	Hydrogel fibers of only Alg _(H) with inks proportion variations in the printing inlets. A comparison between conceptual and experimental results of the crosssections' architecture and inks' proportion is also shown.	88
Figure 4.11	Lateral view of a hollow fiber of Alg _(H) and HEC under the bright field and a green fluorescent channel.	89
Figure 4.12	Fluorescent microscopy images of a multimaterial hollow fiber.	90
Figure 4.13	Mechanical properties of hydrogel fibers with variations in the number of hollow channels. The stress-strain curve (left) and bar plot represent statistical significance between the elastic modulus values (right).	92
Figure 4.14	Bar plots representing statistical significance between strain values at break (left) and stress at break (right) of fibers with different numbers of holes.	92

Figure 4.15 Mechanical properties of hydrogel fibers with variations in the proportion of Alg _(H) layers. Stress-strain curve (left) and bar plot representing statistical significance between values of elastic modulus	93
Figure 4.16 Bar plots representing statistical significance between values of strain at break (left) and stress at break (right) of fibers with different proportions of Alg _(H) layers.	94
Figure 4.17 Mechanical properties of hydrogel fibers with different concentration of Alg _(H) . The stress-strain curve (left) and bar plot show the statistical significance between elastic modulus values (right).	95
Figure 4.18 Bar plots representing statistical significance between values of strain at break and stress at break of fibers with different concentrations of Alg _(H) .	96
Figure 4.19 Printed fibers for degradation experiments. Left to right: unreinforced solid fibers (control 1), reinforced solid fibers (control 2), unreinforced hollow fibers (control 3), reinforced hollow fibers (treatment).	97
Figure 4.20 Remaining weight of fibers in the first 72 hours of agitation in a rocking bioreactor.	98
Figure 4.21 Mouse myoblasts at 70% confluence	100
Figure 4.22 Bioprinting of the control sample (left). Bioprinting of the optimized-reinforced hollow fiber (right).	101
Figure 4.23 Chaotically bioprinted hydrogel fiber at day 1 (left). Embedded C2C12 cells in the hydrogel fiber (right).	101
Figure 4.24 Live/Dead staining of solid and hollow fibers in static culture at days 1, 7, and 14. Scale bar: 500 μm.	102
Figure 4.25 Statistical analysis of cell viability of fibers in static culture	102
Figure 4.26 Actin/DAPI of reinforced hollow fibers at days 7 and 14	105
Figure 4.27 Actin/DAPI of solid fibers at day 14	105

Figure 4.28 Actin/DAPI of reinforced hollow fibers at day 14	106
Figure 4.29 Actin/DAPI of reinforced hollow fibers at days 7 and 14	106
Figure 4.30 Live/Dead staining of solid and hollow fibers in agitated cul- ture at day 1 and 7.	108
Figure 4.31 Statistical analysis of cell viability of fibers in culture under agitation	108

List of Appendices

Appendix 1	129
Appendix 2	130
Appendix 3	131
Appendix 4	131
Appendix 5	132
Appendix 6	133
Appendix 7	133
Appendix 8	134
Appendix 9	135

List of Abbreviations

2D	Two-dimensional
3D	Three-dimensional
Alg	Alginate
<i>Alg_(H)</i>	High-viscosity alginate
<i>Alg_(L)</i>	Low-viscosity alginate
ANOVA	Analysis of variance
Anti-anti	Antibiotic/antimycotic
ASTM	American Society for Testing and Materials
C2C12	Mourin myoblast cells
CAD	Computer-aided design
CO₂	Carbon dioxide
DAPI	4',6-diamidino-2-fenilindol
DIY	Do-it-yourself
dH₂O	Distilled water

DMEM	Dulbecco's modified eagle medium
DMSO	Dimethyl sulfoxide
DPBS	Dulbecco's phosphate-buffered saline
ECM	Extracellular matrix
EtHD1	ethidium homodimer
dECM	Decellularized extracellular matrix
FBS	Fetal bovine serum
GelMA	Gelatin methacryloyl
HUVEC	Human umbilical vein endothelial cells
HEC	Hydroxyethylcellulose
IPA	Isopropyl alcohol
ITESM	Instituto Tecnológico y de Estudios Superiores de Monterrey
kPa	Kilopascals
KSM	Kenics Static Mixer
LAP	Lithium phenyl-2,4,6-trimethylbenzoylphosphinate
mRNA	Messenger RNA
PBS	phosphate-buffered saline
pH	Power of hydrogen
qPCR	Power of hydrogen
RNA	Ribonucleic acid

RT-qPCR Power of hydrogen

UTECH Universidad de Ingeniería y Tecnología

UV Ultraviolet

ABSTRACT

Chaotic bioprinting enables the fabrication of microstructured hydrogel fibers with co-extruding permanent and fugitive inks using a Kenics static mixer (KSM) printhead. However, these fibers degrade completely after 7 days of static culture. Survival of hydrogel constructs for prolonged periods is critical for tissue maturation. Therefore, in this project, chaotic bioprinting was optimized to reinforce multichannel hollow fibers, thereby extending the culture time to enable skeletal muscle tissue maturation. A KSM printhead equipped with eight inlets and two mixing elements was used to print hydrogel fibers with three materials: a bioink suitable to load cells, a sacrificial material to create hollow channels, and a structural material to provide mechanical stability (without cells). Each bioink layer was placed 62.5 μm apart from a hollow channel. Furthermore, the optimal ratio for each material was determined to enhance structural stability. The tensile test and degradation analysis indicated that the hydrogel fibers composed of 37.5% of the structural ink, 37.5% of the bioink and 25% of the sacrificial ink exhibited sufficient strength (elastic modulus = 12, 8 kPa) to conserve more than 75% of their mass after 72 h of continuous agitation in a rocking bioreactor. In contrast, the fibers containing no reinforcing ink entirely degraded in the same period or earlier. The bioprinting experiments also showed that mouse myoblasts adhering to the reinforced hollow fibers exhibited greater cell viability (95%) than myoblasts on reinforced solid filaments during 14 days of static culture. In the future, these reinforced multichannel fibers could mature musculoskeletal tissue with culturing under continuous agitation.

Keywords:

chaotic bioprinting; hydrogel fibers; hollow fibers; skeletal muscle; mechanical reinforcement; agitated culture.

RESUMEN

La bioimpresión caótica permite la fabricación de fibras de hidrogel microestructuradas. Esta consiste en coextruir una tinta permanente y una fugitiva a través de un cabezal de impresión Kenics Static Mixer (KSM). Sin embargo, estas fibras se degradan después de 7 días de cultivo estático. La supervivencia de los constructos de hidrogel durante períodos prolongados de tiempo es fundamental para la maduración del tejido. En este proyecto, se optimizó la bioimpresión caótica para reforzar las fibras huecas multicanal para prolongar el tiempo de cultivo. Para ello, se utilizó un cabezal de impresión KSM equipado con 8 entradas y 2 elementos de mezclado para imprimir con tres materiales: una biotinta para cargar células, un material sacrificable y un material estructural. Los filamentos se imprimieron variando la proporción de las tres tintas y su posición en el cabezal de extrusión sin comprometer la proporción de material estructural, el número de capas con células y acomodando microcanales huecos al menos cada $200\ \mu\text{m}$ de las capas con células. El ensayo de tracción y el análisis de degradación indicaron que las fibras de hidrogel que contienen $3/8$ de la tinta de refuerzo, $3/8$ de la biotinta y $2/8$ de la tinta de sacrificio exhiben suficiente resistencia (módulo de elasticidad = $12,8\ \text{kPa}$) para conservar más del 75% de su masa después de 72 h de agitación continua en un biorreactor oscilante. Por el contrario, las fibras que no contenían refuerzo se degradaron completamente en el mismo período de tiempo o antes. Los experimentos de bioimpresión muestran que los mioblastos de ratón adheridos a las fibras huecas reforzadas exhiben mayor viabilidad celular (un 95% más) que los mioblastos en filamentos sólidos durante 14 días de cultivo estático. En el futuro, estas fibras podrían utilizarse como plataforma para madurar tejido musculoesquelético con cultivo en agitación continua.

Palabras clave:

bioimpresión caótica; fibras de hidrogel; fibras huecas; músculo esquelético; refuerzo mecánico; cultivo en agitación

INTRODUCTION

Presentation of the research topic

Tissue engineering is an emerging, interdisciplinary branch of bioengineering that seeks to manufacture artificial human tissues. The term "tissue engineering" was first coined around 1980 by Joseph Vacanti and Robert Langer, who are considered the pioneers of this field. Nevertheless, after 40 years of research, functional three-dimensional (3D) tissues and organs have yet to be obtained. Specific properties are necessary for these tissues, such as being multicellular, vascularized, and mechanically stable[1]. Fabricating a tissue with all these properties is a challenge the scientific community must address.

Different biofabrication techniques have been developed to obtain artificial tissues, but 3D bioprinting has become the most popular strategy. This technology creates complex 3D constructs with live cells by depositing layers of bioinks. Hydrogels are polymeric biomaterials commonly used as bioinks because they can maintain a distinct 3D structure after deposition, provide mechanical support for the construct, and simulate the structure of the native extracellular matrix (ECM) for cell growth and proliferation[2]. 3D bioprinting has multiple advantages, including creating external and internal structures similar to natural biological tissues; creating flexible, targeted models; and minimizing waste with the help of computer software[3]. Additionally, a 3D structure model can be designed and printed with different bioinks according to its purpose to replicate native tissues and organs with higher accuracy.

One method to create 3D biological structures using multiple bioinks simultaneously is multimaterial 3D bioprinting. Among the different types of 3D bioprinting approaches, multimaterial chaotic 3D bioprinting has demonstrated its potential for

obtaining hydrogel fibers with different materials in one step. Hydrogels are non-Newtonian materials that can be extruded and mixed in layers through chaotic advection. Chaotic flows are predictable because they can be modeled through Navier-Stokes equations. They also present exponential growth due to their stretching and folding properties. These flows can generate sharp structures at the nanoscale and facilitate the creation of layers[4]. Mixing is possible with static mixers that use geometric reorientations to split and reconnect different materials. Kenics Static Mixer (KSM) is one static mixing tool adapted as a printhead in chaotic bioprinting. The KSM contains mixing elements that create inner-lamellar structures to print hydrogel fibers[5].

Description of the problem

In the global healthcare landscape, musculoskeletal conditions affect the mobility of the human body in patients worldwide. Musculoskeletal conditions include muscle atrophy, congenital disorders, musculoskeletal injuries, and volumetric muscle loss. Approximately 1.71 billion people worldwide have musculoskeletal conditions[6]. Globally, the proportion of prevalent cases due to categories of musculoskeletal disorders in 2017 was higher for low back pain (36.8%), followed by other musculoskeletal conditions (21.5%), osteoarthritis (19.3%), neck pain (18.4%), gout (2.6%), and rheumatoid arthritis (1.3%)[7]. Musculoskeletal disorders are a significant health concern in Peru, too. Just in 2017, around 2000 Peruvians over the age of 50 were hospitalized due to diseases of the musculoskeletal system and tissue [8]. Additionally, the demand for alternative treatments against musculoskeletal disorders is expected to increase in Peru during 2024. The market revenue is expected to be US\$219.40 million for new treatments, including surgical procedures for patients who require hospitalization due to degenerative diseases [9].

Due to insufficient tissue and organ donors worldwide, regeneration of skeletal muscle tissue seems to be a better approach to treating these conditions. Currently, a few strategies to stimulate skeletal muscle tissue regeneration exist, including satellite cell transplantation. Satellite cells (or muscle stem cells) are precursors of skeletal muscle cells, and they can differentiate into myoblasts that initiate skeletal muscle formation. Satellite cell transplantation involves inserting these cells into the patient to regenerate muscle tissue at a specific site. Although this strategy is promising, it does not guarantee entire regeneration in cases of volumetric muscle loss[10]. Another strategy is the insertion of muscle grafts, in which healthy muscle is taken from one body part and inserted into another that requires regeneration. Although this approach promotes regeneration after volumetric muscle loss, the post-operative phase typically consists of patients resting for an extended period. This makes recovery difficult because the lack of movement limits the skeletal muscle's natural ability to be restored structurally and functionally[11]. For this reason, there is a need for new strategies that facilitate muscle regeneration to facilitate the functional regeneration of tissue.

Among current biofabrication strategies that enhance tissue regeneration, 3D bioprinting is a promising technique for recreating human tissues with potential clinical applications. However, this strategy still has some challenges. For example, recreating the internal microarchitecture of the muscle accurately, including different cell types, blood vessels, and nerves, is a technical challenge. Therefore, most successful applications of skeletal muscle tissue bioprinting have not included vascularization. This can lead to limited cell growth, especially in printed constructs' cores or deep sections. While some attempts to create prevascularized constructs have been made, most techniques require post-processing steps that may damage cells and increase the risk of contamination due to the high sample manipulation[12]. Additionally, since tissue engineering and 3D bioprinting are emerging fields in Latin America, scientists trained in the topic are lacking, and specifically, only a few institutions

perform research in this field. This is due to the high cost of biofabrication technologies and the lack of investment in scientific research in the region. Therefore, some existing bioprinting strategies are challenging to replicate in Peru. Finally, high materials and equipment costs can create limitations for reproducibility and scalability in the long run.

Chaotic 3D bioprinting uses chaotic flow principles to obtain hydrogel and cell-laden fibers in a single step with high throughput. Although this technique has been proven effective at the nanoscale to fabricate prevascularized hollow fibers, it still faces some limitations. Hollow fibers made with this method lack mechanical stability; therefore, they are not resistant to erosion by flow and break easily under agitation conditions. To address this problem, researchers have attempted to use stiffer hydrogels as scaffolds. However, these rigid hydrogels are not a suitable environment for cells, which require porous surfaces to grow, expand, and proliferate adequately[13].

Problem statement

Bioprinting is a tool for replicating artificial tissue in the laboratory for tissue engineering applications. For example, it enables the creation of skeletal muscle fibers for treating patients with musculoskeletal disorders. Unlike traditional bioprinting, chaotic bioprinting is a one-step technique that can fabricate hydrogel fibers economically and at high throughput, including multichannel hollow fibers[14]. However, despite the benefits of creating void microchannels for vascularized constructs, the multichannel hollow constructs cannot withstand more than 7 days in static culture due to their poor mechanical stability[15].

The ideal maturation process involves agitation in a controlled environment (i.e., in a bioreactor), as agitation recreates what occurs inside the human body with fidelity. Moreover, bioreactors with agitation improve the perfusion of culture media

inside the void microchannels of the fiber, improving the mass transfer of nutrients to cells inside the construct, as well as cell growth and viability[16]. Therefore, a reinforced hydrogel fiber that can resist agitated culture for a prolonged period is needed. The most apparent approach to fabricating such a fiber is increasing the stiffness of the matrix. However, cells aggregate and cannot spread when seeded in a too rigid hydrogel. Thus, the mechanical properties of the construct, the hollow microchannels (which allow prevascularization), and the cells' ability to spread in the matrix must be optimized.

This research project proposes printing multi-material, compartmentalized scaffolds that gather different materials into one structure. Through this approach, this project aims to develop a biofabrication strategy based on chaotic advection that enables the production of mechanically resistant hollow hydrogel fibers. Combining three types of hydrogels (matrix hydrogels to load cells, structural hydrogels to provide mechanical support, and sacrificial hydrogels to create void microchannels) in one bioprinting-compatible structure will address this current gap in research regarding the need for longer-lasting hollow hydrogel fibers for skeletal muscle tissue engineering.

Research Objectives

Main objective

The main objective of this research is to optimize chaotic bioprinting for producing reinforced hollow hydrogel fibers that can sustain the maturation of skeletal muscle tissue under agitation.

Specific objectives

The specific objectives of the project are:

1. Develop protocols based on chaotic printing to create a multichannel fiber using structural, cell-adhesive, and sacrificial hydrogels.
2. Optimize the mechanical properties of the reinforced hollow fibers while preserving the maximum number of cell-adhesive layers.
3. Measure the degradation of reinforced and unreinforced hydrogel fibers under continuous agitation over time.
4. Evaluate the biological compatibility of reinforced hollow fibers in static culture over time.
5. Assess the cell alignment of skeletal muscle precursor cells on the reinforced hollow fibers in static culture over time.
6. Determine whether the agitated culture in a rocking bioreactor improves the cell viability of reinforced fibers over time.

Justification

Multimaterial chaotic bioprinting is a biofabrication technique that produces multi-material hydrogel fibers at a low cost and with high throughput. Using chaotic flows, it can utilize three types of inks (matrix, structural, and sacrificial) in a single construct to create fibers with a predictable microarchitecture. This technique solves the common problems faced in 3D bioprinting, such as expensive materials and equipment, recreation of human tissues' biological complexity, vascularization, structural integrity maintenance, and scalability. This project is expected to optimize this strategy by printing reinforced hollow fibers that sustain the maturation of skeletal muscle tissue under agitation. Additionally, this technique has the potential to be optimized for other types of tissue^[5] and other applications, such as the recreation of cancer microenvironments^[17]. Therefore, it is a promising technique for advancing tissue engineering and regenerative medicine.

Scope and limitations

The project aims to develop a bioprinting strategy as a proof of concept in a laboratory environment. Due to time limitations, the quantitative assessment of the cells when differentiated into mature tissue (which could be done using real-time PCR) is outside the previously stated objectives and should be addressed in future research. Additionally, it should be studied first in an animal model to ensure that the proposed reinforced hollow hydrogel fiber is safe for humans and can induce skeletal muscle tissue regeneration. However, this research is still in its initial stages, and the analysis of animals requires more resources that could be utilized in future steps of the project. Finally, to obtain artificial skeletal muscle tissue, its functionality must be evaluated. This would require incorporating other materials to induce electroconductivity in the fibers, something that is not considered in this project because of time and budgetary constraints.

The experimental section of this thesis project was developed in the Alvarez-Trujillo biomedical engineering laboratory of the Monterrey Institute of Technology and Higher Education (ITESM) in Monterrey, Mexico, for 10 months.

CHAPTER I

CRITICAL LITERATURE REVIEW

1.1 3D bioprinting for skeletal muscle tissue engineering

Although it is a promising alternative, 3D bioprinting is an emerging technology that still requires optimization for skeletal muscle tissue engineering. Various reports have outlined the fabrication of skeletal muscle-like tissue without vascularization, employing diverse bioprinting techniques and bioinks. Among different bioprinting techniques, extrusion bioprinting is the most common approach in current research.

Extrusion bioprinting enables the creation of skeletal muscle tissue with bundles and internal structures on the microscale. Fan et al. (2021) have demonstrated that 3D bioprinting of muscle cells in confined spaces enhances the maturation of skeletal muscle tissue. Using bioinks, such as gelatin and fibrinogen, they created muscle bundles with different widths[18]. Thinner structures improved myotube alignment, myogenic gene expression, and mechanical forces. Moreover, the cell viability (live cells) in three sample groups was more significant than 90%. Nonetheless, this method only showed these results with thin bundles. Therefore, an improved strategy should scale up the technique to obtain anatomically relevant muscle structures.

Lee et al. (2021) demonstrated the capacity of pneumatic bioprinting (a type of extrusion bioprinting) to produce self-aligned myofibers using a decellularized extracellular matrix (dECM)-based bioink. The bioink was made of porcine methacrylated dECM and polyvinyl alcohol (PVA) with embedded human primary

muscle cells[19]. This bioink provided biochemical and topographical cues that improved the muscle tissue’s contractile force while enhancing cell alignment. While the printing parameters and bioink formulation resulted in high cell viability (>90% in constructs of 100 μm), finding the optimal extrusion pressure to ensure good printing resolution and high cell viability was challenging[20]. Additionally, the method for providing topographical cues for cellular alignment limits the printing to a single direction, thereby preventing the creation of more complex tissues.

Another extrusion bioprinting strategy is chaotic bioprinting, which uses chaotic flows to fabricate hydrogel fibers. Frias et al. (2021) injected a millimeter-scale droplet of GelMA pre-gel with viral nanoparticles into glycerin and applied iterative two-dimensional (2D) chaotic flows to generate a hydrogel fiber. The addition of viral nanoparticles improved the cell alignment, metabolic activity, and cell adhesion of C2C12 cells, but the mechanical properties of the fibers were not evaluated. However, although viral nanoparticles are not toxic for humans, concerns regarding their safety do exist among patients and regulatory agencies, such as the Food and Drug Administration (FDA)[21]. Therefore, an ideal solution should not raise this biosecurity concern when scaled to pre-clinical and clinical assays.

Chaotic bioprinting has been adapted to fabricate hydrogel fibers with multiple layers. This can be achieved by co-extruding a bioink to serve as a cell matrix and another bioink to provide robustness and intercalate both layers. Bolivar et al. (2021) used 3D chaotic flows to fabricate muscle-like constructs that mimic the architecture of actual skeletal muscle tissue. Using a KSM printhead, they modulated the printing resolution by modifying the number of mixing elements in the printhead. The fibers showed high post-printing cell viability (more than 85%) after 28 days of culture, highly aligned microstructures constrained by arginylglycylaspartic acid (RGD)-free physical barriers, and expression of myosin and sarcomeric actin. However, nutrient perfusion was limited at the inner region of the filament due to

the fiber dimensions (approximately 1 mm diameter of solid hydrogel fiber without hollow microchannels)[14].

Hwangbo et al. (2022) used extrusion bioprinting and *in situ* crosslinking to develop a muscle construct with a bioink of cell-laden gelatin methacryloyl (GelMA) with murine myoblasts cells (C2C12). After GelMA was extruded from the printing nozzle, the *in situ* crosslinking system showed superior uniaxial alignment (with a high orientation factor) and density of cells in myogenesis compared to the conventional strategy (post-printing crosslinking). Furthermore, the constructs showed high cell viability (more than 90% on days 1 and 3), indicating that the ultraviolet (UV) light dose used was safe [22]. Nonetheless, performing *in situ* photocrosslinking during the bioprinting process increases the cost and complexity of this technique, as exposure to UV light can damage the skin. Finally, cell viability assays for at least 7 days must be conducted to determine UV light wavelength safety on cells.

Variations of traditional extrusion printing have been developed to overcome the limitations of conventional methods. For example, Lee et al. (2023) developed a novel bioprinting method—microvalve-assisted coaxial 3D bioprinting—to fabricate functional skeletal muscle tissue. The muscle tissue-like structure they created comprises a core filled with C2C12 cells and a hydrogel shell made of GelMA and glycidyl methacrylated hyaluronic acid. This bioprinting method allowed cell deposition with high cell viability (86%) at high throughput, responded to electrical stimulation, and represents histologically regenerated muscle tissue in rats. However, the viscosity of the bioink is limited to 200 Pa.s to avoid clogging the nozzle, which constrains the amount of bioink that can be extruded using this technique. Furthermore, samples with a cell strand showed necrosis on day seven in the core parts of the construct when compared to cell scraping[23]. Thus, the cell collection strategy should also be optimized to guarantee the high cell viability of the artificial muscle tissue.

Li et al. (2023) developed a novel extrusion-based 3D bioprinting method that uses a Carbopol support gel and a GelMA-Fibrinogen bioink to obtain muscle-like bundles with tunable stress relaxation. This system enabled high-resolution printing (around 100 μm), high efficiency in the differentiation and organization of oriented skeletal muscle bundles *in vitro*, and good biocompatibility and regeneration potential *in vivo*[24]. However, post-processing steps were required to remove the support gel to obtain the printed construct, which increases the process's overall time and the probability of contamination due to post-printing manipulation of the bundle. Additionally, exposure to UV light requires optimization to ensure cell safety.

Filippi and colleagues (2023) proposed an extrusion-based bioprinting method using permanent and sacrificial bioinks to obtain a perfusable, muscle-like structure with channels. Their technique ensured higher cell viability (more than 90%) in channeled constructs compared to solid ones due to improved mass transfer of nutrients. They used a GelMa-Alginate bioink, which offered mechanical and rheological properties suitable for tissue formation. The mature muscle-like constructs reached an elastic modulus of 14.7 kPa. Although the study showed promising results, long-term evaluation of the bioprinted muscle tissue and its functionality in clinical applications is still pending[25].

Lee et al. (2023) proposed optical fiber-assisted bioprinting (OAB) for efficient in situ crosslinking of methacrylated hydrogels. Optimized printing conditions, including UV light dose and processing temperature, ensured efficient crosslinking and the formation of mechanically stable structures with high cellular alignment and myogenic activity. Furthermore, the OAB process did not compromise cellular integrity or functionality and showed significant regenerative potential in a murine model. Some disadvantages of this method are high costs and complexity due to the optical fiber and cooling system required, as well as a lack of homogeneity

in the crosslinking process that can affect mechanical properties and multilayered constructs[26].

1.2 Vascularization strategies using 3D bioprinting

When tissue engineering was established as a new field of study, the need to create vascularized artificial tissues was addressed. Langer and Vacanti were the first to describe the characteristics of an ideal cell-polymer matrix. They proposed that this matrix should be prevascularized or become vascularized after immunization to ensure the transportation of nutrients[27]. Recent reports show that the most popular strategies to incorporate vascularization involve 3D bioprinting[28]. In bioprinting, the co-extrusion of two different bioinks enables the creation of complex structures and has been explored to recreate blood vessels in hydrogels.

For instance, Choi et al. (2019) co-extruded two tissue-derived bioinks (one loaded with muscle cells and the other with human umbilical vein endothelial cells (HUVECs)) to obtain prevascularized muscle constructs through coaxial bioprinting. This technique improved vascularization, promoted *de novo* muscle regeneration in an animal model, stimulated innervation, and showed low hypoxia levels in the construct's core parts. However, producing a larger construct was challenging due to the low viscosity and mechanical and resolution properties of the dECM bioinks[29]. Additionally, post-processing steps were required to remove the gelatin printing reservoir. As shown by this approach, vascularization requires recreating a blood vessel inside the muscle fiber and printing an anatomically relevant-sized tissue in a single step without compromising the construct's mechanical stability.

The co-extrusion of two bioinks was also explored by Cui and colleagues (2019)[30]. They utilized coaxial 3D bioprinting to create a small-diameter vascularity with a layered architecture, incorporating smooth muscle and endothelial

cells. This was achieved by employing catechol-functionalized methacrylate gelatin (GelMA/C) as the cell matrix. Despite obtaining a biomimetic structure, they did not achieve a vascular construct that was robust enough to connect blood circulation directly, and the printing system has yet to be optimized to produce relevant structures for clinical application. While blood vessel engineering can be achieved, these blood vessels must be incorporated into more complex tissues, and mechanical stability is still a problem.

Using sacrificial bioinks in extrusion bioprinting is an efficient mechanism for obtaining pre-vascularized, muscle-like structures. For example, Bolivar et al. (2022) co-extruded a cell-laden matrix (GelMA) and a sacrificial ink to fabricate thin hydrogel filaments with void microchannels. Using chaotic bioprinting, they printed fibers with C2C12 cells in a single step and at high throughput. The printed fibers contained multiple microchannels with diameters less than hundreds of micrometers. These hollow fibers showed greater viability (>90%) and metabolic activity than solid constructs, promoted the expression of a proliferation biomarker (Ki67), and improved cell alignment[15]. However, the fibers could not withstand more than 7 days of static culture because of mechanical instability in the microchannels' walls.

1.3 Bioreactors for artificial tissue maturation

Bioreactors have been widely applied in the biotechnology industry to improve the culture conditions of cells in suspension, and this concept has been transferred into tissue engineering. Instead of growing in suspension, the cells adhere to a biologically compatible scaffold suspended in the culture medium, enabling the formation of artificial tissues due to the accumulation of cells in a 3D matrix. Under cultivation in bioreactors, this technique is expected to improve control over cell growth parameters and the culture medium (for example, incorporating glucose or power of hydrogen

(pH) sensors). Furthermore, another advantage of exploring this approach is that bioreactors facilitate automation and scaling in tissue production.

Researchers have explored the feasibility of cultivation in bioreactors and how much it accelerates or benefits the formation of artificial tissue. One of the first findings on this topic was published by Freed, Vunjak-Novakovi, and Langer in 1993, who studied the formation of a cartilage implant in porous microscaffolds. They found that including micropores fulfills the function of blood vessels in native tissue since these empty cavities allow the transfer of nutrients throughout the 3D construct. Furthermore, they compared cell cultures in static and agitated bioreactors. They concluded that agitation culture (either by magnetic stirring or shaking) improved cell density and decreased cell doubling time compared to static culture[31]. Similarly, Freed described methods for culturing a single cell type and using a single material. However, the current challenge faced by skeletal muscle tissue engineering is creating templates using at least two materials to replicate the original architecture of the tissue and, ideally, the culture of two cells simultaneously. Despite Freed's promising findings, few subsequent reports have addressed cell culturing with stirred or shaking agitation.

Perfusion bioreactors have mainly been described as an alternative to passing culture medium with a constant flow to improve its absorption in 3D constructs. As Silva et al. (2020) demonstrated, additive manufacturing enables low-cost perfused bioreactors to be created for artificial tissue maturation. For example, a 3D-printed perfusion bioreactor was used to study the effect of shear stress on the chondrogenic differentiation of stem cells and human mesenchymal cells on porous poly(ϵ -caprolactone) scaffolds. The perfused and non-perfused constructs showed similar cell metabolic activity (approximately 30000 a.u. at day 21 for both samples). Cell viability was not assessed, but gene expression analysis showed that cell culture in the perfusion bioreactor had a higher expression of differentiation markers than that

in the non-perfused bioreactor[32]. The authors suggested that this system can be adapted to culture cells in hydrogels or electrospun fibers. However, the evaluation was conducted on a single-material scaffold, and the maturation of muscle fibers was not assessed.

To obtain vascular models, Liu and colleagues (2020) studied the maturation of HUVECs, mesenchymal stem cells (MSCs), and smooth muscle cells (SMCs) in a multilayer hydrogel using a 3D-printed bioreactor. A transparent polydimethylsiloxane (PDMS) bioreactor was connected to continuous infusion without complicated assembly. This strategy enabled the precise design of parameters such as lumens' length, thickness, and diameter and the completion of vascular constructs without sophisticated equipment[33]. Although the technique can theoretically be applied to the construction of nearly every tissue, the PDMS bioreactor is similar to a microchip, so scaling it up to the maturation of larger constructs can be challenging. Additionally, the study did not compare the behavior of cells with non-perfused hydrogels to determine whether the perfusion bioreactor was a better option for tissue maturation than static culturing.

Another strategy to induce perfusion involving agitation is a wave bioreactor. Nguyen et al. (2019) used porous gelatin microcarriers to expand human MSCs (hMSCs) in a wave bioreactor. The microcarriers showed higher growth and proliferation rates in a dynamic wave-type culture until day 40. Histological evaluations and live/dead staining were used to investigate the proliferation of static and dynamic culturing of cells. Cells in dynamic culture exhibited a doubled or greater proliferation rate than their static counterparts[34]. Nevertheless, a wave bioreactor system requires strict control and monitoring of various parameters, which can increase operational complexity. Despite the method's apparent benefits for cell expansion, the authors did not measure any maturation parameters in this study.

Without this information, the feasibility of this technology for fabricating artificial tissues is uncertain.

A rotating bioreactor can also induce constant perfusion for cell differentiation. Li et al. (2019) showed that a rocking bioreactor could differentiate MSCs into endothelial cells and vascular SMCs on an ECM scaffold. This dynamic culture system significantly increased cell differentiation efficiency compared to the static system, as evidenced by a higher expression of alpha-actin and smoothelin in the dynamic mode and high viability after 2 weeks of culture[35]. However, this study did not evaluate the maturation of skeletal muscle cells into artificial tissue.

Bioreactors with constant perfusion and agitation have demonstrated greater cell viability in most scenarios. Nevertheless, the use of bioreactors to grow multichannel hydrogel fibers with mechanical reinforcement has not yet been reported for the maturation of skeletal muscle tissue. This thesis shows, for the first time, the combination of these three parameters: mechanical reinforcement of a hollow hydrogel fiber with layers of structural material, growing cells in a reinforced hollow hydrogel, and 3D cell culturing of the reinforced hollow fibers in a rocking bioreactor for skeletal muscle tissue maturation.

CHAPTER II

THEORETICAL FRAMEWORK

2.1 Tissue Engineering

Tissue engineering is a branch of regenerative medicine, a subset of biomedical engineering. It is an interdisciplinary field of research that combines engineering principles and life science and uses cells, biomaterials, and biomolecules to replace or regenerate tissues and organs in patients. It seeks to fabricate functional tissues *in vitro* by using scaffolds as support for the cells to regenerate tissues in patients (Fig. 2.1).

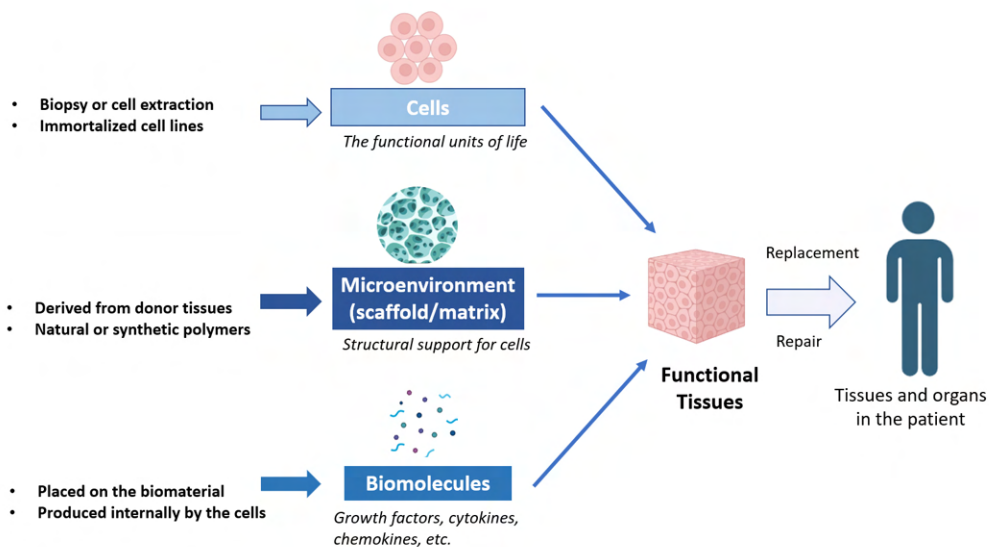


FIGURE 2.1: Components of tissue engineering. Adapted from Valdivia-Silva (2020)

2.1.1 Skeletal muscle tissue engineering

The final target of skeletal muscle tissue engineering is fabricating constructs where the cells can develop into contractile muscle cell precursors (myofibers). Engineering skeletal muscle tissue can be performed *in situ*, *in vivo*, or *in vitro*[36] (Fig. 2.2).

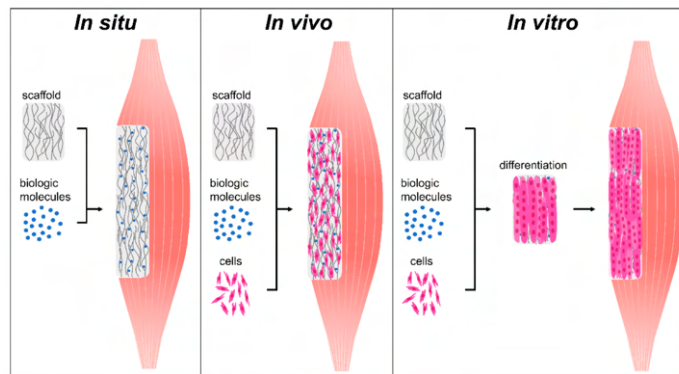


FIGURE 2.2: Tissue engineering approaches[36].

In situ tissue engineering promotes endogenous regeneration, as the scaffold can direct host cell recruitment, activation, proliferation, and differentiation by implanting an acellular biomaterial scaffold into the patient's wound. While *in situ* tissue engineering is the easiest method for scalability and clinical translation, it presents some limitations. For example, it has limited regeneration capabilities due to the absence of cells. Thus, this approach is inefficient when the lost tissue volume is too high and, therefore, unsuitable for tissue regeneration in patients with volumetric muscle loss.

In vivo tissue engineering is more challenging since it includes seeding cells on scaffolds before transplantation. *In vivo* tissue engineering is more efficient because the scaffold consists of cells participating in the regeneration process. While this method is effective since seeded cells participate in the regeneration process, it can also leave them vulnerable to immunological rejection and retention[37]. Scaling

up and translating this approach to clinical practice is also a challenge because, ideally, the cell-laden scaffold should be adapted to use each patient’s cells, leading to variability in the final product.

Finally, *in vitro* tissue engineering involves inducing tissue maturation in the laboratory. Functional tissue is created from cell-laden scaffolds using 3D cell culturing techniques, and the mature tissue is transplanted into the patient. It is the most efficient for volumetric muscle loss regeneration and enables disease and drug modeling. *In vitro* tissue engineering is the most challenging tissue engineering method because it involves complex techniques for assembling biomaterials, different cell types, and growth factors. Therefore, the scientific community is attempting to find new methods (such as 3D bioprinting) to recreate skeletal muscle tissue *in vitro*.

2.2 Skeletal muscle

Skeletal muscle is one of the three types of muscle tissue in the human body, and the structural units of skeletal muscle tissue are muscle cells (also known as muscle fibers). In contrast to smooth and cardiac muscle, skeletal muscle can be controlled by conscious commands from the brain. In other words, skeletal muscle conducts voluntary movements. Additionally, it provides mechanical strength to the entire body to maintain posture and stability in the joints[38].

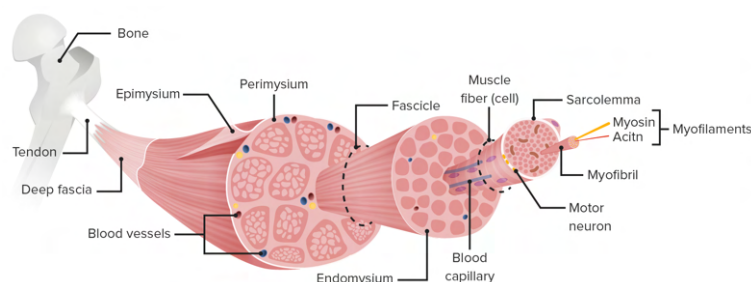


FIGURE 2.3: Structure of skeletal muscle tissue. Image by Lecturio.

2.2.1 Structure of the skeletal muscle

Skeletal muscles are attached to bones and tendons to contribute to the movement of the body's extremities. A skeletal muscle comprises several fascicles, or bundles of muscle fibers, and connective tissue intertwined with blood capillaries that provide nutrients and oxygenation (Fig. 2.3). Muscle cells are composed of myofibrils, organelles in charge of muscle contraction. Each myofibril is composed of bundles of complementary proteins known as myofilaments. The most critical myofilaments are actin and myosin because they work together in muscle contraction[39].

2.2.2 Maturation of skeletal muscle cells

Myoblasts are progenitor mononucleate cells that have the potential to differentiate into muscle fibers. They lack the distinctive myofilaments of muscle cells and cannot fuse with neighboring cells[40]. When myoblasts enter a differentiation process, they elongate due to an increased production of actin and myosin. Subsequently, they transform into myocytes. Myocytes then fuse into multinucleated cells as myotubes (Fig. 2.4). These myotubes continue undergoing maturation until they become functional myofibers, which are big enough to perform their contractile function adequately[41].

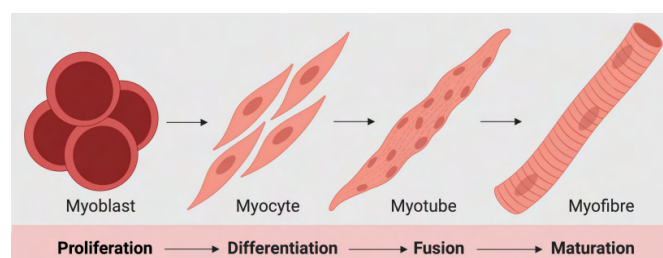


FIGURE 2.4: Maturation of skeletal muscle cells[34].

2.3 Vascularization

Vascularization is the blood vessel growth process in tissues. This process is vital because blood vessels improve the transfer of nutrients and communication between cells and other tissues (such as skeletal muscle tissue) and serve as a way to eliminate waste byproducts from the cells' metabolic activity.

Blood vessels, including arteries, arterioles, and capillaries, are of varying sizes. The distance between two capillaries surrounding a layer of cells cannot be more than $200\ \mu\text{m}$ due to the diffusion limitation of oxygen[42]. When this distance is greater, the cells from the core portion of tissues (especially in thick tissues) begin to die because they do not receive adequate nutrients or oxygen.

There are two mechanisms of vascularization: vasculogenesis and angiogenesis (Fig. 2.5). In vasculogenesis, blood vessels are formed *de novo* from precursor endothelial cells to create the main vascular networks in the human body. This process typically occurs during embryonic development. In angiogenesis, in contrast, secondary blood vessels are made from preexisting ones[43]. This process occurs continuously during adulthood whenever the regeneration of some tissue is required.

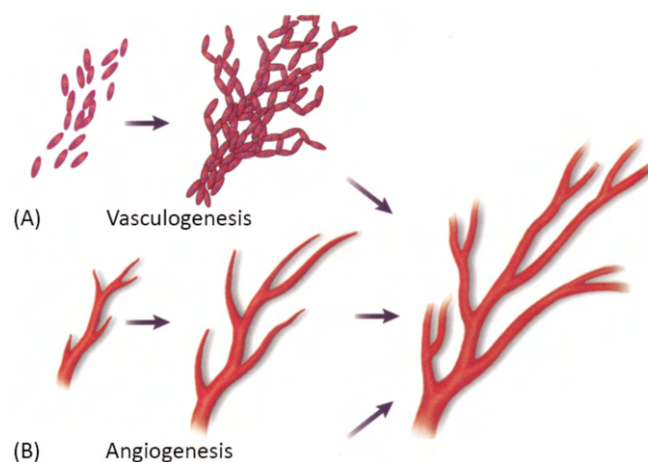


FIGURE 2.5: Mechanisms of vascularization[43].

2.4 Biomaterials

A biomaterial is any substance engineered to interact with biological components at a physiological level to cure, improve, or replace a tissue[44]. Biomaterials can be divided into different categories based on their composition: They can be natural or synthetic, and they can also be made of polymeric, metallic, ceramic, or composite materials.

2.4.1 Polymeric biomaterials

A polymeric biomaterial comprises chemical subunits of monomers that form more extensive polymer networks. Polymeric biomaterials are preferred for tissue engineering applications because they have tunable mechanical properties, are biodegradable, and can be personalized through surface modification to enhance their properties[45].

2.5 Scaffolds

Scaffolds are 3D structures composed of biomaterials that support the regeneration of tissues and organs. Their primary function is to provide a physical framework for cell growth. Scaffolds are typically made with polymeric biomaterials and come in different presentations like hydrogels, sponges, films, and fibers (Fig. 2.6). In applications involving the regeneration of bones, they can also be composed of minerals. Some scaffolds are made of "exotic" materials, such as eggshells, marine sponges, and vegetables[46].

Scaffolds can be designed and synthesized in the laboratory to improve tissue regeneration. These scaffolds can recreate an artificial microenvironment that resembles the ECM of native tissue. They must combine biophysical cues (such as

topography, porosity, and dynamics) and biochemical cues (like bioactive chemicals) to guarantee optimal regeneration of the tissue[47].

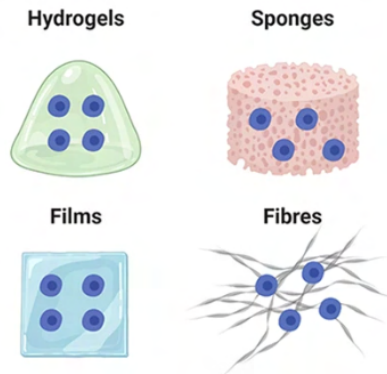


FIGURE 2.6: Some types of scaffolds[48].

2.6 Hydrogels

Hydrogels are gel-like materials comprising a 3D network of hydrophilic polymers dispersed in water or a comparable aqueous solution. They can absorb and retain significant volumes of water while retaining structural integrity[49]. Hydrogels are highly adaptable and may be manufactured with various physical qualities, such as stiffness, elasticity, and porosity, making them appropriate for a wide range of applications. They are used in tissue engineering, drug delivery systems, wound dressings, and biosensors, among others[50]. Hydrogel synthesis involves pre-gel preparation in a polar solvent (i.e., distilled water (dH_2O)) and the subsequent crosslinking of polymeric chains.

2.6.1 Mechanical properties of hydrogels

Mechanical properties are those properties shown by any biomaterial when forces are applied. In the case of hydrogels, the most important mechanical properties

are elasticity, compressibility, and stiffness, which determine the material's ability to deform, compress, and resist deformation. Furthermore, these properties can be assessed with a universal tensile machine to obtain the Young's modulus of a material under various stress conditions[51].

Understanding the material's mechanical properties in tissue engineering is essential to knowing the similarity between one biomaterial and a native tissue or organ. Ideally, the mechanical properties of the hydrogels should be similar to those of the tissue to be replaced or regenerated. Additionally, identifying these properties helps understand cell behavior in cell-laden materials. Finally, they indicate whether the material possesses adequate mechanical stability to function correctly.

2.7 Hydrogel Fibers

Hydrogel fibers are hydrogels in a fibrous state. In tissue engineering, hydrogel fibers replace skeletal muscle tissues, nerves, blood vessels, and other structures with an elongated shape. They can be produced by fabrication methods such as electrospinning and chemical crosslinking after 3D bioprinting.

The mechanical properties of a hydrogel fiber can be assessed through tensile assays. The compatibility of hydrogel fibers with tensile test is attributed to their elongated geometry. Tensile tests consist of exposing hydrogel fibers to uniaxial stretch until they break. Results from tensile tests can vary according to the fiber's condition. The elastic modulus of a hydrogel fiber, typically measured in kilopascals (kPa), can vary based on whether the hydrogel is wet or dry[52].

Hydrogel fibers can be solid or hollow. Solid fibers have a continuous structure and consistency in their cross-section, while hollow fibers possess at least one hole in their structure, surrounded by hydrogel walls. The holes can be seen under the microscope by observing a cross-section.

2.7.1 Multichannel Hydrogel Fibers

A type of hollow fiber, multichannel hydrogel fibers are hydrogels in a fibrous state with multiple void microchannels inside the structure. Besides possessing holes, they have various compartments of different materials that are layered together into one structure. These fibers can be fabricated with sacrificial materials, which are removed after the printing process, are removed to leave holes inside the construct[53].

Multichannel hollow fibers have higher cell viability than solid fibers. Solid fibers have cell viability on their surface but a necrotic core. Meanwhile, higher cell viability in hollow fibers is due to the void spaces that simulate the function of blood vessels and allow perfusion in the core parts of the structure[15]. Therefore, these fibers enable the improved mass transfer of nutrients in thick scaffolds (Fig. 2.7). Additionally, multichannel hydrogel fibers are an ideal platform to induce vascularization inside the void spaces, thereby improving tissue maturation *in vitro*.

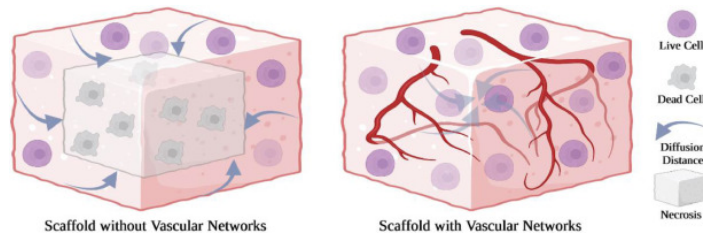


FIGURE 2.7: Differences between a scaffold without vascular networks (i.e., a solid hydrogel fiber) and a scaffold with vascular networks (a multichannel hydrogel fiber resembles this structure)[54].

However, these multichannel hydrogel fibers do not possess mechanical stability, and their Young's modulus is lower than that of solid hydrogel fibers. This limitation renders 3D cell culturing difficult for extended periods and nearly impossible in culture conditions that involve continuous agitation[15]. The poor mechanical

stability of these fibers also raises concerns about their applicability in regenerating tissues exposed to constant movement, such as skeletal muscle tissue.

2.7.2 Reinforced Multichannel Hydrogel Fibers

Reinforced multichannel fibers are hollow fibers that are mechanically reinforced. Different methods have been used to improve the mechanical stability of hollow fibers, including multimaterial bioprinting to include a structural material (such as alginate) as an additional layer in the structure [14], the synthesis of composed hydrogels[55], the addition of dECM[56], and the addition of nanoparticles inside the hydrogel[57].

2.8 Cell culture

Cell culture is a laboratory technique that allows the growth of cells in vitro. It enables the development of isolated cells or characterized cell lines in a controlled environment that preserves the physiological conditions of temperature, pH, and carbon dioxide (CO₂). A critical component in cell culture is the culture medium, which provides all the amino acids, nutrients, salts, and growth factors needed by the cells[58].

Cell culture can be performed two or three-dimensionally (Fig. 2.8). 2D cell culture can be conducted in Petri dishes or flasks and is used to cultivate adherent cells that require a surface to attach. 2D cell culturing is the traditional cell culture method used in tissue engineering to expand cells until a desired concentration is reached for other experiments. In contrast, 3D cell culture cultivates cells on a 3D scaffold. The 3D environment allows the cells to have a spatial arrangement that replicates their physiological conditions in tissues and organs with more fidelity. This technique differs from the traditional cell culture method and is more suitable for

disease modeling, artificial tissue maturation, and drug delivery experiments[59].

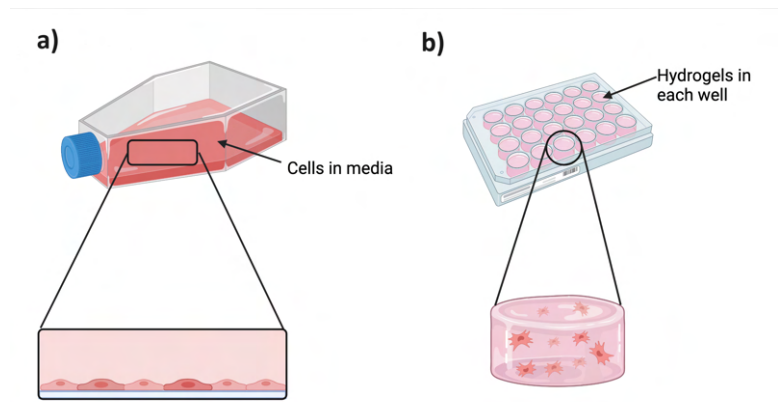


FIGURE 2.8: a) 2D cell culture and b) 3D cell culture. Adapted from lifETIME CDT.

2.9 Bioreactor

A bioreactor is a vessel used in biotechnology that provides a controlled environment for the biological activity of cells, bacteria, and yeast. Cultivating cells, or microorganisms, in a bioreactor aims to transform a substrate into products and bioproducts while scaling up the entire process for industrial applications. In tissue engineering, bioreactors are used to cultivate stem cells and as part of the maturation process of artificial tissues.

2.9.1 Rocking bioreactor

Rocking bioreactors operate with a gentle rocking motion, moving from one side to the other continuously (Fig. 2.9). This rocking motion helps the culture medium perfuse inside the void microchannels of porous or hollow scaffolds to improve the

mass transfer of nutrients and oxygenation. The advantage of working with a rocking bioreactor is that it induces low shear forces that do not damage the cells or the scaffold[60].

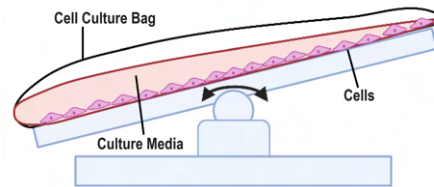


FIGURE 2.9: Rocking bioreactor. Adapted from [61].

Other types of bioreactors also provide agitation. For example, the spinner-flask bioreactor creates agitation by rotating its helixes. However, this agitation is not uniform, and the shear stress varies with the volume of the bioreactor[62]. Therefore, a spinner-flask bioreactor may not be optimal for tissue engineering applications, as it can expose cells in certain areas to high shear stress and destroy scaffolds with mechanical agitation. Gentle and uniform agitation is preferred for the continuous maturation of tissues, which can only be achieved through 3D cell culture in a rocking bioreactor[63].

2.10 3D Bioprinting

Three-D bioprinting uses 3D printing techniques to combine cells, growth factors, and biomaterials to fabricate biomedical parts, often to imitate natural tissue characteristics. Generally, 3D bioprinting can utilize a layer-by-layer method to deposit materials known as bio-inks to create tissue-like structures used in various medical and tissue engineering fields[64]. Currently, bioprinting can print tissue and organ models for researching drugs and potential treatments[65]. Some types of 3D

bioprinting include inkjet bioprinting, extrusion bioprinting, and stereolithography (Fig. 2.10).

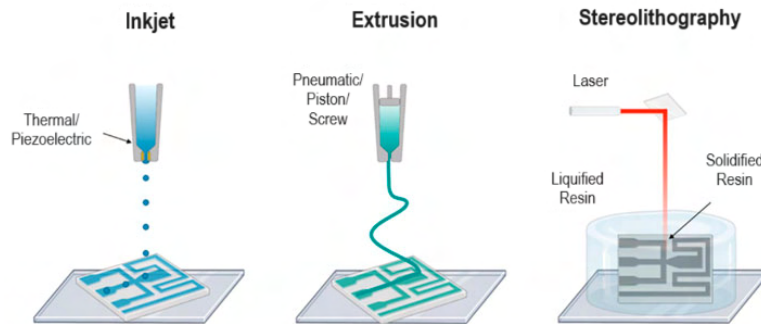


FIGURE 2.10: Different 3D bioprinting strategies[66].

2.10.1 Stereolithography

Stereolithography (SL) is an additive manufacturing technique that uses a UV laser to cure layers of liquid resin to create 3D objects. The primary mechanism of SL is projecting a light beam onto the surface of photocurable liquid resin using a UV laser and a directed mirror array. To create the 3D pieces, this light beam is repeatedly projected along the vertical axis in each layer. The primary drawback of SL is the UV light source, which damages cells and leads to skin cancer[67]. A substitute is visible light SL, developed in bioprinting by optimizing and stabilizing the printed scaffolds [68]. Standard printing methods typically result in porous networks with weakly constructed 3D scaffold structures. Light-sensitive bioinks help to build the structure because SL bioprinting relies on a specific light source to govern printing. Consequently, the bioinks are deposited plane by plane[69].

2.10.2 Inkjet Bioprinting

The use of 2D desktop inkjet printers allows for the non-contact technique of inkjet-based bioprinting. Piezoelectric inkjet bioprinting, thermal inkjet bioprinting, and electrostatic inkjet bioprinting are the three main categories of this technique[70]. A piezoelectric actuator produces acoustic waves through the bioink chamber in piezoelectric inkjet bioprinters. A voltage pulse is created for electrostatic inkjet bioprinters to form droplets by exerting pressure between a pressure plate and an electrode. Heat is produced in the bioink chamber in thermal inkjet bioprinting, causing pressure to build. Although the fabrication method relies on producing ink droplets, the demand for this bioprinting method has grown due to their reasonable cost and biocompatibility[71].

2.10.3 Extrusion-based bioprinting

Extrusion-based bioprinting, often called direct ink writing, has a significantly increased use in tissue engineering and biofabrication [72]. Based on two fundamental mechanisms, pneumatic force (gas or pressurized air) and mechanical force, the extruded bioinks are distributed broadly (screw or piston). The bioinks are applied to a building substrate, and a screw-driven mechanism controls the bioink overflow during the piston-driven deposition setup. This bioink overflow process is essential for depositing high-viscous biomaterials[71].

A computer-aided design (CAD) file is imported into fabrication as a .stl file and printed according to the specified structure. In contrast, due to machine developments, some printheads can now deposit multiple bioinks while controlling porosity, shaping, and the distribution of cells in the manufactured parts. Extrusion-based bioprinting enables the deposition of large cell densities and various printable materials.

2.10.3.1 Co-extrusion bioprinting

Co-extrusion bioprinting is a technique in which two or more bioinks can be simultaneously extruded to create multimaterial structures. Ideally, all the materials should possess different mechanical and biological properties. In this way, they can create heterogeneous tissues with different layers and a higher level of complexity. Additionally, this approach enables printing two or more cell types simultaneously to imitate their organization in native tissue accurately.

2.10.4 3D Chaotic Bioprinting

Continuous chaotic bioprinting uses a simple laminar chaotic flow induced by a static mixer to create delicate, complex structures at the micrometer and submicrometer levels within polymer fibers[5] (Fig. 2.11). Chaotic flows are used to mix in the laminar regime, where low speed and high viscosity conditions preclude turbulence to achieve homogeneity. However, a much less exploited characteristic of chaotic flows is its potential to create defined multi-material and multi-lamellar structures[73].

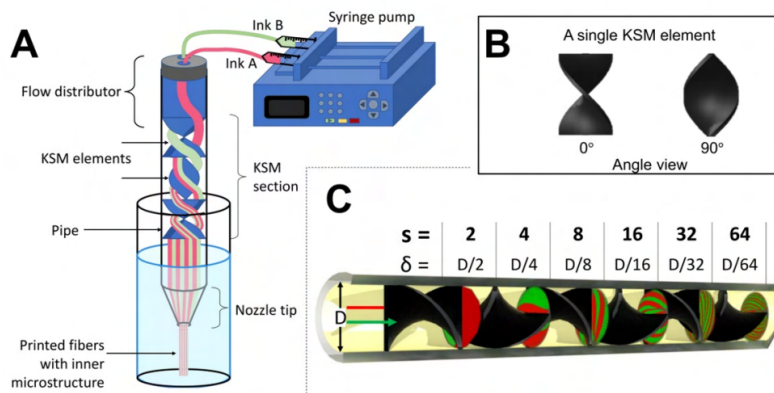


FIGURE 2.11: Chaotic Bioprinting. A. Co-extrusion of two inks through a KSM printhead. B. Geometry of a single KSM mixing element. C. Illustration of the inks division in a KSM printhead[5].

2.11 Bioinks

Bioinks are materials in 3D bioprinting processes to fabricate artificial tissues and organs. A bioink is the foundation for bioprinting procedures because it enables the exact layering of cells, biomaterials, and biomolecules to construct functional living scaffolds (Fig. 2.12). The distinct composition of a bioink enables it to provide structural support while preserving the printed cells' viability and functionality, making it an essential component for tissue engineering, regenerative medicine, and organ transplantation[74].

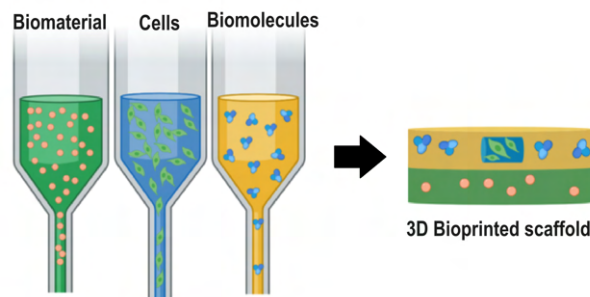


FIGURE 2.12: Composition of a bioink. Adapted from[75].

Some essential features of an ideal bioink material are bioprinting ability, high mechanical integrity and stability, insolubility in the cell culture medium, biodegradability at a rate appropriate to the regenerating tissue, non-toxicity and non-immunogenicity, and the ability to promote cell adhesion[76]. Three types of bioinks are used for bioprinting in tissue engineering: matrix bioinks, sacrificial bioinks, and structural bioinks (Fig. 2.13).

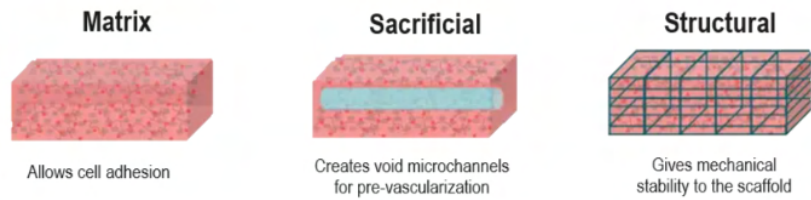


FIGURE 2.13: Types of bioinks. Adapted from Allevi.

2.11.1 Matrix bioinks

Matrix bioinks are cell-friendly bioinks in which cells are attached during bioprinting and posterior 3D cell culturing. The properties of these bioinks are similar to those of the ECM, which guarantees optimal cell adhesion and spreading. To achieve optimal print resolution, matrix bioinks must shield cells from shear stresses during printing, closely mimic the ECM, and offer quick, nontoxic gelation[77]. Matrix materials will also be introduced in this text as cell-adhesive materials because they allow cell adhesion and growth.

2.11.1.1 GelMA

GelMA is a semi-synthetic material derived from gelatin. Unlike common gelatin hydrogels, the gelatin amine groups in GelMA have been chemically modified by a process called methacrylation (Fig. 2.14). GelMA hydrogels have a high cell viability due to their porosity and composition resembling the ECM. Moreover, GelMA is favorable for cell growth, as it has a high similarity to the ECM due to the presence of RGD motifs that mediate cell attachment in the native ECM, allowing cell spreading of different types of cells[78],[79].

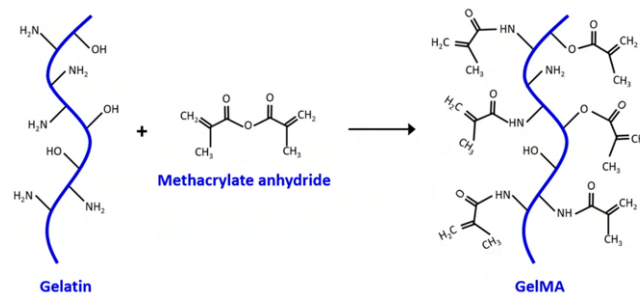


FIGURE 2.14: Gelatin methacryloyl structure[80]

2.11.2 Sacrificial bioinks

Sacrificial bioinks can offer temporary support or can be used to create complex geometries within a structure for vasculature networks. Ideally, a sacrificial bio-material offers high print fidelity, cytocompatibility, and ease of removal. Using sacrificial bioinks in bioprinting aims to leave space for hollow structures that lead to vascularized, perfusable channels that resemble real tissue[81].

2.11.2.1 Hydroxyethyl cellulose

Hydroxyethyl cellulose (HEC) is a natural water-soluble polymer derived from cellulose. It is obtained by treating cellulose with sodium hydroxide and reacting it with ethylene oxide. Since this modification increases water retention, HEC can be used as a hydrogel. Furthermore, HEC is highly soluble in water. Therefore, it has been used as a sacrificial material to fabricate prevascularized scaffolds[82]. Besides its applications in tissue engineering, HEC can be used as a stabilizer and thickening agent in the food, cosmetic, and pharmaceutical industries. The chemical structure of HEC is depicted in Fig. 2.15

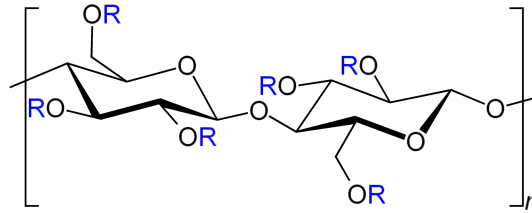


FIGURE 2.15: Hydroxyethyl cellulose structure[83]

2.11.3 Structural bioinks

Structural bioinks enhance the mechanical properties and structure of scaffolds. These materials are most valuable when developing tissues that require higher mechanical strength, such as bone or cartilage. Because they have a higher stiffness than matrix hydrogels, they are not always loaded with cells, and in the case of skeletal muscle cell precursors, their high stiffness does not allow cell spreading[84].

2.11.3.1 Sodium Alginate

Sodium alginate is a natural hydrogel derived from brown algae and is the sodium salt of alginic acid. It has an anionic linear polysaccharide with hydroxyl and carboxyl groups attached to its backbone (Fig. 2.16). Sodium alginate is widely used in tissue engineering as a scaffold and can be found commercially with different viscosities[85]. High-viscosity alginate ($\text{Alg}_{(H)}$) is preferred when the goal is to encapsulate cells and create a hydrogel with good mechanical stability. This type of alginate can be used as a structural material to improve the mechanical properties of hydrogel fiber. In contrast, low-viscosity alginate ($\text{Alg}_{(L)}$) is preferred for cell spreading and higher cell viability. It has lower mechanical stability compared to high-viscosity alginate[86].

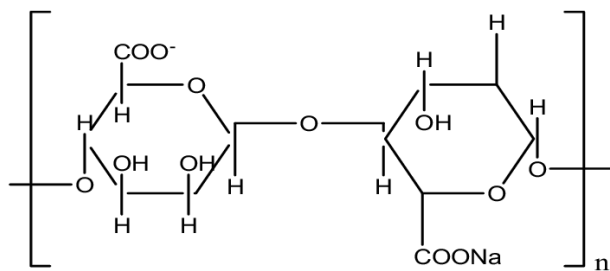


FIGURE 2.16: Sodium alginate structure[87].

2.12 Crosslinking

Crosslinking is a stabilization process that extends polymeric chains, resulting in network structures. Through crosslinking, hydrogels are formed into stable structures that differ from their raw materials[88] by using heat, UV light, or a crosslinking agent (Fig. 2.17). Crosslinking agents (crosslinkers) chemically bind polymeric chains to create hydrogels. For example, calcium chloride (CaCl_2) is a crosslinker that connects polymeric chains due to the binding of calcium ions to functional groups with a negative charge[89].

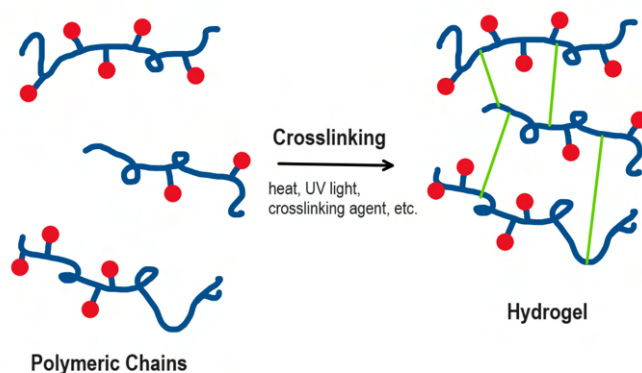


FIGURE 2.17: Crosslinking of polymeric chains[90].

2.12.1 Photocrosslinking

Photocrosslinking is a crosslinking method using UV light to bond polymeric chains chemically. Depending on whether cells are included in the utilized bioinks, the UV exposure time and photoinitiator concentration must be adjusted to attain an acceptable polymer crosslink. Thus, photocrosslinking enables a rapid crosslinking process.

A photoinitiator compound is necessary to make a polymeric solution sensitive to light for photocrosslinking. For example, lithium phenyl-2,4,6-trimethylbenzoylphosphinate (LAP) is a cytocompatible photoinitiator usually added to a bioink for 3D bioprinting. After adding LAP, the bioink is exposed to UV light, and a hydrogel scaffold is created as a result of photocrosslinking[91].

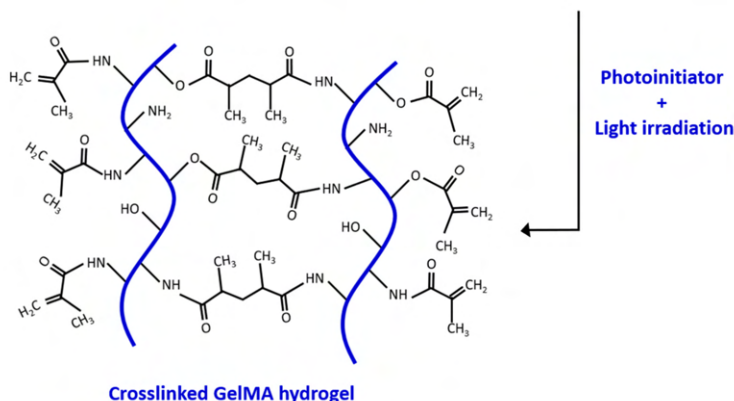


FIGURE 2.18: Photocrosslinking of GelMA[80]

Different chemical functional groups, including methacryloyl groups, have been conjugated to natural polymers to make them photocrosslinkable, allowing the mechanical properties of natural polymers to be precisely tuned. Examples of these polymers include GelMA (Fig. 2.18), hyaluronic acid methacrylate, carboxymethyl cellulose methacrylate, glycidyl methacrylate, oxidized methacrylate alginate (OMA), and methacrylate alginate[92].

2.13 Newtonian fluid

A Newtonian fluid is characterized by a linear correlation between the viscous stresses resulting from the fluid's flow and the local strain rate—the rate of change of the fluid's deformation over time[93]. Stresses are proportional to the rate of change of the fluid's velocity vector. In other words, a Newtonian fluid has a constant viscosity value independent of the shear rate. Some examples of Newtonian fluids are water, honey, and oil.

2.14 Non-Newtonian fluid

A non-Newtonian fluid is a fluid that does not follow Newton's law of viscosity. In non-Newtonian fluids, viscosity can change when under force to be more liquid or solid. Most commonly, the viscosity of non-Newtonian fluids (i.e., the gradual deformation by shear or tensile stresses) depends on their shear rate or shear rate history[93]. One example of a non-Newtonian fluid is hydrogels, commonly used in regenerative medicine and 3D bioprinting.

2.15 Viscosity

The viscosity of a fluid is a measure of its resistance to deformation at a given rate. In general, viscosity depends on a fluid's state, such as its temperature, pressure, and deformation rate. However, the dependence on some of these properties is negligible in some instances. For example, the viscosity of Newtonian fluids remains constant despite changes in temperature, pressure, or shear rate[94].

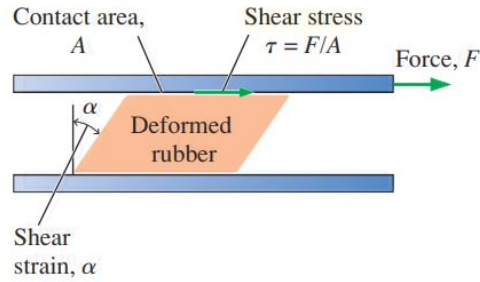


FIGURE 2.19: Deformation of a rubber block placed between two parallel plates under the influence of a shear force[95].

2.16 Shear Stress

Shear stress is the component of stress coplanar with a material cross-section. A fluid deforms continuously under the influence of shear stress, ultimately approaching a constant strain rate when a constant shear force is applied. A visual description of shear stress is described in Fig. 2.19 with the example of a deformed rubber. Mathematically, the shear stress is expressed as:

$$\tau = F/A, \quad (\text{II.1})$$

where τ is shear stress (Pa), F is force (N), and A is Area (m^2)[95].

For a one-dimensional shear flow of Newtonian fluids, shear stress can be expressed by the following equation:

$$\tau = \mu \cdot \frac{du}{dy}, \quad (\text{II.2})$$

where τ is shear stress (Pa), μ is the dynamic viscosity of the fluid (Pa.s), and du/dy is the velocity gradient[95].

2.17 Reynolds Number

The Reynolds number is a dimensionless number used in fluid mechanics to characterize the movement of a fluid. Changes in flow patterns can be predicted with this number.

Laminar flow occurs at low Reynolds numbers, where viscous forces dominate, and is characterized by smooth, constant fluid motion. In contrast, turbulent flow occurs at high Reynolds numbers and is dominated by inertial forces, which tend to produce chaotic eddies, vortices, and other flow instabilities[96]. Chaotic flows can lead to elastic flow instability at Reynolds numbers well below the transition number ($Re = 2000$) for turbulence flow[97].

2.18 Advection

Advection refers to the transport of a particle by fluid from one region to another due to the fluid's horizontal bulk motion[97]. The term "passive advection" is used to specify that the particle moving with the fluid has so little mass that it cannot interfere with the flow; instead, it adjusts its velocity to the flow (Fig. 2.20). To simplify this statement, advection can be described as follows:

$$\vec{V}_{\text{fluid}} = \vec{V}_{\text{particle}} \quad (\text{II.3})$$

The velocity of this passive particle is given by the rate of its position in a 3D space:

$$V_{\text{particle}} = \left(\frac{dx}{dt}, \frac{dy}{dt}, \frac{dz}{dt} \right) \quad (\text{II.4})$$

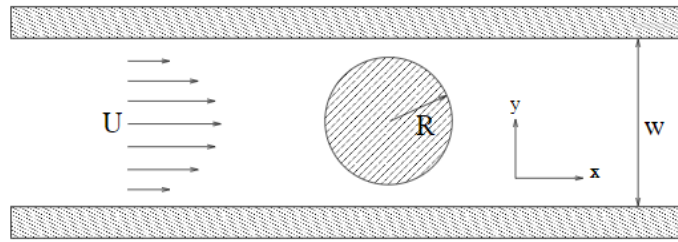


FIGURE 2.20: Advection of passive particles in an open flow setup with an obstacle[98].

2.18.1 Chaotic Advection

Chaotic advection is the chaotic motion of passive particles in a deterministic velocity field. Hasan Aref first coined the term in 1984[98]. Chaotic advection can generate small-scale structures in the spatial distribution of advected fields. This is possible due to chaotic flows' stretching and folding properties, which tend exponentially to a geometric pattern[99]. Mixing by chaotic advection has advantages over turbulence. It does not require extensive energy input and can induce mixing in microfluidics with low Reynolds numbers.

2.19 Static Mixers

Static mixers are systems based on geometric re-orientations to mix two fluids. They blend fluids (liquids or gases) through their stationary mixing elements placed inside the pipe housing. The mixing elements split two regions and reconnect them[98].

2.19.1 Kenics static mixer

A Kenics static mixer (KSM) is an arrangement of motionless helicoidal mixing elements fixed in a cylindrical housing, as shown in Fig. 2.22. The extrusion of

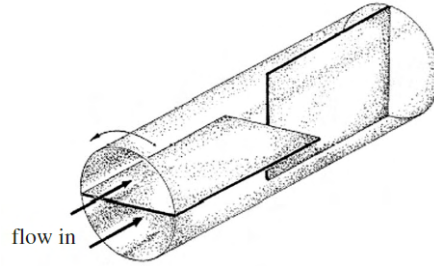


FIGURE 2.21: The partitioned pipe mixer, an example of a static mixer[100].

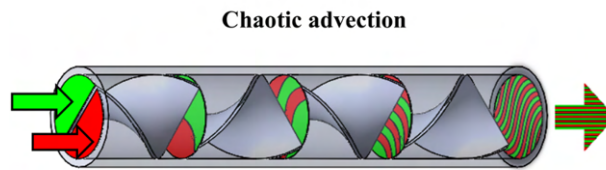


FIGURE 2.22: KSM inducing chaotic advection for mixing two hydrogels[101].

two fluids through a printhead containing a KSM increases the number of interfaces between them exponentially, according to the number of mixing elements used.

The number of striations generated by a KSM of 2 inlets can be calculated according to Equation II.5 :

$$s = 2^n \quad (\text{II.5})$$

where s is the number of striations and n is the number of KSM mixing elements.

The following equation can calculate the width of each striation:

$$l = d/s \quad (\text{II.6})$$

where l is the width of striations, d is the diameter of the KSM nozzle tip, and s is the number of striations[5].

CHAPTER III

METHODOLOGY

Type and design of study

Since experimental techniques and instrumentation were used to optimize a technology—in this case, chaotic bioprinting—this project can be classified as applied research.

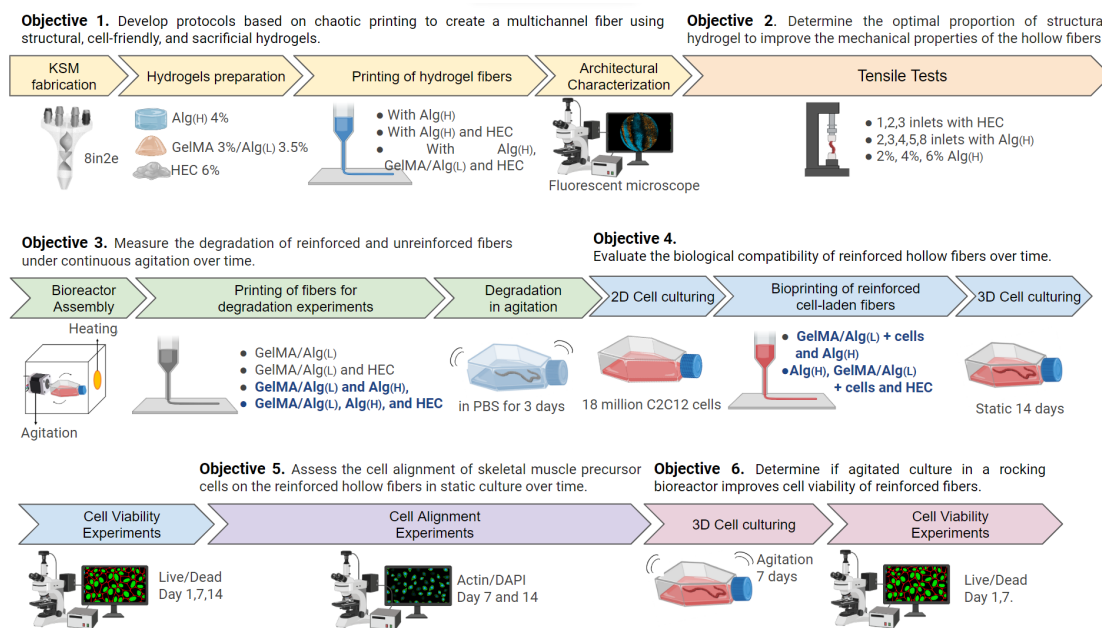


FIGURE 3.1: Methodology schematic

The methodology is divided according to the six specific objectives. The first three objectives are focused on experiments without cells to develop the printing strategy, evaluate the mechanical properties of fibers, and assess the degradation over time of the reinforced hydrogel fibers. Objectives four, five, and six are focused

on experiments with cells to understand biological compatibility, cell alignment, and the effect of the agitated culture on cell viability. The general methodological workflow is explained in Fig.3.1.

3.1 Printing protocols based on chaotic printing

The development of chaotic printing protocols was achieved in three stages: the fabrication of the printhead, the optimization of printing protocols, and the architectural characterization of the hydrogel fibers. The methodological workflow for the first specific objective is explained in Fig.3.2.

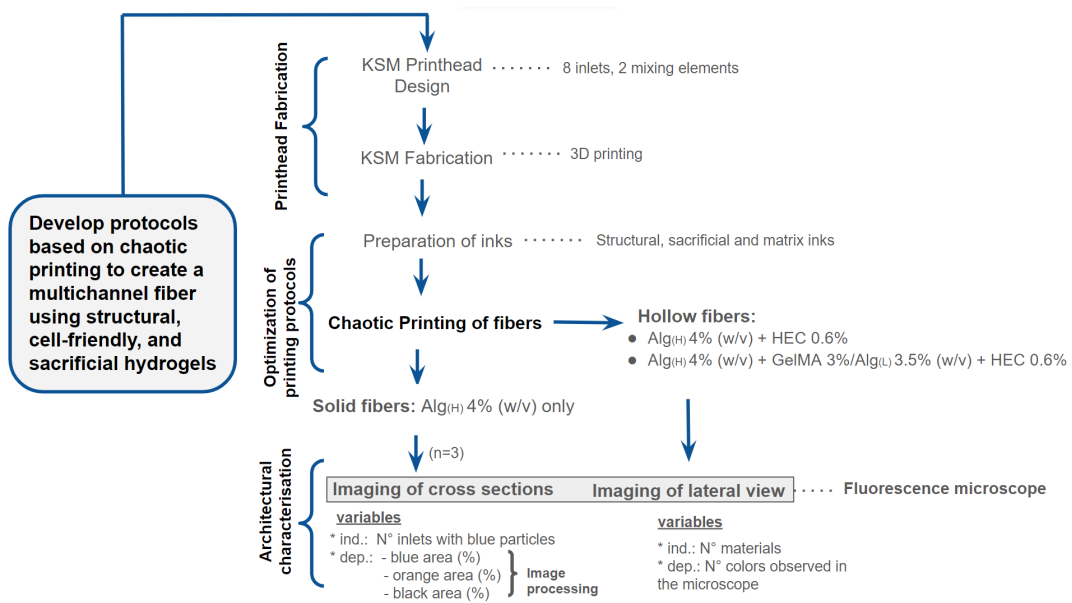


FIGURE 3.2: Methodology schematic for specific objective N°1.

The first step consisted of choosing correctly the design of the printhead. A KSM that has 8 inlets and 2 mixing elements was selected by following four criteria that will be explained in a further section. Then, the KSM was fabricated with resin through 3D printing. The second stage consisted of preparing a structural,

a sacrificial, and a matrix ink; the chaotic printing of solid and hollow fibers; and the crosslinking of the materials to obtain a hydrogel fiber. Finally, the last stage consisted of the architectural characterization of solid and hollow fibers by taking images in the fluorescence microscope and image processing.

For solid fibers made of $\text{Alg}_{(H)}$ only, the inlets were loaded with three fluorescent particles to represent the structural, sacrificial, and matrix materials using blue, black, and orange particles, respectively. The independent variable was the number of inlets loaded with blue fluorescent particles. The dependent variables were the blue, black, and orange area (%) on the fibers' cross-section. Hollow fibers were assessed qualitatively by imaging the lateral view of the fibers. The independent variable was the number of materials used to fabricate the fibers. The dependent variable was the number of colors observed in the microscope, as each material was assigned a different color.

A list of the solutions used in this first set of experiments is described in Table 3.1

TABLE 3.1: Solutions used for experiments without cells

Solution	Concentration	Solute Amount	Total Volume	Solvent
CaCl_2	2% (w/v)	10 g	500 mL	dH_2O
HEC	0.6% (w/v)	0.3 g	50 mL	dH_2O
$\text{Alg}_{(H)}$	2% (w/v)	1 g	50 mL	dH_2O
	4% (w/v)	2 g	50 mL	dH_2O
	6% (w/v)	3 g	50 mL	dH_2O
$\text{Alg}_{(L)}$	7% (w/v)	0.7 g	10 mL	dH_2O
GelMA	6% (w/v)	0.6 g	10 mL	DPBS
LAP	0.2% (w/v)	0.02 g		
Fluorescent particles	5% (v/v)	0.5 mL	10 mL	dH_2O

Additionally, the equipment that was used for developing the printing strategy and performing the architectural characterization is listed in Table 3.2

TABLE 3.2: Equipment used for experiments without cells

Equipment	Application
Formlabs 3D printer	KSM Fabrication
Formlabs Form Wash	
UV Curing Lamp	
Digital Balance	Inks Preparation
Analytical Balance	
Centrifuge	Optimization of Printing Parameters
Multichannel Pump	
Omniculture UV Curing	
Fluorescent Microscope	Architectural Characterization
Universal Tensile Machine	Tensile Tests
Rocking Bioreactor	Degradation Analysis

3.1.1 KSM Printhead Design

KSM of eight inlets and two mixing elements was designed in AutoCAD with a nozzle diameter and length of 1 mm and 3 mm, respectively. The walls' thickness, including the mixing elements' thickness, was 1 mm to provide enough mechanical strength to the KSM[102]. The design needed additional structural support to withstand the 3D printing process without collapsing. In that sense, additional scaffolds in PreForm Software were added to preserve the KSM's structure. Specific dimensions of the nozzle and inlets of the KSM cannot be included in this document because the design is in the process of registration as a patent in Mexico and the United States. A conceptual design of the KSM is provided in Fig. 3.3.

Four criteria guided the printhead design:

1. Ability to co-extrude a sacrificial, a matrix, and a structural ink:

Using eight inlets enables printing with three materials. The conventional KSM can co-extrude only two inks. Fortunately, a KSM can be adapted to have 4, 6, or 8 inlets for co-extrusion of two or more inks[103].

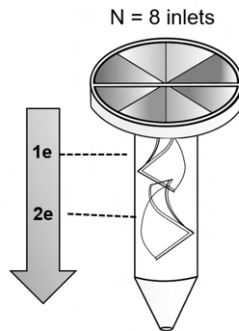


FIGURE 3.3: Conceptual design of the KSM printhead with 8 inlets and 2 mixing elements.

2. Capability to include different materials into a single structure:

Using two mixing elements is optimal for placing hydrogels of different viscosities together in a predictable pattern without mixing them thoroughly. Using more than two mixing elements results in better mixing of the materials, but it also decreases the elastic modulus of the hydrogel fibers[5]. Using two mixing elements is preferred to maintain the constructs' mechanical stability while creating hydrogel fibers with multiple layers.

3. Ability to generate chaotic flows: Like any static mixer, the KSM induces chaotic flows when extruding non-Newtonian fluids, such as inks, through its mixing elements[98].

4. Capability to be manufactured in-house with a 3D printer: The KSM is easily adaptable for 3D printing manufacturing because it has helicoidal mixing elements. Helicoidal structures facilitate the precise layering of resin during the printing process[104]. Other static mixers, like Ross or Sulzer SMX, have intricate geometries that are difficult to adapt for 3D printing fabrication[100].

3.1.2 KSM Fabrication

The KSM was fabricated through resin 3D printing. A resin 3D printer uses UV light to cure photosensitive resin, layer by layer; a screen partially blocks the UV light, and the exposed resin layer hardens. After printing, the KSM was exposed to an isopropyl alcohol (IPA) bath for 20 minutes. Then, the structural support was removed carefully. Subsequently, the KSM was exposed again to an IPA bath for 10 minutes. The KSM was dried gently with an air compressor and finally photo-crosslinked with UV light for 15 minutes. The fabrication process is described in Fig. 3.4, and the equipment used is shown in Fig. 3.5.

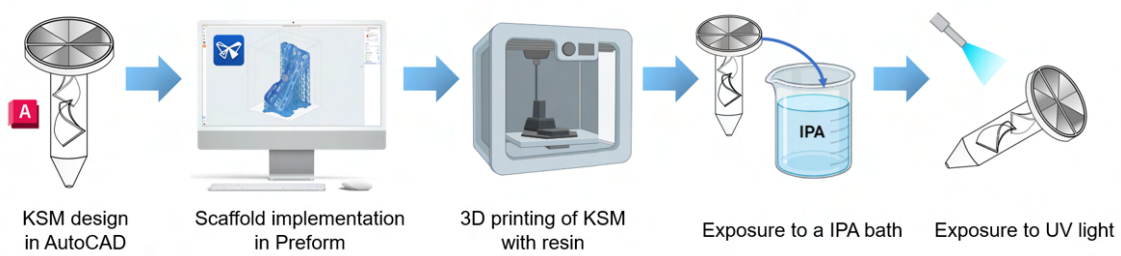


FIGURE 3.4: Steps for the KSM printhead fabrication.

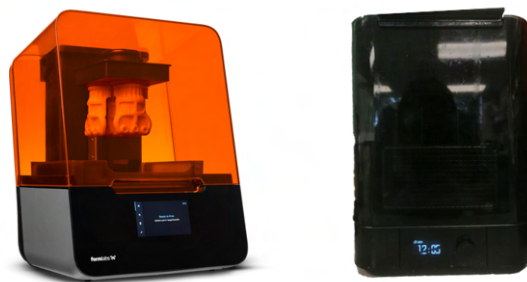


FIGURE 3.5: Equipment used for KSM fabrication. Form 3+ Resin 3D printer from Formlabs (left) and Formlabs Form Wash to remove resin from the KSM (right).

The Form 3+ resin printer cures an entire layer simultaneously, allowing for faster 3D printing with a high resolution as thin as 0.025 mm (Appendix 1). However, a longer post-processing step is needed to remove residual resin and improve the mechanical properties of the printed object[105]. Additionally, the resin is cancerogenic, so the printed construct must be manipulated with gloves until the post-processing step is complete.

3.1.3 Preparation of inks

Three inks were prepared using chemical methods: structural, matrix, and sacrificial. $\text{Alg}_{(H)}$ was used as a structural hydrogel due to its mechanical properties[106]. Concentrations of $\text{Alg}_{(H)}$ since 4% have been reported to provide mechanical support to hydrogel fibers [103]. Therefore, a solution of $\text{Alg}_{(H)}$ at 4% (w/v) was prepared using 2 g of $\text{Alg}_{(H)}$ dissolved in 50 mL of dH_2O . This solution was mixed with a magnetic agitator on a hot plate at 70°C for 45 seconds (Fig. 3.6).

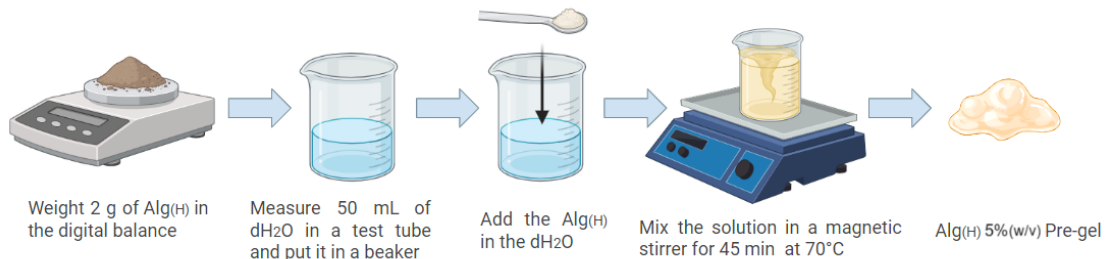


FIGURE 3.6: Protocol for preparation of $\text{Alg}_{(H)}$ 4% (w/v).

A solution of GelMA with $\text{Alg}_{(L)}$ was used as a matrix ink. A bioink made of $\text{Alg}_{(L)}$ 3.5% and GelMA 3% (w/v) was reported to sustain cell growth with high cell viability[14]. The first step of the matrix ink preparation is to synthesize $\text{Alg}_{(L)}$ at 7% (w/v) (Fig. 3.7). This was achieved by adding 0.7 g of $\text{Alg}_{(L)}$ in 10 mL of

dH₂O. This solution was mixed with a magnetic agitator on a hot plate at 50°C for 45 minutes. Then, a GelMA solution at 6% was prepared with LAP as a photocrosslinking agent. For a total GelMA/Alg_(L) solution of 20 mL, 0.6 grams of in-house lyophilized GelMA were added to 10 mL of Dulbecco’s phosphate-buffered saline (DPBS) with 0.02 grams of LAP. The protocol for synthesizing lyophilized GelMA is described in Appendix 2. Alg_(L) 7% (w/v) was added to the GelMA 6% (w/v) solution in a proportion of 1:1 to obtain 20 mL of GelMA 3%/Alg_(L) 3.5% (w/v). Finally, the solution was heated in a water bath at 70°C for 10 minutes to homogenize the ink (Fig. 3.8).

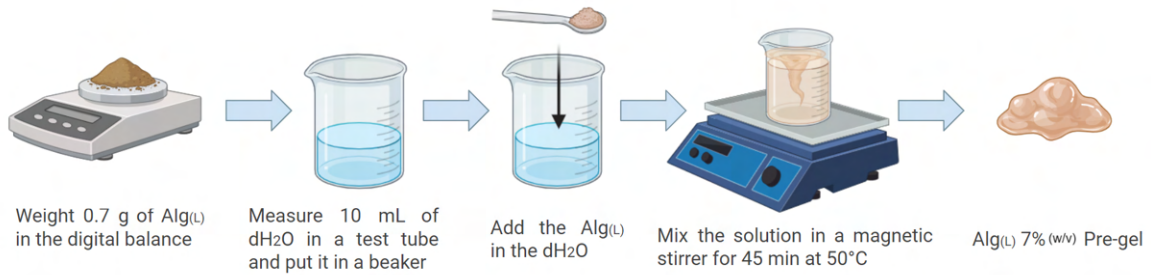


FIGURE 3.7: Protocol for preparation of Alg_(L) 7% (w/v).

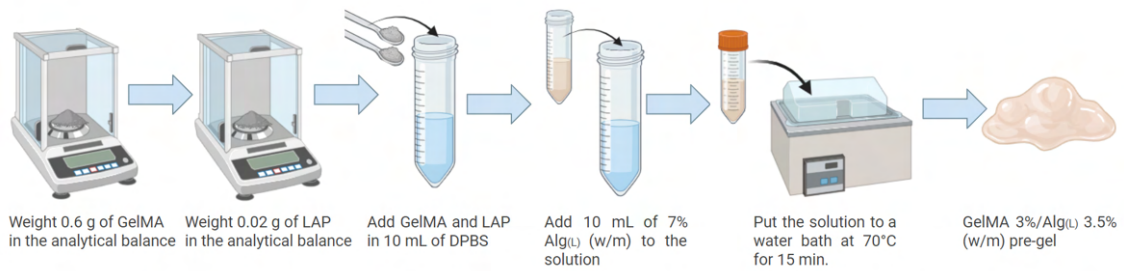


FIGURE 3.8: Protocol for preparation of GelMA 3%/Alg_(L) 3.5% (w/v).

HEC was used as a sacrificial ink. Low concentrations of HEC have been reported to dissolve easily in liquid solvents[107]. In addition, previous reports showed

that HEC 0.6% (m/v) dissolves in a CaCl_2 bath and creates hollow channels in hydrogel fibers[15]. To obtain an HEC solution at 0.6% (m/v), 0.3 grams of HEC were dissolved in 50 mL of dH_2O under agitation at 70°C for approximately 45 min, being careful of water evaporation (Fig. 3.9).

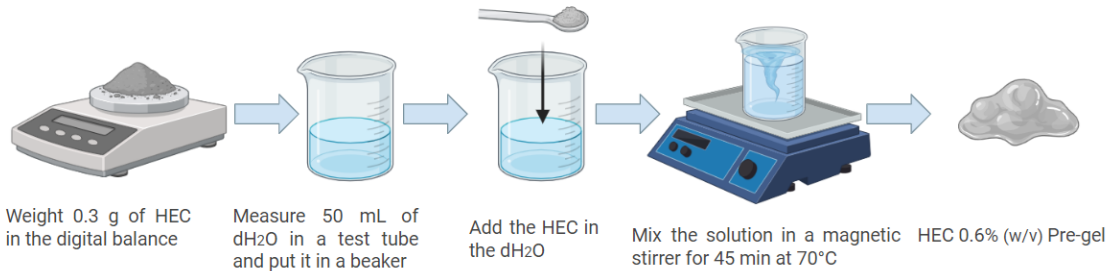


FIGURE 3.9: Protocol for preparation of HEC 0.6% (w/v).

3.1.4 Chaotic printing of hydrogel fibers

The hydrogels were warmed in a water bath at 50°C for 20 minutes and stained with fluorescent microparticles to distinguish them under the fluorescence microscope. Fibers of $\text{Alg}_{(H)}$ 4% were printed using three different colors, representing the following inks: $\text{Alg}_{(H)}$ (light blue), HEC (black), and GelMA/ $\text{Alg}_{(L)}$ (orange).

For solid fibers of $\text{Alg}_{(H)}$ 4% (w/v) only, the perfusion rate was 1 ml/min. These fibers were printed to compare their cross-sections with those predicted by computational simulations. For hollow fibers of $\text{Alg}_{(H)}$ 4% (w/v) and HEC 0.6% (w/v), the perfusion rate was 0.5 ml/min. For multimaterial hollow fibers, $\text{Alg}_{(H)}$ 4% (w/v), HEC 0.6% (w/v), and GelMA 3%/ $\text{Alg}_{(L)}$ 3.5% (w/v) were co-extruded at a printing rate of 0.2 mL min^{-1} . Both $\text{Alg}_{(H)}$ and $\text{Alg}_{(L)}$ were crosslinked in a CaCl_2 solution of 2% (w/v) due to the presence of Ca^{2+} ions [106]. The crosslinking of GelMA was done with UV light at a delta length of 365 nm for 45 minutes due

to the presence of LAP as a photocrosslinking agent. A multichannel syringe pump was used to control the velocity of perfusion of the inks, while an Omnicure S2000 curing system was used for GelMA/AlgAlg_(L) photocrosslinking (Fig. 3.10). The printing protocol is shown in Fig. 3.11.

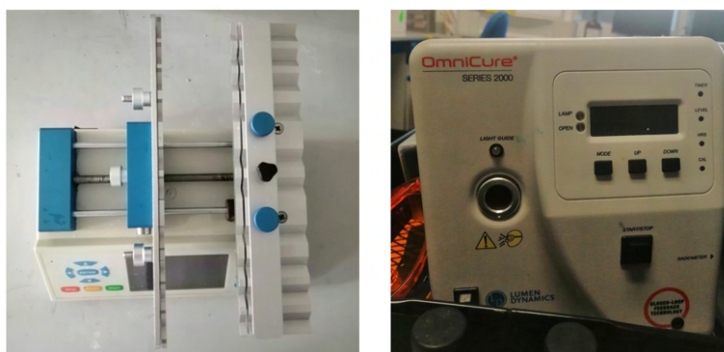


FIGURE 3.10: Equipment used for chaotic printing. The multichannel pump was adapted for 8 syringes (left), and Omnicure S2000 was used for the photocrosslinking of GelMA (right).

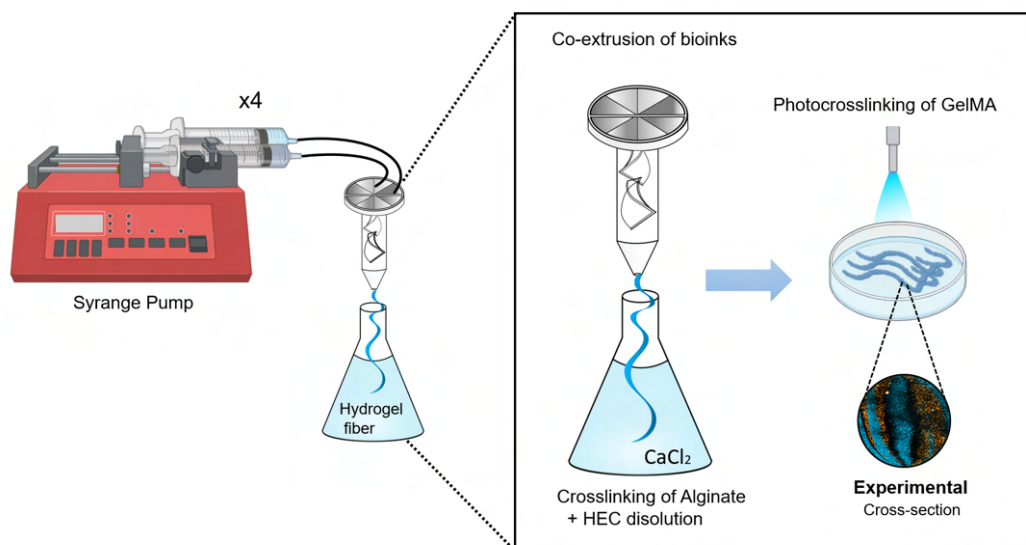


FIGURE 3.11: Schematic representation of the chaotic bioprinting strategy implemented

Chaotic printing has a high throughput; therefore, 2 meters of fiber could be printed in less than 5 minutes. Nonetheless, one limitation of this technique is that the syringe pump needed to be adapted to use eight syringes simultaneously, and there is little control over the geometrical arrangement of the fibers in the 3D space. While photocrosslinking GelMA, it is preferable that exposure to UV light is no longer than 2 minutes, as prolonged exposure times can kill cells [79].

3.1.5 Architectural Characterization

Conceptual images of the cross-sections were obtained with Computational fluid dynamics (CFD) simulations. The CFD images were a courtesy of Diego Quevedo. Cross-section images of solid fibers (of just Alg_(H)) were obtained by cutting a tiny portion of the fiber with a blade, wetting them with dH₂O, and visualizing the cross-sections in an Axio Observer.Z1 microscope (Zeiss, Germany) equipped with Apotome, and a 10x objective. The proportion of each ink was calculated by measuring the light-blue, black, and orange areas in ImageJ. The calculation was repeated three times (n=3) using three images. The following equation calculated the area of each ink:

$$P_i(\%) = \frac{A_i}{A_t} \cdot 100(\%) \quad (\text{III.1})$$

where P_i is the proportion of ink, A_i is the Area of ink "i" (pixels), and A_t is the Total area (pixels).

Images of the lateral view of hollow fibers (Alg_(L), GelMA/Alg_(L), and HEC) were obtained by an axio observer.Z1 microscope in the dark field mode to assess the formation of hollow microchannels inside the constructs. The assessment was done qualitatively by observing the number of colors in the microscope and the color distinction between each layer.

3.2 Optimization of mechanical properties

Three steps were followed to improve the mechanical properties of the reinforced hydrogel fibers. The first step consisted of the chaotic printing of fibers with variations in the following independent variables: number of holes, proportion of Alg_(H), and Alg_(H) concentration. The second step consisted of performing the tensile tests in a homemade universal testing machine. After the test, the values of the dependent variables were obtained from the stress-strain curve. Such variables are strain, stress at break (kPa), and elastic modulus (kPa). Finally, a statistical analysis was performed using two-sided ANOVA and Tukey Test to evaluate statistical differences between the dependent variables' values. The methodological workflow for the second specific objective is explained in Fig. 3.12.

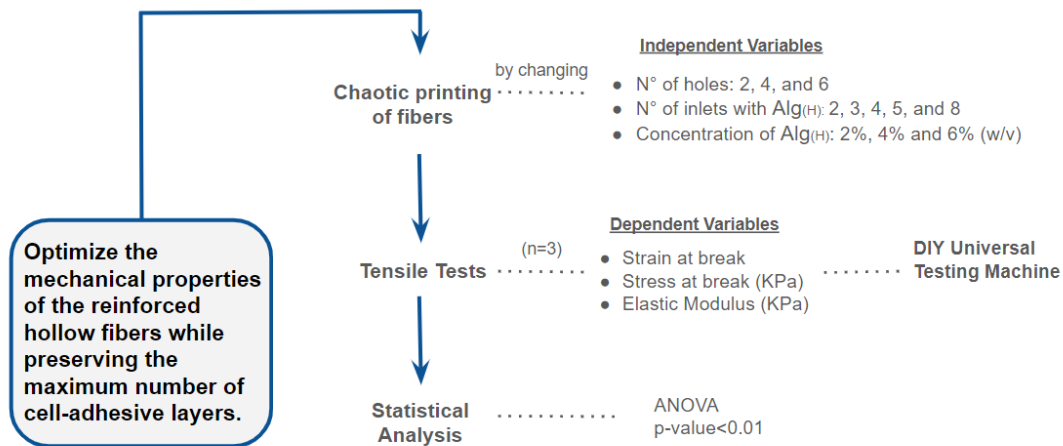


FIGURE 3.12: Methodology schematic for specific objective N°2.

3.2.1 Chaotic printing of fibers

Printing protocols developed in the previous section were used to print hydrogel fibers for the tensile tests. Regarding the inks, a GelMA 3%/Alg_(H) 3.5% (w/v) was

used as a matrix ink, and HEC 0.6% (w/v) was used to generate hollow channels. Alg_(H) was prepared at concentrations of 2%, 4%, and 6% (w/m). Alg_(H) 2% (w/v) was prepared using 1 g of Alg_(H) dissolved in 50 mL of dH₂O. Then, Alg_(H) 4% (w/m) was prepared using 2 g of Alg_(H) dissolved in 50 mL of dH₂O(w/v). Finally, Alg_(H) 6% (w/m) was prepared using 3 g of Alg_(H) dissolved in 50 mL of dH₂O(w/v). All the solutions were mixed with a magnetic agitator on a hot plate at 70°C for 45 seconds. The chaotic printing and crosslinking processes were the same as described in the printing protocols.

3.2.2 Tensile Tests

Tensile tests were performed on a do-it-yourself (DIY) tensile testing machine fabricated in the laboratory. The mechanical structure of the machine is made with 3D-printed parts, and the electrical system is based on Arduino UNO. The tensile tests for each set of experiments were repeated three times (n=3) to calculate the average values and standard deviations. The strain at break, stress at break (kPa), and elastic modulus (kPa) were extracted from the stress-strain curve of each set of hydrogel variations.

The test followed American Society for Testing and Materials (ASTM) standards for tissue engineering scaffolds (ASTM F2150-13) and plastics (ASTM D638) [108]. The fibers had a thickness of 1 mm, according to the values provided by the ASTM D638 standard (between 1 and 14 mm). Additionally, the 1 kg load was applied at a rate of 36 mm/min as this velocity allowed for better stretching of polymeric materials[109] and followed the values provided by the ASTM D638 standard (1-500 mm/min). The load was applied until the samples finally broke from the center of the structure (Fig. 3.13). A video showing how the tensile test was done can be found in Appendix 3.

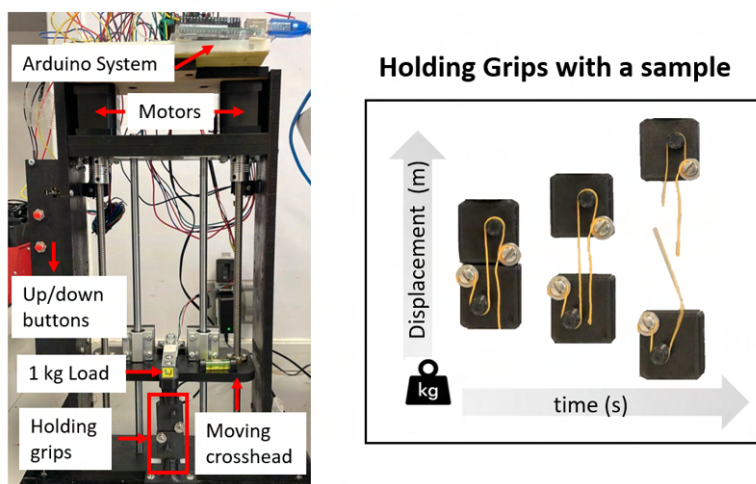


FIGURE 3.13: Tensile test machine made in the laboratory and its parts (left). Holding grips of the tensile machine with a hydrogel fiber as a sample (right).

The samples consisted of reinforced hydrogel fibers with variations on:

1. **The number of holes:** Hollow fibers have a pre-vascularized structure with void channels that resemble the vascularization of native tissues. In that sense, creating fibers with the maximum number of holes possible is preferred to improve the cells' viability in the scaffold. However, the amount of pre-vascularized channels should not affect the mechanical stability of the scaffold. Based on a chaotic printing strategy, the proportion of sacrificial ink in the printhead influences the number of void microchannels created inside the fiber.

For this reason, the number of inlets with HEC was changed to test the mechanical properties of fibers with 1, 2, and 3 HEC inlets. These variations created reinforced hollow fibers with 2, 4, and 6 hollow channels, respectively. Once the proportion of HEC was optimized, this proportion was not changed in the subsequent printings to optimize the following parameter. The fibers were printed using GelMA 3%/Alg_(H) 3.5% (w/v), HEC 0.6% (w/v), and Alg_(H) 2% (w/m).

2. The proportion of Alg_(H): Another parameter that needed optimization was the proportion Alg_(H) in the reinforced hollow fibers. The mechanical properties of the hollow fibers are influenced by the proportion of structural material used during the printing process. While increasing the number of Alg_(H) layers results in better mechanical properties, it also decreases the proportion of GelMA/Alg_(L) layers. GelMA/Alg_(L) is the matrix material; thus, it provides a friendly environment for cells to adhere to. If the number of GelMA/Alg_(L) layers is reduced, there will be less space within the fiber for cells to grow. As skeletal muscle tissue is mainly made of cells, keeping as many cell-friendly layers as possible is better.

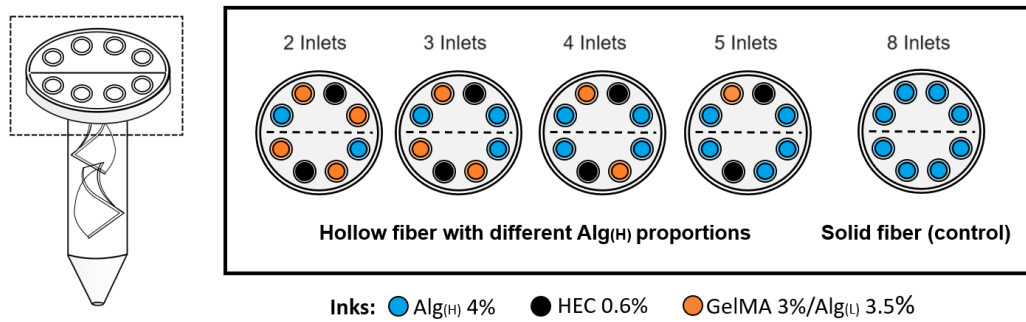


FIGURE 3.14: KSM used to print hydrogel fibers with variations in Alg_(H) proportion.

Therefore, an optimal point between the proportion of Alg_(H) and the proportion of cell-adhesive layers inside the fiber must be reached. To determine the optimal proportion of Alg_(H), the number of Alg_(H) inlets was changed from 2, 3, 4, 5, and 8 inlets (Fig. 3.14). The fiber with 8/8 Alg_(H) inlets was used as a control sample. Once the proportion of Alg_(H) was optimized, this proportion was not changed in the next printings to optimize the next parameter. The fibers were printed using GelMA 3%/Alg_(H) 3.5% (w/v), HEC 0.6% (w/v), and Alg_(H) 2% (w/m).

3. The concentration of Alg_(H): The concentration of the structural material was the last parameter assessed. The mechanical properties of the reinforced hollow fibers are also affected by the concentration of the structural material. The fibers were printed using GelMA 3%/Alg_(H) 3.5% (w/v), HEC 0.6% (w/v), and with different concentrations of Alg_(H). To determine the optimal Alg_(H) concentration, concentrations of 2%, 4%, and 6% (w/m) were tested.

The data obtained by the Arduino code (displacement (mm) vs. Force (N)) was used for calculating the stress-strain curve in Microsoft Excel with the following equations:

$$Strain = \frac{D}{L_0} \quad (III.2)$$

where D is Displacement (mm), and L₀ is Initial length (mm).

$$Stress(kPa) = \frac{F}{A \cdot 100} \quad (III.3)$$

where F is Force (N), and A is Cross-sectional area (mm²).

Then, the elastic modulus (kPa) was calculated by finding the slope from the linear region of the stress-strain curve through linear regression in Microsoft Excel.

3.2.3 Statistical Analysis

Statistical analysis was performed in Excel. All data were reported as means ± standard deviations. A two-sided one-way analysis of variance (ANOVA) and Tukey's test for multiple comparisons were used for the statistical analysis. A p-value < 0.05 was considered statistically significant, while a p-value < 0.01 was considered highly

significant. Once the optimal proportion of HEC, Alg_(H), and optimal Alg_(H) concentration were chosen, optimized reinforced hollow fibers were printed for the degradation analysis.

3.3 Mass degradation of hydrogel fibers in a rocking bioreactor

Improving the mechanical properties of the fibers was based on the fact that, subsequently, they would be exposed to a 3D culture with continuous agitation in a bioreactor. A mass degradation analysis is one way to evaluate whether mechanically reinforced fibers can withstand continuous agitation over time. First, it was necessary to assemble the homemade bioreactor. Then, mechanically reinforced (experimental samples) and non-reinforced fibers (control samples) were printed. Finally, a degradation analysis was conducted for 72 hours, measuring the percentage of mass remaining in both reinforced and unreinforced fibers. The degradation experiments were repeated three times to calculate the average values and standard deviations. The methodological workflow for the third specific objective is explained in Fig.3.15.

3.3.1 Rocking Bioreactor Set-up

A homemade rocking bioreactor was set up using two Arduino Nano boards for the electronic circuits, one for controlling temperature and the other for controlling agitation velocity. The fibers were put inside the rocking bioreactor in phosphate-buffered saline (PBS) (pH=7.4) in a proportion of 1:1 (w/v) (5 grams of hydrogel fibers in 5 mL of PBS). The temperature was set at 37°C because mouse myoblasts (the precursor cells chosen for experiments with cells) grow at that temperature. That temperature is also a standard for any mammalian cells. The velocity of the

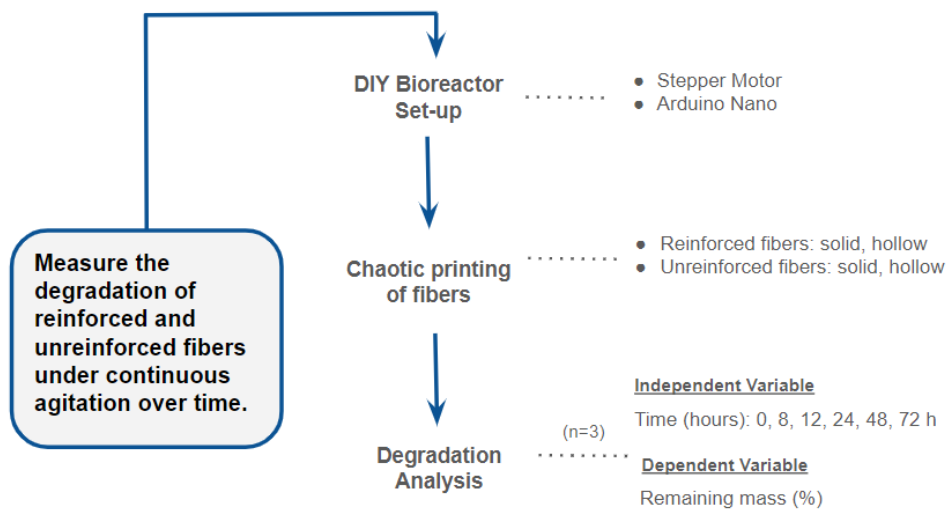


FIGURE 3.15: Methodology schematic for specific objective N°3.

stepper motor that induces agitation was set up at 60 RPM, with a continuous back-and-forth cycle that lasted 1 minute.

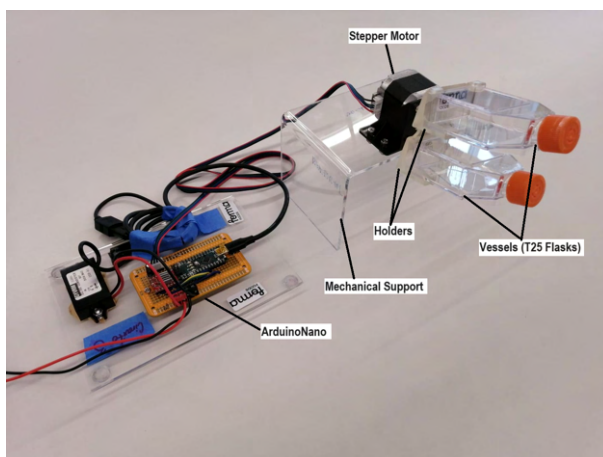


FIGURE 3.16: DIY bioreactor system. A T25 flask was attached using a 3D-printed piece of resin to the magnet connected to the motor.

The bioreactor's vessel was a T25 flask, commonly used in 2D cell culturing but, in this case, adapted for 3D cell culturing of cell-laden hydrogel fibers. The

bioreactor was designed to withstand the continuous agitation of two T25 flasks simultaneously. This design was made to culture the maximum amount of cell-laden hydrogel fibers at the same time as a way to scale up the tissue maturation process. Additionally, it allowed to conduct two sets of experiments with cells simultaneously to save time and space. Fig. 3.16 shows all the components of the DIY bioreactor, including the mechanical support, stepper motor, Arduino Nano board, and holders for two vessels.

3.3.2 Printing of fibers for degradation experiments

Reinforced and unreinforced hydrogel fibers were printed for the degradation experiments. Reinforced fibers are all the hydrogel filaments that have layers of Alg_(H) (the structural material). In contrast, unreinforced fibers are all the hydrogel filaments that do not have layers of Alg_(H).

- **Unreinforced solid fibers:** They were the first control group and were made of GelMA/Alg_(L) only. In other words, they were entirely made of matrix material and did not have holes.
- **Reinforced solid fibers:** They were the second control group and were made of GelMA/Alg_(L) and layers of Alg_(H). In other words, they were made of matrix and structural material.
- **Unreinforced hollow fibers:** They were the third control group and were made of GelMA/Alg_(L) and HEC (the sacrificial ink). In other words, they were made of matrix and sacrificial material.
- **Reinforced hollow fibers:** These fibers were the experimental group. They were made of Alg_(H), HEC, and GelMA/Alg_(L). They were developed after the optimization of the proportion of HEC, the proportion of Alg_(H), and the

concentration of $\text{Alg}_{(H)}$. The exact composition of these fibers will be described in the Results and Discussion section.

The control samples were made of just one or two materials (one material per inlet). For this reason, they were printed with a KSM of 2 inlets and 4 mixing elements to simplify the printing process (Fig. 3.17). This KSM created fibers with 16 layers (the same number of layers created by the 8-inlet 2-mixing elements KSM).

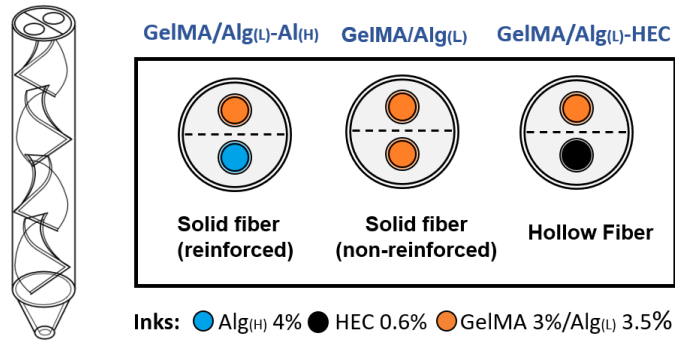


FIGURE 3.17: Composition of control samples for degradation experiments.

3.3.3 Degradation of fibers

The initial mass of printed fibers (without cells) was measured with an analytical balance on a milligram scale. The analytical balance measured the wet mass at $t = 8$ h, 12 h, 24 h, 48 h, and 72 h. The remaining weight (%) was calculated with the following equation:

$$Rm(\%) = \frac{M_o - M_i}{M_o} \cdot 100(\%) \quad (\text{III.4})$$

where Rm is Remaining mass (%), M_o is Initial mass (mg), and M_i is Mass at a time "i" (mg).

3.4 Evaluation of biological compatibility

After optimizing the mechanical properties of the reinforced hollow fiber and verifying that it can withstand continuous agitation, the biological compatibility of the fiber was evaluated. The evaluation involves several steps.

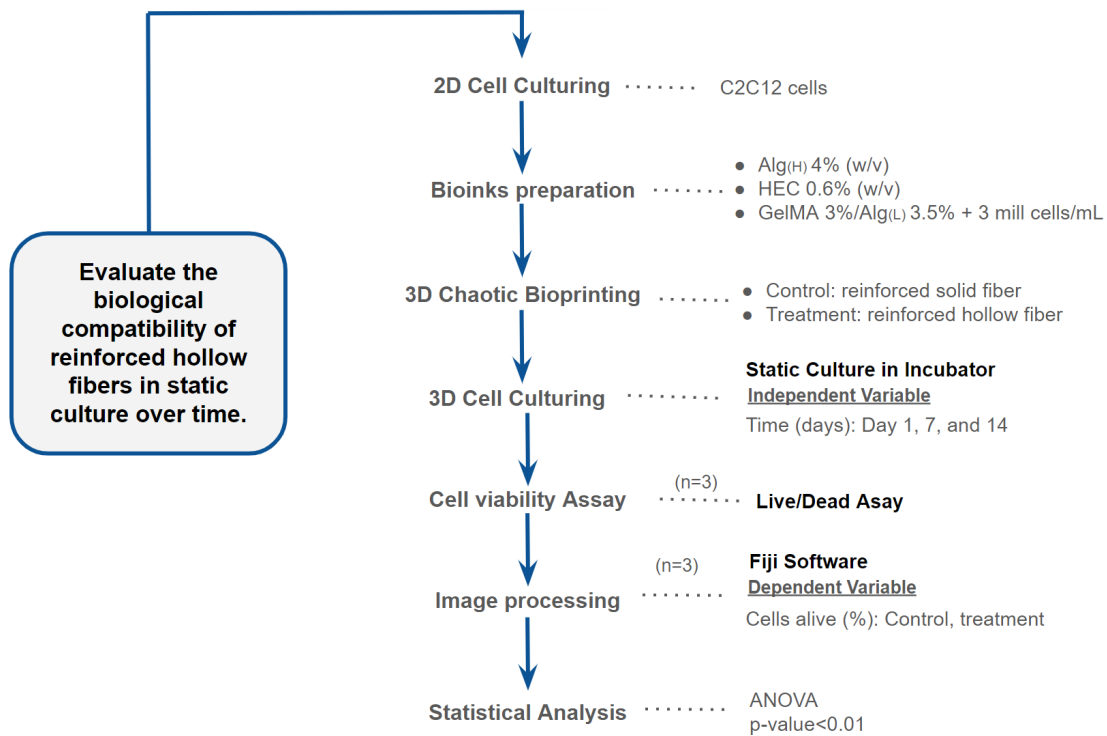


FIGURE 3.18: Methodology schematic for specific objective N°4.

First, 2D cell culturing is necessary for the expansion of C2C12 cells. After having the required number of cells, bioinks were prepared by following the printing protocols with some variations. All the bioinks were solved in DPBS, and the matrix ink was loaded with cells. Then, chaotic bioprinting of the control samples (reinforced solid fibers) and the treatment samples (the optimized reinforced hollow fibers) was done.

The bioprinted scaffolds were cultured for 14 days in an incubator, and live/dead assays were performed on days 1, 7, and 14. Image processing of live/dead staining images in the fluorescence inverted microscope revealed the amount of viable (%) and dead (%) cells. Finally, statistical analysis showed the meaningful significance of cell viability among control and treatment samples over time. The independent variable is time (days 1, 7, and 14), while the dependent variable is the percentage of viable cells (%). Cell viability assays were done three times (n=3) per sample type. The methodological workflow for the fourth specific objective is explained in Fig.3.18.

A list of the solutions used in experiments with cells is described in Table 3.3.

TABLE 3.3: Solutions used for experiments with cells

Solution	Concentration	Solute Amount	Total Volume	Solvent
CaCl ₂	2% (w/v)	10 g	500 mL	dH ₂ O
HEC	0.6% (w/v)	0.6 g	100 mL	DPBS
Alg _(H)	4% (w/v)	2 g	50 mL	DPBS
Alg _(L)	7% (w/v)	0.7 g	10 mL	DPBS
GelMA	6% (w/v)	0.6 g	10 mL	DPBS
LAP	0.2% (w/v)	0.02 g		
Anti-anti	1X	0.15 mL	15 mL	PBS
Live	1 µg/mL	2 µL	1 mL	PBS
Dead	1 µg/mL	1 µL		
Phalloidin	1 µg/mL	1 µL	1 mL	PBS
DAPI	1 µg/mL	10 µL		
Paraformaldehyde	4% (w/v)	2 g	45 mL	PBS

3.4.1 2D Cell Culture

A cell suspension of 1 mL with a concentration of 1 million cells/mL was defrosted at room temperature. The cell suspension was put in a T25 flask with 4 mL of

Dulbecco's modified eagle medium (DMEM) media containing 1% of antibiotic/antimycotic (anti-anti) and 10% of fetal bovine serum (FBS). The T25 was incubated at 37°C and 5% CO2 for one day. The day after, the media was changed to remove dimethyl sulfoxide (DMSO), a toxic cryopreservative that was included in the frozen cell suspension, from the media.

Cell passing was performed inside a hood when the cells reached 80% confluence. The media was extracted with a serological pipette from the T25 flask. To deactivate the FBS, 1 mL of PBS was used to wash the flask. Trypsin 0.25 (2 mL) was added to the flask to detach the cells from the wall. The T25 flask with trypsin was incubated at 37°C for 5 minutes. To ensure the cells were detached, they were observed under an optical microscope at x10.

The cells with trypsin were added to a Falcon tube of 15 mL with 1 mL of DMEM and centrifuged at 1000 RPM for 5 minutes. The supernatant was discarded, and the pellet was resuspended with 6 mL of DMEM. The cell suspension was distributed with the same volume in two T25 flasks (3 mL per flask). The flasks were stored in an incubator at 37°C until use. Cellpasing was repeated until 12 million cells were obtained.

A list of the equipment used in cell culturing is described in Table 3.4.

TABLE 3.4: Equipment used for cell culturing

Equipment	Application
-80° Refrigerator	Cryopreservation of cells
-20° Refrigerator	Storage of antibiotics and trypsin
4°C Refrigerator	Storage of culture media and PBS
Laminar Hood	Change of media and passaging cells
Centrifuge	Cell separation
Inverted Microscope	Cell counting
Incubator	Cell growth
Fluorescent Microscope	Cell imaging

3.4.2 Bioinks preparation

A solution of Alg_(H) at 4% was prepared using 0.8 g of Alg_(H) dissolved in 20 mL of DPBS. This solution was mixed with a magnetic agitator on a hot plate at 70°C for 45 minutes or until completely dissolved. To obtain an HEC solution at 0.6%, 0.12 grams of HEC were dissolved in 20 mL of DPBS under agitation at 70°C for approximately 45 min, being careful of water evaporation.

A GelMA solution at 6% was prepared with LAP as a photocrosslinking agent. For a total solution of 10 ml, 0.3 grams of lyophilized GelMA was added to 5 mL of DPBS with 0.01 grams of LAP. The solution was heated in a water bath at 70°C for 15 minutes. Secondly, a solution of Alg_(L) at 7% was prepared with 0.35 g of Alg_(L) in 5 mL of water. This solution was mixed with a magnetic agitator in a hot plate at 50°C for 45 minutes or until completely dissolved. Finally, the GelMA 6% solution was mixed with Alg_(L) 7% in a proportion of 1:1. The final solution was composed of GelMA 3% and Alg_(L) 7% in 10 mL. The whole process was done in darkness to avoid the photocrosslinking of GelMA.

The inks were sterilized with a syringe filter of 0.4 µm in porous diameter, allowing bacteria and other microorganisms to detach from the hydrogels before printing. All hydrogels were tempered to 37°C before the bioprinting for compatibility with C2C12 cells. To prepare the bioink (hydrogel loaded with cells), a cell suspension of C2C12 with a concentration of 3 million cells/mL was used. Five mL of cell suspension was centrifuged at 1,000 RPM for 5 minutes. The suspension was discarded, and the pellet was then resuspended in the GelMA 3%/Alg_(L) 3.5% (m/v) solution.

3.4.3 3D Bioprinting with cells

A KSM of eight inlets and two mixing elements was used for the treatment samples as the chaotic bioprinting printhead. Under sterilized conditions and inside a laminar hood, 8 syringes were loaded with 2 mL of hydrogel and connected to the KSM inlets through silicon elastic tubes. The GelMA/Alg_(L) ink was loaded with C2C12 cells at a concentration of 3 million cells/mL, while Alg_(H) and HEC were not loaded with cells. All hydrogels were perfused at a 0.1 ml/min rate through the KSM printhead into a beaker containing CaCl₂ 2% (w/v). Both alginates (Alg_(H) and Alg_(L)) were crosslinked in the CaCl₂ bath for 1 minute, and GelMA was crosslinked with UV light at a delta length of 365 nm for 45 seconds. After printing, the fibers were washed twice with sterile PBS to remove the CaCl₂ from the fibers (Fig. 3.19).

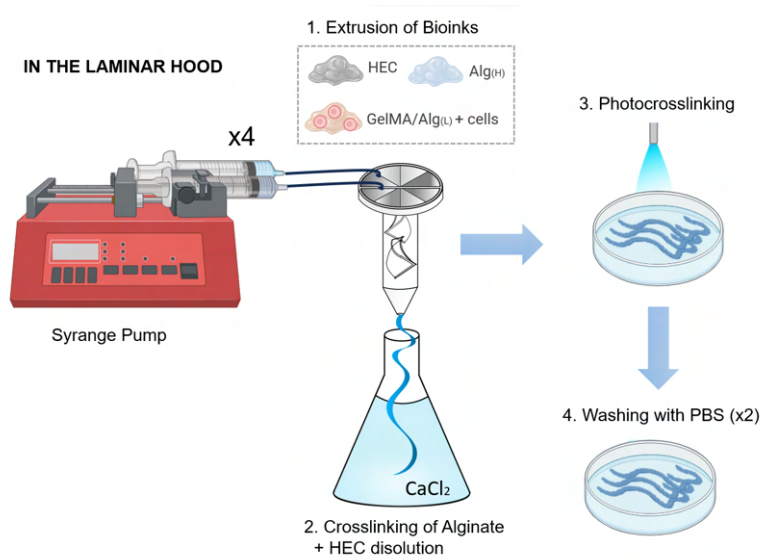


FIGURE 3.19: Bioprinting strategy for reinforced hollow fibers (treatment).

For the control samples, a KSM of two inlets and four mixing elements was the printhead in the bioprinting system. In the laminar hood, 2 syringes were loaded with bioinks. One syringe had cell-free Alg_(H), while the second had a cell-loaded

GelMA/Alg_(L) bioink with a cell concentration of 3 million cells/mL. Printing and crosslinking conditions were the same for printing the treatment samples (Fig. 3.20).

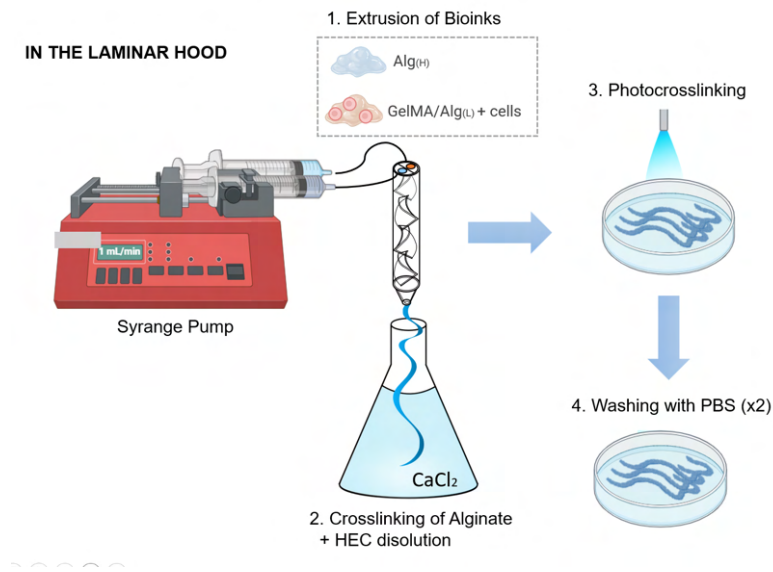


FIGURE 3.20: Bioprinting strategy for reinforced solid fibers (control).

A list of the equipment used in 3D chaotic bioprinting using cells is described in Table 3.5.

TABLE 3.5: Equipment used for 3D chaotic bioprinting

Equipment	Application
Digital Balance	Bioinks preparation
Analytical Balance	
Centrifuge	
Laminar Hood	3D bioprinting
Multichannel Pump	
Omniculture UV Curing	
Incubator	3D cell culturing
Fluorescent Microscope	Cell viability and spreading analysis

3.4.4 Static 3D cell culture

For static culture, the hydrogel fibers were divided into small sections of 5 cm inside each well of a 12-well plate with DMEM media containing 10% FBS and 2% anti-anti (Fig. 3.23). The high amount of antibiotics was necessary because bioprinting involves high manipulation of instruments and equipment, possibly leading to cross-contamination. The next day after bioprinting, the antibiotic was reduced to 1%. On day 5, the media was changed to a DMEM media containing 2% FBS and 1% anti-anti. The medium was changed every two days, and the fibers were cultured inside an incubator with 5% of CO₂ and 37°C.

3.4.5 Cell Viability experiments

The viability of the cells in the printed constructs was assessed on days 1, 7, and 14. Cross-sectional cuts were washed three times with PBS and assayed using a live/dead cell imaging kit containing 2 mM calcein AM and 4 mM ethidium homodimer (EtHD1). The samples were then placed in a dark, humidified incubator at room temperature for 1 h. Subsequently, they were washed with PBS and imaged using an axioscope.Z1 microscope equipped with Colibri.2 LED illuminations and an Apotome.2system (Zeiss). Every micrograph in the viability assays was taken with a 10X objective.

3.4.6 Statistical Analysis

Statistical analysis was performed in Excel using two-sided ANOVA and Tukey's test. A p-value < 0.05 was considered statistically significant, while a p-value < 0.01 was considered highly significant.

3.5 Cell alignment assesment

In native skeletal muscle tissue, the cells are highly aligned. The alignment gives functionality to the muscle tissue, as it allows the transmission of electrical signals for muscle contraction. Therefore, the degree of alignment of the cells in the hydrogel fibers was evaluated. The independent variable is time (days 7 and 14), while the dependent variable is the degree of orientation ($^{\circ}$). The control sample was a reinforced solid fiber of Alg_(H) and GelMA/Alg_(L), while the treatment was the optimized reinforced hollow fiber made of Alg_(L), HEC, and GelMA/Alg_(L). Printing protocols were the same as the ones described in the **Evaluation of biological compatibility** section. Cell alignment assessment was done three times (n=3) for both treatment and control samples. The methodological workflow for the fifth specific objective is explained in Fig.3.21.

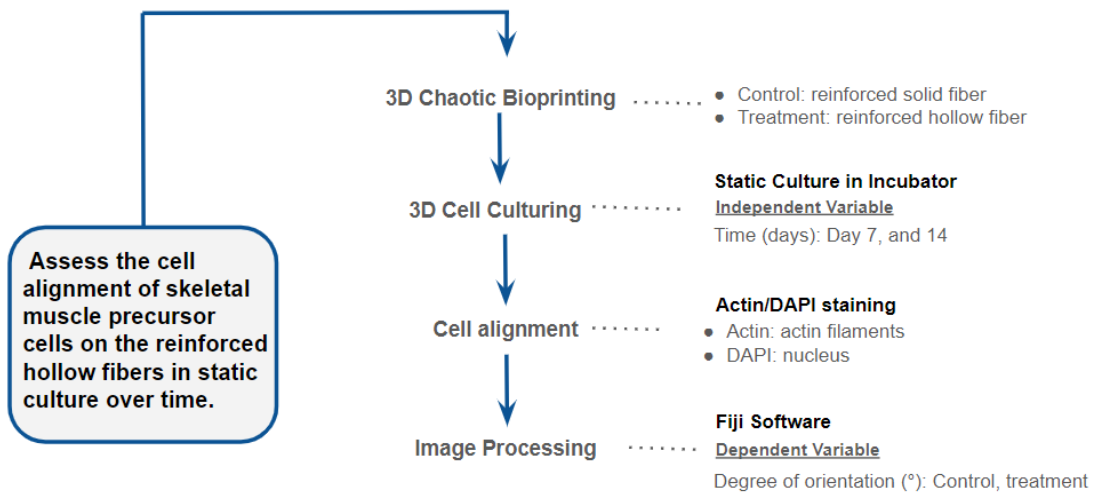


FIGURE 3.21: Methodology schematic for specific objective N°5.

3.5.1 Actin/DAPI staining

To evaluate cell alignment, it was necessary to visualize the actin filaments of the cells. The actin filaments are more visible when cells have higher spreading (flattening). The 4',6-diamidino-2-phenylindole (DAPI) staining enables the visualization of the cell nucleus. Samples of days 7 and 14 were fixed with 4% (w/v) paraformaldehyde solution for 30 minutes. All the samples were stained with phalloidin-iFluor 647 (1:1000) for actin and DAPI 1 ($\mu\text{g}/\text{mL}$) for nuclei according to the manufacturer's protocol. The constructs were submerged overnight in the staining solutions to enable effective diffusion.

The analysis was conducted with an Axio Vert.A1 microscope (Zeiss) equipped with a Colibri 2.0 illumination and an Apotome system. The AF647 channel (wavelength = 635 nm) was used to visualize phalloidin-iFluor (1:1000) staining, while the DAPI channel (wavelength = 358 nm) was used to visualize the stained nuclei.

3.5.2 Cell orientation assessment

The orientation angle of the myoblasts was estimated using the directionality tool in Fiji software using representative images from the Actin/DAPI staining at days 7 and 14. Fourier components and 13 bins per scalar from -90° to 90° were selected for the image processing. Frequencies were plotted as a polar histogram using compound graphics (radial) in Microsoft Excel.

3.6 Determination of cell viability in agitated culture

After assessing cell viability and cell orientation in static culture, the next step involved evaluating the cell viability in an agitated culture. Cell viability assays were done three times ($n=3$) per sample type. The methodological workflow for the sixth

specific objective is explained in Fig.3.22.

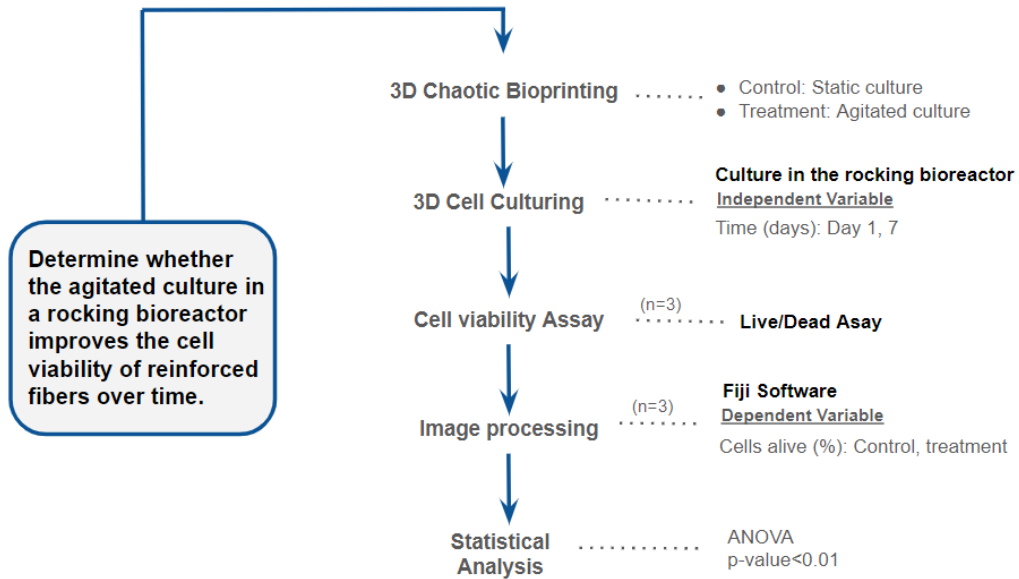


FIGURE 3.22: Methodology schematic for specific objective N°6.

3.6.1 Three-D cell culture in a rocking bioreactor

For culture with continuous agitation, the fibers were divided into sections of 10 cm inside a T25 flask (the bioreactor container). The cells were incubated at 37°C with 5% CO₂ for 7 days (Fig. 3.23), and the media was changed every 2 days. On the same day of bioprinting, DMEM media containing 10% FBS and 4% anti-anti was used for 3d cell culturing. The next day, the medium was changed to 2% anti-anti. On day 5, the media was changed to DMEM containing 2% FBS and 2% anti-anti.

3.6.2 Cell Viability experiments

The viability of the cells in the printed constructs was assessed on days 1 and 7. Cross-sectional cuts were washed three times with PBS and assayed using a

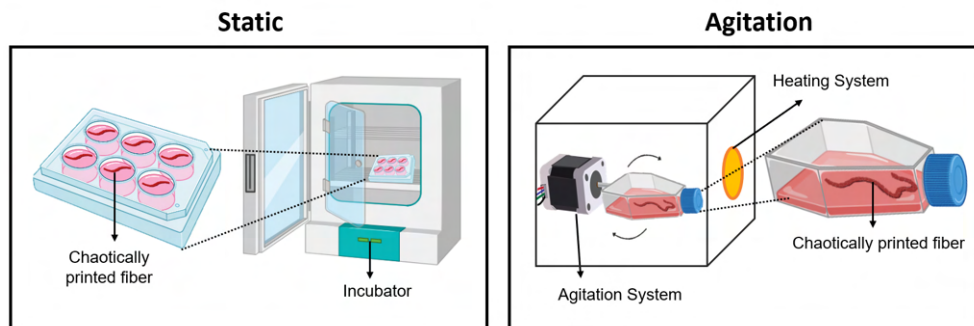


FIGURE 3.23: 3D Cell Culturing Conditions: static (left) and under constant agitation in a rocking bioreactor (right).

live/dead cell imaging kit containing 2 mM calcein AM and 4 mM ethidium homodimer (EtHD1). The samples were then placed in a dark, humidified incubator at room temperature for 1 h. Subsequently, they were washed with PBS and imaged using an axioscope.Z1 microscope equipped with Colibri.2 LED illuminations and an Apotome.2system (Zeiss). Every micrograph in the viability assays was taken with a 10X objective.

3.6.3 Statistical Analysis

Statistical analysis was performed in Excel using a two-sided ANOVA and Tukey's test. A p-value < 0.05 was considered statistically significant, while a p-value < 0.01 was considered highly significant.

3.7 Ethical Considerations

UTEC and ITESM approved the project. Since it was performed *in vitro* without the intervention of animal models or human participants, this project did not require approval from an ethics committee. The design of the KSM for chaotic bioprinting is

under patent in the United States and Mexico. Thus, this document cannot include the original sketch or complete measurements.

CHAPTER IV

RESULTS AND DISCUSSION

4.1 Development of printing protocols

Regarding the first specific objective, the following results were achieved: fabrication of the KSM printhead, computational simulation of chaotically-printed solid fibers, development of a mathematical equation estimating the number of layers within hydrogel fibers, chaotic printing of solid fibers, architectural characterization of solid fibers, printing of hollow fibers using two inks, and printing of hollow fibers using three inks.

A KSM printhead plays a pivotal role in the chaotic printing process by facilitating the co-extrusion and layering of inks. This capability arises from the multiple inlets in the top part of the KSM, allowing for the co-extrusion of inks. Additionally, the KSM generates chaotic flows through its mixing elements, facilitating layer stratification inside a hydrogel fiber without ink blending. Consequently, the chaotic printing strategy used in this thesis cannot be feasible without a KSM printhead. For this reason, a KSM printhead with 8 inlets and 2 mixing elements was created using resin 3D printing. The rationale for selecting the number of inlets and mixing elements was explained in the Methodology.

Characterizing the inner microarchitecture of the hydrogel fibers is necessary to control the fibers' composition and design when printing with multiple materials. Computational simulations elucidated each layer's shape and spatial distribution inside the fiber when using an 8-inlet KSM with 2 mixing elements. Then, a mathematical equation was introduced to determine the total number of layers within a

fiber just by knowing the number of inlets and the number of mixing elements. The equation demonstrated that altering the number of mixing elements within the KSM can impact the number of layers within a hydrogel fiber. Additionally, the equation can be used to calculate the amount of layers inside a fiber printed by KSMs with varying numbers of inlets and mixing elements.

Cell-free fibers were printed in the following sequence: solid fibers of one material, hollow fibers with two materials (one permanent ink and a fugitive ink), and finally, hollow fibers incorporating three materials (two permanent inks and a fugitive ink). This sequence was designed to streamline the printing protocols, progressing from the simplest to the most intricate procedure. Introducing additional printing materials (each one with a different viscosity) heightened the complexity of the printing system. Similarly, fabricating hollow channels introduced an extra layer of complexity due to the need for crosslinking and subsequent dissolution of the sacrificial ink.

First, solid fibers were printed with only one material (alginate) using three colors to represent three different materials. The printed fibers were used to quantify the proportion of each color in the crosssections. Then, they were compared to the color proportion in conceptual crosssections. This analysis aimed to assess whether the distribution of materials aligned with theoretical expectations and to identify any potential need for adjustments to printing parameters. In skeletal muscle tissue engineering, the hydrogel fibers' structure and composition are vital to recreate a functional artificial tissue.

Afterward, hollow fibers were printed using structural and sacrificial ink. The structural ink was identifiable under the microscope due to its distinct color, while the sacrificial ink dissolved, leaving void channels through which light passed. Subsequently, multi-material hollow fibers were printed, utilizing three materials: sacrificial ink, structural material, and another material for cell adhesion. Each

permanent ink was distinguishable under the microscope due to its unique color, whereas the sacrificial ink created void spaces within the fiber. The color distinction verified that the printing of hollow fibers did not affect the creation of layers with permanent, non-fugitive materials.

The computational model accurately depicted the distribution of layers within the fiber and their proportional relationship to the cross-sectional area. Based on simulations, the proposed mathematical equation generalized the number of layers in KSMs with varying numbers of inlets and mixing elements. Similarly, the printing protocols developed for the 8-input, 2-element KSM were effectively modified for chaotic printing of both solid and hollow fibers using up to three materials with varying viscosities.

4.1.1 Printhead fabrication

The KSM printhead was designed successfully in AutoCAD, and the scaffolds for stability during 3D printing was created using the PreForm Software. The scaffolds were placed to sustain the inlets and the top part of the KSM (Fig. 4.1).

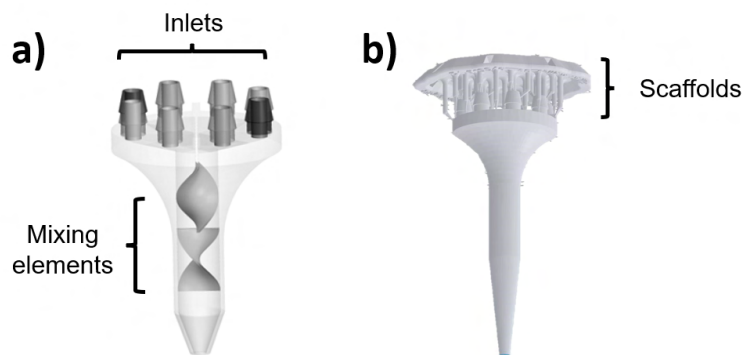


FIGURE 4.1: KSM design. a) 3D design of a KSM of eight inlets and two mixing elements. b) Adaptation of 3D KSM design in PreForm to ensure the structural conservation of the object during the printing process.

The KSM was printed on a 3D resin printer in a time lapse of 3 h. The resin scaffolds helped preserve the structure of the KSM printhead without breaking during the printing process. As part of the post-printing process, the washing process with IPA assisted in removing the exceeding resin from the KSM without affecting its structure (Fig.4.2).

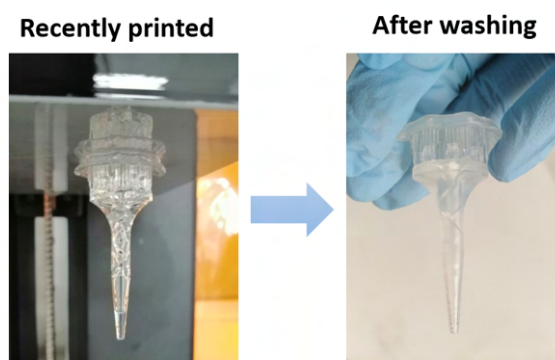


FIGURE 4.2: KSM just after the printing process was completed (left) and after washing with IPA to remove resin remains (right).

After removing the printing scaffolds, the eight inlets for the extrusion of multiple inks were visible. Then, the photocuring process with UV light was done successfully to solidify any remaining resin that was still viscous and improve the mechanical properties of the printhead. After post-printing, the two helicoidal mixing elements preserved their shape (Fig. 4.3).

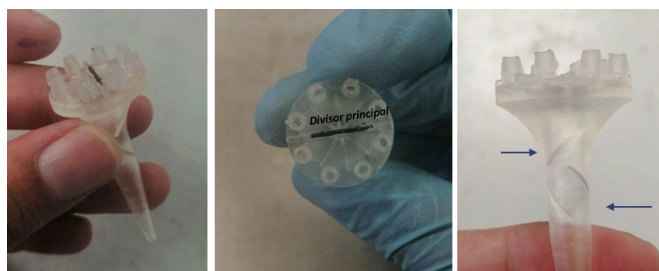


FIGURE 4.3: KSM printhead after removing scaffolds and photocuring (left). Top view (center). Helicoidal mixing elements (right)

4.1.2 Chaotic printing of hydrogel fibers

Solid and hollow fibers were printed without cells to optimize printing parameters such as extrusion speed and ink volume.

4.1.2.1 For solid fibers of Alg(H) only

Printing fibers without holes was accomplished using Alg_(H) 4% in all eight inlets of the KSM. Fluorescent inks (blue, red, green, and yellow) were added to make the layers visible under the fluorescent microscope. Fig. 4.4 shows how the syringes were configured in the multichannel syringe pump. Additionally, the elastic silicone tubes connected the syringe nozzle with all the Kenics inlets. After printing, the fluorescent inks left a color trace in the KSM head, indicating that the inks moved through the static mixer correctly.

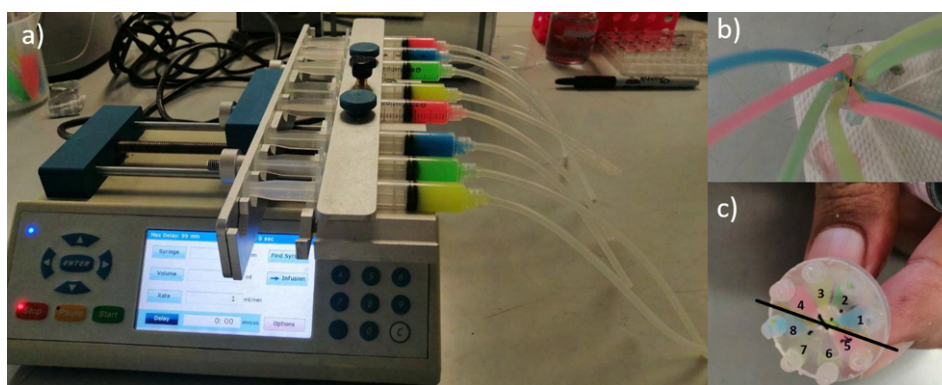


FIGURE 4.4: Printing setup for solid hydrogel fibers. a) A multichannel syringe pump with eight syringes loaded with Alg_(H) 4%. b) Connection of silicone tubes with the eight KSM printhead inlets. c) Printhead inlets after printing.

4.1.3 Printing hollow fibers of Alg(H) and HEC

The fibers with hollows were printed using Alg_(H) 4% in six syringes and HEC 0.6% in two syringes. The setup of the syringes in the pump was the same as shown in Fig. 4.4. Hydrogel fibers with a homogenous structure were printed successfully with a printing velocity of 0.5 mL/min. Higher printing rates created inconsistent structures because the co-extrusion of two inks with different viscosities leads to a mismatch in the material deposition. A slow printing rate reduces the shear stress, leading to a stable extrusion and better mixing of the inks.

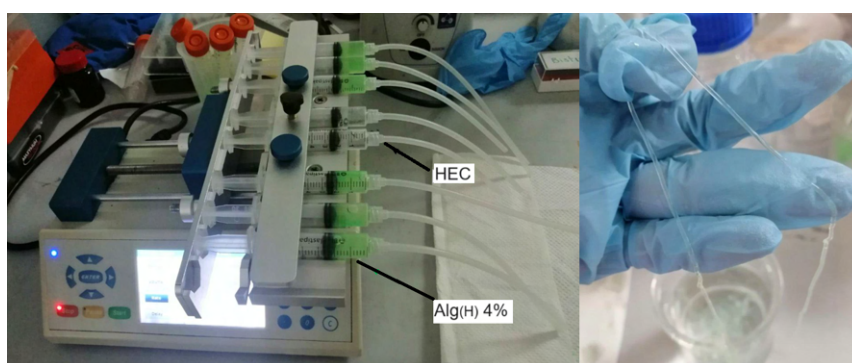


FIGURE 4.5: Printing setup for hollow fibers with two inks. Left: A multichannel syringe pump and syringes loaded with inks. Right: Printed fiber.

4.1.4 Printing hollow fibers of Alg(H), GelMA/Alg(L), and HEC

Multi-material hollow fibers of Alg_(H), GelMA/_(L), and HEC were fabricated by using the printing system shown in Fig. 4.6. The printhead was configured with three inlets for Alg_(H), three inlets for GelMA/_(L), and two inlets for HEC. The three inks were co-extruded at a velocity of 0.2 mL/min. The printing speed is slow because all the inks have different viscosities. Alg_(H) has a higher viscosity than GelMA, and GelMA/Alg_(L) has a higher viscosity than HEC[15]. When one of

the inks has a higher viscosity than the others, the shear stress of the whole fluid increases. This phenomenon can be explained by revising Eq. II.2:

$$\tau = \mu \cdot \frac{du}{dy},$$

where τ is shear stress (Pa), μ is the fluid's dynamic viscosity (Pa.s), and du/dy is the velocity gradient.

The shear stress (τ) is directly proportional to the viscosity (μ). If the viscosity increases, the shear stress increases as well. Therefore, decreasing the velocity gradient is a strategy to keep the shear stress as low as possible. In bioprinting, the velocity gradient is related to the extrusion rate.

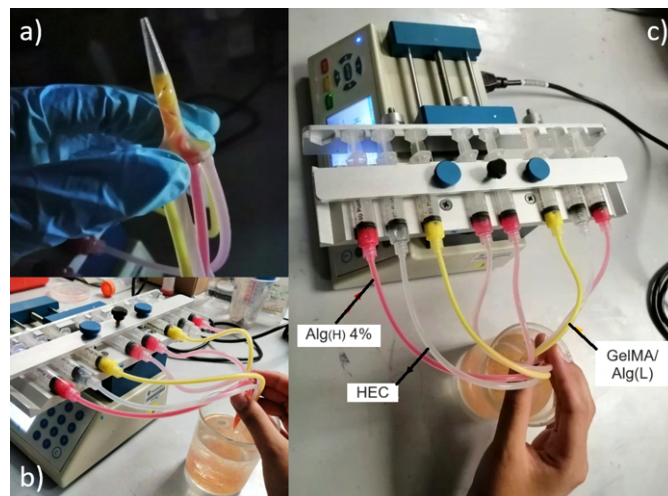


FIGURE 4.6: Chaotic bioprinting system for printing multi-material hollow channels. a) Loading of hydrogels inside the KSM. b) Multichannel syringe pump with loaded syringes connected to KSM during bioprinting. c) Hydrogels used for bioprinting. Alg_(H) is in red, GelMA is in yellow, and HEC is without color.

The fibers were crosslinked successfully with calcium chloride (for alginate) and UV light (for GelMA). A homogeneous hydrogel fiber was obtained because

the slow extrusion rate minimizes the tendency of clumping and agglomerations (Fig. 4.7). Increasing the time under the calcium chloride solution did not affect the crosslinking of alginate. However, GelMA exposition to UV light increased the polymer chains' bonding. GelMA hydrogel loaded with cells cannot be exposed to UV light for more than 1 minute, as the UV starts killing the cells. Thus, the exposure to UV light must be between 30 seconds and 1 minute [5]. The striations of permanent inks and the void channels produced by the sacrificial ink can be appreciated in Fig. 4.8.

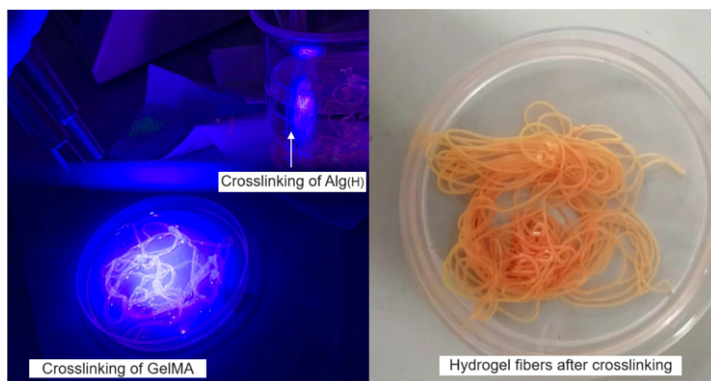


FIGURE 4.7: Crosslinking of multimaterial hollow fibers. Left: Crosslinking process. Right: Hydrogel fiber after crosslinking.

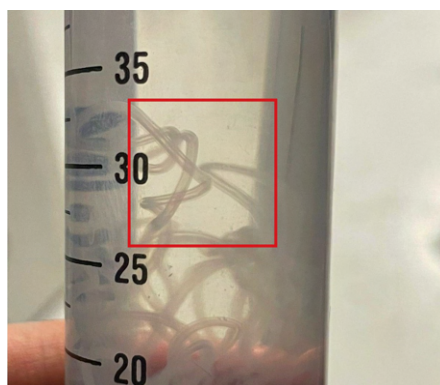


FIGURE 4.8: Multimaterial hollow fibers (without color).

4.1.5 Architectural Characterization

According to Computational Fluid Dynamics (CFD) simulations (courtesy of Diego Quevedo), when using a KSM with 8 inlets and two mixing elements as a printhead, a hydrogel fiber with 16 layers is produced. The simulations considered the extrusion of the same material through all 8 inlets of the KSM printhead. Despite being the same material, each inlet was stained with a different color to visualize the distribution of the layers in the crosssection.

The simulation illustrated that loading an ink into one inlet produced two layers of that material within the hydrogel fiber. For example, inlet n°1 (in red) produced 2 red layers inside the fiber. Similarly, inlet n° 7 (in blue) resulted in 2 blue layers in the crosssection distributed in a different space inside the fiber. The same happened for all the inlets (Fig. 4.9).

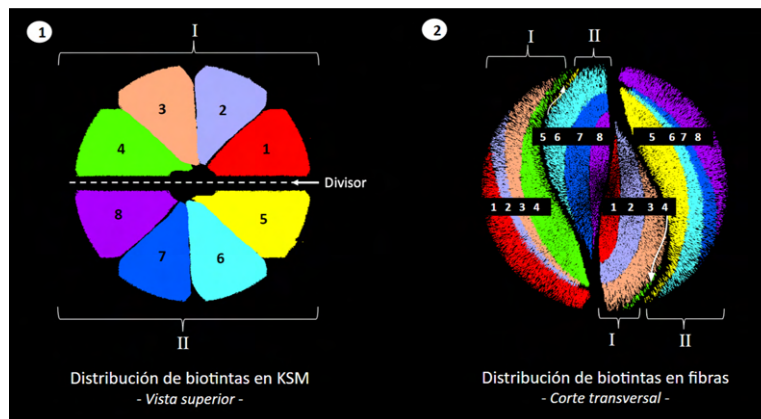


FIGURE 4.9: Simulation of hydrogel layers arrangement in the head of KSM (left) and in the crosssection of the fiber (right). Courtesy of Diego Quevedo.

Based on the simulation, the total number of layers inside a fiber can be predicted by the following equation:

$$s = N \cdot 2^{(n-1)} \quad (\text{IV.1})$$

where s is the number of layers, N is the number of KSM inlets, and n is the number of mixing elements.

If we replace N and n values for a KSM printhead with 8 inlets and 2 mixing elements, the mathematical expression would be:

$$s = 8 \cdot 2^{(2-1)} \quad (\text{IV.2})$$

Solving the equation yields that the number of layers is 16.

$$s = 8 \cdot 2^1 = 16 \quad (\text{IV.3})$$

Similarly, the width of each striation can be calculated by the equation $l=d/s$, where l is the width of striations, d is the diameter of the KSM nozzle tip (1 mm), and s is the number of striations. When printing fibers with a KSM with eight inlets and two mixing elements, the hydrogel fibers have 16 layers. Each entry loaded with ink forms two layers of that same material inside the construct with a 62.5 μm width. This width is appropriate considering that a microchannel is next to every cell-friendly fiber layer since nutrients cannot perfuse deeper than 200 μm [42].

4.1.5.1 For solid fibers

The goal of printing solid fibers was to check the feasibility of the computational simulations. Hollow fibers with variations in the number of Alg_(H) and GelMA/Alg_(L)

inlets were printed. The number of inlets with HEC remained constant, as depicted by Fig. 4.10.

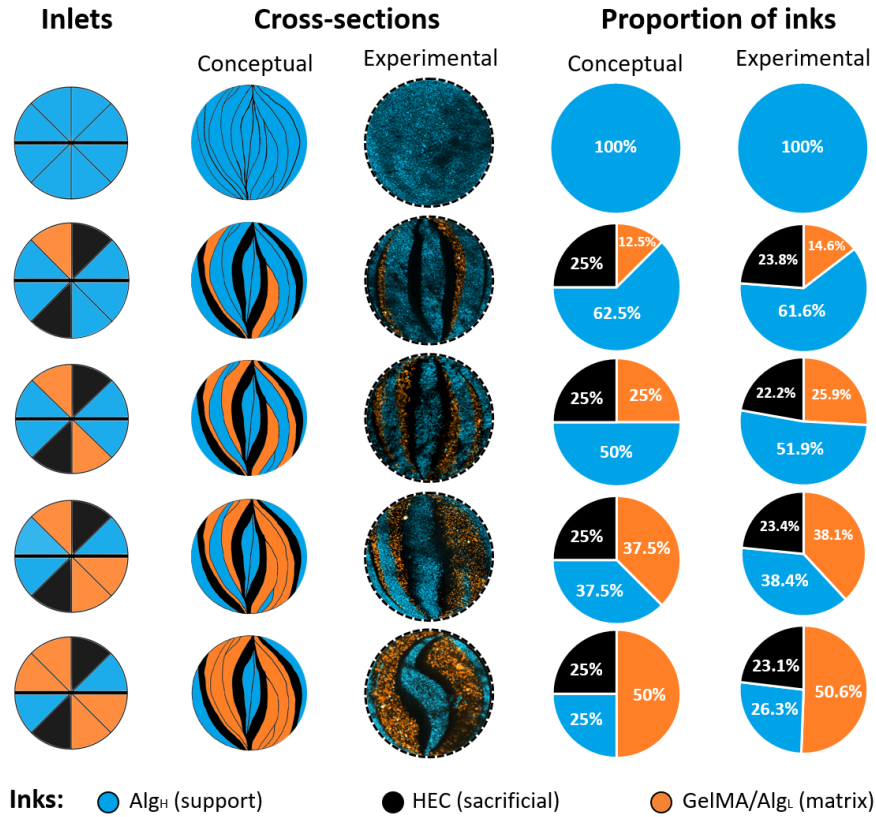


FIGURE 4.10: Hydrogel fibers of only Alg_(H) with inks proportion variations in the printing inlets. A comparison between conceptual and experimental results of the crosssections' architecture and inks' proportion is also shown.

Results showed that the conceptual crosssections were similar to experimental crosssections in geometry and spatial arrangement—moreover, the conceptual and experimental results for the proportion of inks returned similar values. For example, a fiber with a conceptual proportion of 50% for structural ink (light blue), 25% for matrix ink (orange), and 25% for sacrificial ink had an experimental proportion of 50.6% for the structural ink, 26.3% for the matrix ink, and 23.1% for the sacrificial ink. The same trend repeated in other ink configurations.

Generally, the fibers' crosssections were predicted accurately with the computational simulations. Chavez et al. also reported the predictable cross-sectional patterns of chaotically-printed fibers with a 2-inlet printhead [5]. Ceballos et al. already demonstrated that the simulations predicted the experimental crosssections of multi-material hydrogel fibers. They characterized the microarchitecture of chaotically-printed fibers with a 4-inlet, 6-inlet, and 8-inlet printhead[101]. Therefore, it is possible to modulate the composition of a multichannel hydrogel fiber by changing the proportion of each ink.

4.1.5.2 For hollow fibers

Obtaining crosssection images in the fluorescence microscope from hollow fibers was not possible. For this reason, the architectural characterization of hollow fibers was done qualitatively by observing the colors in their lateral view. Fluorescence images only captured the green color for hollow fibers of Alg_(H) and HEC. The Alg_(H) layers had a green fluorescent ink distinguished by the fluorescence microscope. The lateral view under the bright field showed light passing in some striated regions along the fiber. As Alg_(H) does not allow light to pass in the bright field, the striated white areas corresponded to void microchannels that were formed after the dissolution of HEC in CaCl₂ (Fig. 4.11).

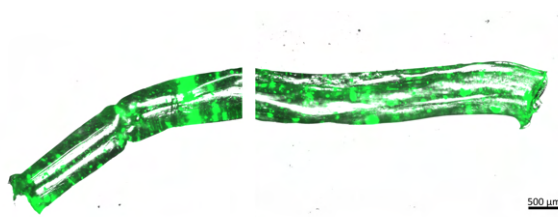


FIGURE 4.11: Lateral view of a hollow fiber of Alg_(H) and HEC under the bright field and a green fluorescent channel.

Fluorescence images captured the blue and red color for hollow fibers of Alg_(H), GelMA/Alg_(L), and HEC. The Alg_(H) ink was loaded with blue fluorescent particles, whereas the GelMA/Alg_(L) ink was loaded with red fluorescent particles. The combined channels (red+blue) can be observed with sober black striations in Fig. 4.12. Black striations correspond to void microchannels formed by HEC dissolution.

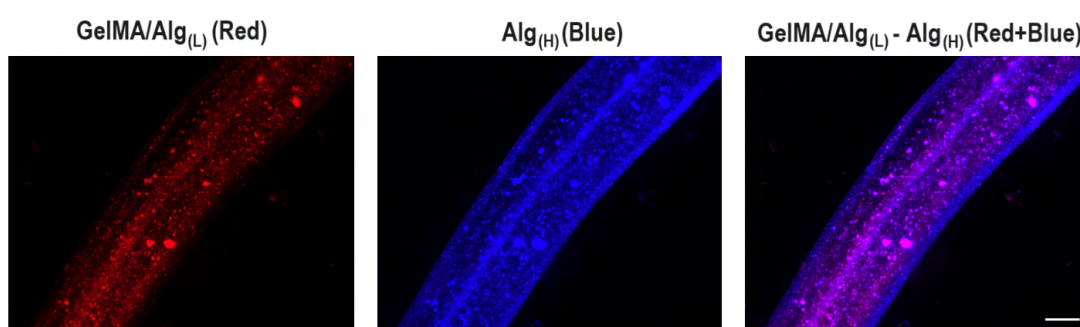


FIGURE 4.12: Fluorescent microscopy images of a multimaterial hollow fiber.

4.2 Tensile Tests

Mechanical tests were performed by optimizing the number of holes, the proportion of Alg_(H) layers, and the concentration of Alg_(H). The tensile tests determined the elastic modulus, strain at break, and stress at break of all the fibers' experimental variations. The elastic modulus describes the fiber's ability to deform under load and then return to its original shape when removed. The strain at break indicates the ability of the fiber to stretch before reaching its strength limit, while the stress at break shows the maximum force the material can withstand before breaking. Optimization was done mainly by comparing elastic modulus values. However, strain and stress at break values were used to differentiate between two fibers with an

optimal elastic modulus when just one needed to be chosen. All the decisions were based on the statistical analysis using ANOVA.

Knowing the mechanical properties of hydrogel fibers is necessary to optimize them for skeletal muscle tissue engineering applications. The human body's muscles are mainly flexible and elastic; that is, they can stretch before breaking. In this sense, the aim was to obtain a fiber with the highest strain at break value possible. Likewise, it must tolerate a specific load force (stress at break) before breaking without making the fiber too rigid. This must be achieved without compromising the number of hollow channels manufactured by the sacrificial ink dissolution and without drastically decreasing the number of cell-adhesive material layers.

4.2.1 The number of holes

Ideally, hydrogel fibers should have as many holes as possible to promote vascularization and enhance cell viability. However, increasing the number of holes decreased mechanical properties. Values from elastic modulus, strain at break, and stress at break were obtained from the stress-strain curve (Fig. 4.13).

The ANOVA test showed that the elastic modulus of fibers with 4 holes (11.76 kPa) and 6 holes (9.44 kPa) was statistically different. In comparison, the difference between the elastic modulus of fibers with 2 holes (10.74 kPa) and 4 holes (11.76 kPa) was insignificant (Fig. 4.13). This same pattern was found for the strain at break values, in which significant differences were found only between fibers with 4 holes (0.76) and 6 holes (0.32) (Fig. 4.14). The stress at break values of fibers with 2 holes (2.15 kPa) and 4 holes (3.10 kPa) differed, although the difference between fibers with 4 holes (3.10 kPa) and 6 holes (1.32 kPa) was more significant. The bar plots showing statistical differences of the strain and stress at break values are

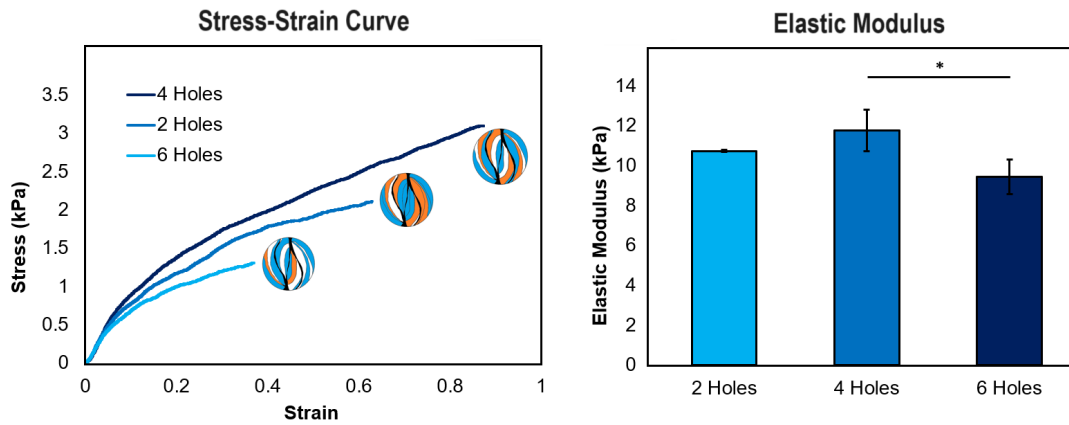


FIGURE 4.13: Mechanical properties of hydrogel fibers with variations in the number of hollow channels. The stress-strain curve (left) and bar plot represent statistical significance between the elastic modulus values (right).

shown in Fig. 4.13.

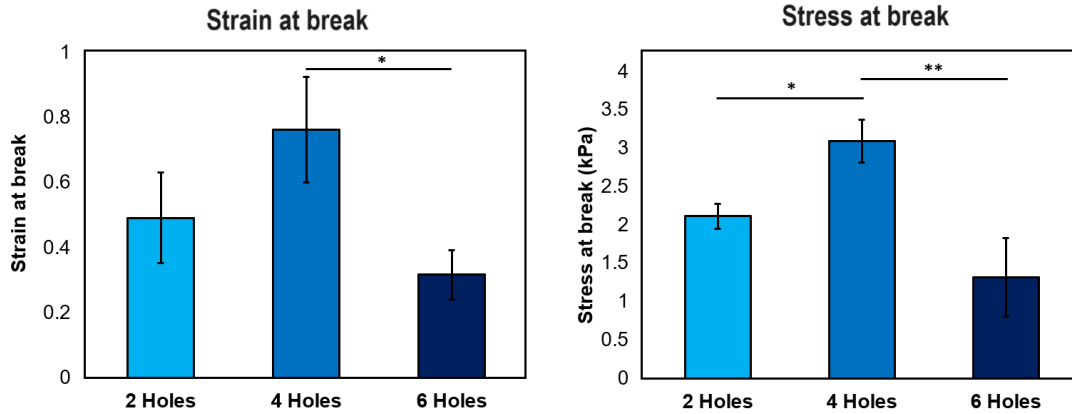


FIGURE 4.14: Bar plots representing statistical significance between strain values at break (left) and stress at break (right) of fibers with different numbers of holes.

Thus, a hydrogel fiber with 4 holes has the optimal amount of void microchannels without significantly decreasing the mechanical properties. Therefore, fibers with 4 holes were printed by adding 2 printhead inlets with the sacrificial ink (HEC) to perform the tensile assay in the next set of experiments.

4.2.2 The proportion of Alg(H) layers

Increasing the proportion of Alg_(H) inside the fibers improved mechanical properties. As shown by the stress-strain curve in Fig.4.15, the control sample (a solid fiber of Alg_(H) only) had better mechanical properties (17.87 kPa) than the hollow fibers with different Alg_(H) proportions. The fiber with the least Alg_(H) proportion (2 out of 8 inlets with Alg_(H)) had the stress-strain curve with the lowest slope and lowest strain and stress at break values. The ANOVA test showed differences in the elastic modulus values of all the experimental samples compared to the control sample. There were also differences between fibers with 2/8 Alg_(H) (4.78 kPa) and 3/8 Alg_(H) (8.93 kPa); and with fibers with 3/8 Alg_(H) and 4/8 Alg_(H) (11.76 kPa).

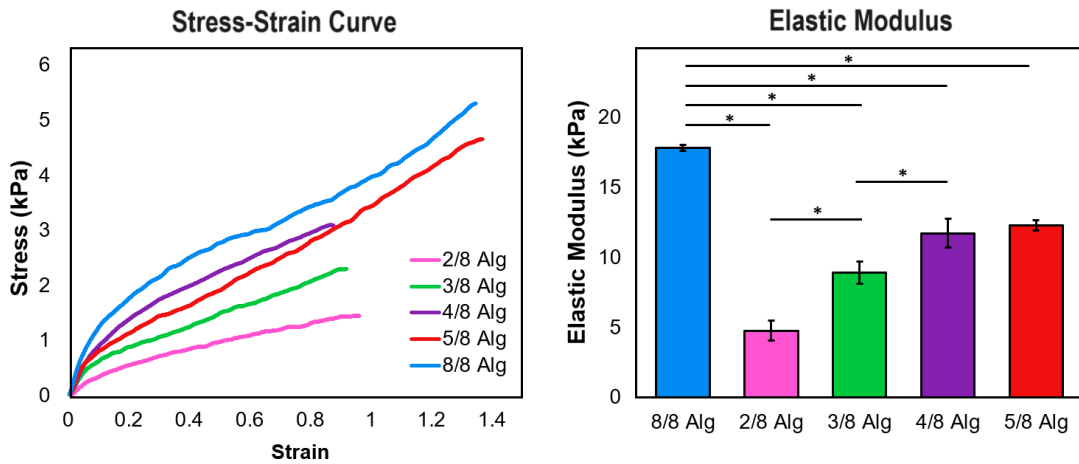


FIGURE 4.15: Mechanical properties of hydrogel fibers with variations in the proportion of Alg_(H) layers. Stress-strain curve (left) and bar plot representing statistical significance between values of elastic modulus

Regarding strain at break values, just the experimental sample of 4/8 Alg_(H) (0.76) had a meaningful difference compared to the control sample (1.29). The other difference was observed between 4/8 Alg_(H) and 5/8 Alg_(H) (1.52). All the experimental samples' stress at break values differed statistically from the control sample

(6.73 kPa). In the experimental samples, the only difference in stress at break values was observed between fibers of 2/8 Alg_(H) (1.52 kPa) and 3/8 Alg_(H) (2.55 kPa). The bar plots showing statistical differences of the strain and stress at break values are shown in Fig. 4.16.

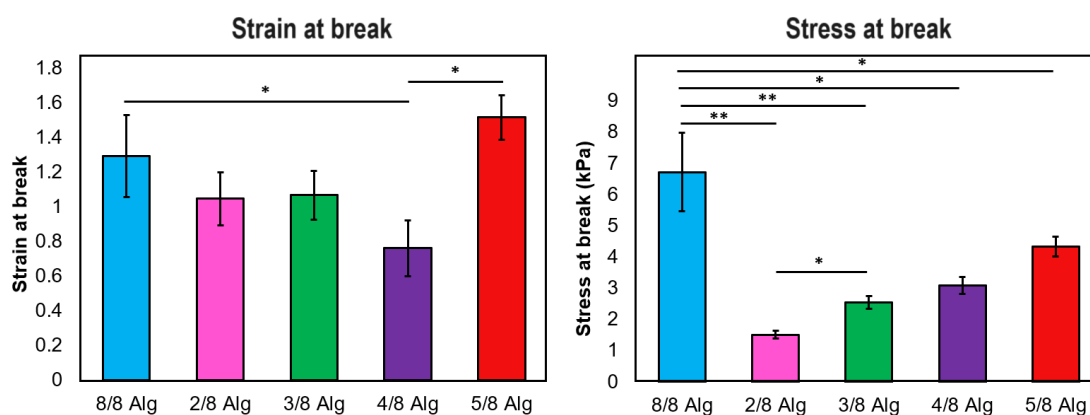


FIGURE 4.16: Bar plots representing statistical significance between values of strain at break (left) and stress at break (right) of fibers with different proportions of Alg_(H) layers.

According to these results, the optimal proportion of Alg_(H) inside the fibers must be between 3/8 and 4/8. As this work focuses on increasing the mechanical properties of the construct while preserving as many cell-adhesive layers as possible, a hollow fiber with an Alg_(H) proportion of 3/8 was chosen as optimal. This fiber proportion was used for the last set of tensile tests.

4.2.3 The concentration of Alg(H)

The final set of tensile assays involved optimizing Alg_(H) concentration. The reinforced hollow fibers used in this section had the optimal proportion of Alg_(H) layers (3/8 of Alg_(H)). The conceptual crosssection of this fiber is shown in the stress-strain curve (Fig. 4.17), where the light blue layers correspond to Alg_(H), orange to

GelMA/Alg_(L), and black to HEC.

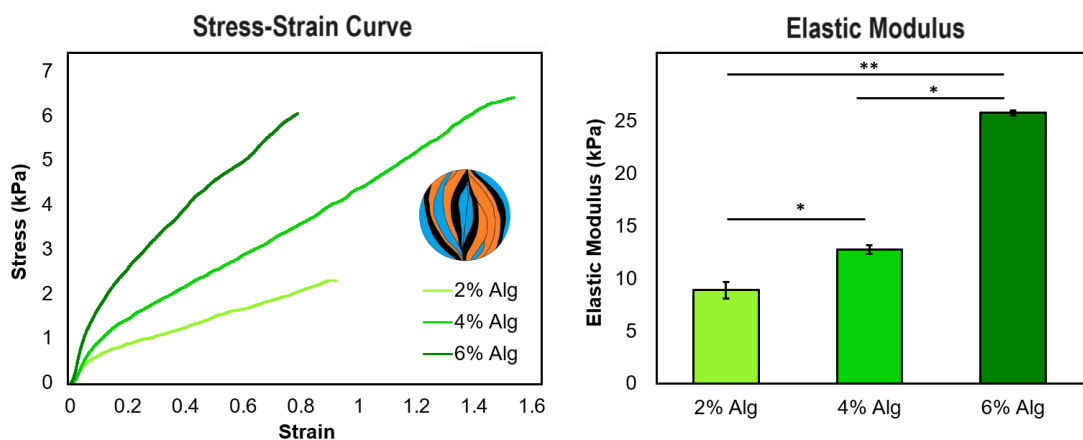


FIGURE 4.17: Mechanical properties of hydrogel fibers with different concentration of Alg_(H). The stress-strain curve (left) and bar plot show the statistical significance between elastic modulus values (right).

The hydrogel fibers' mechanical properties increased as the Alg_(H) concentration increased, and the stress-strain curve showed a similar slope in the linear region of the curve between 2% and 4%. However, the slope significantly increased when Alg_(H) at 6% was used. The fiber with 6% was stiffer but also had limited stretch. The ANOVA test showed that the elastic modulus values significantly differed between samples that used Alg_(H) 4% (12.80 kPa) and 6% (25.83 kPa).

The fiber with higher deformability corresponded to the one with 4% alginate, as it had a higher strain at break. The strain at break values had a meaningful difference between Alg_(H) 2% (1.07) and 4% (1.54), and between Alg_(H) 4% and 6% (0.86). The stress values at break showed significance between the first two concentrations but did not show any significance between Alg_(H) 4% (6.96 kPa) and 6% (7.05 kPa). This was due to the relatively high standard deviation of the values related to the 6% concentration (± 2.55). The bar plots showing statistical differences

of the strain and stress at break values are shown in Fig. 4.18.

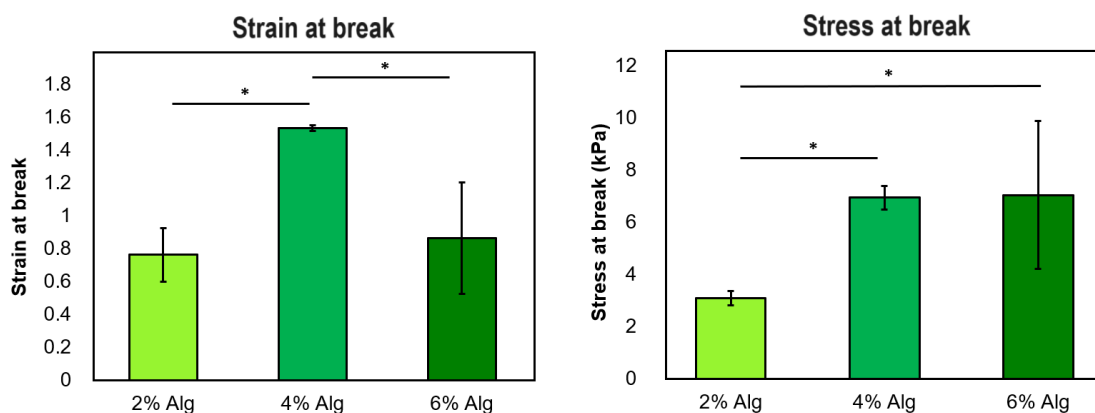


FIGURE 4.18: Bar plots representing statistical significance between values of strain at break and stress at break of fibers with different concentrations of $\text{Alg}_{(H)}$.

These results showed that a higher alginate concentration provided a more mechanically stable and stiffer fiber. However, if the purpose is to fabricate a more deformable and elastic muscle, the concentration of 4% alginate is more appropriate. Choosing between these two concentrations depends on the final application of the fiber: a stiffer or more deformable skeletal muscle fiber. The elastic modulus of a human skeletal muscle fiber is around 10-40 kPa[110]. Therefore, either 4% (w/m) or 6% (w/m) of $\text{Alg}_{(H)}$ can be used, as both have an elastic modulus of 13 and 25 kPa, respectively. $\text{Alg}_{(H)}$ 4% (w/m) was chosen for further degradation experiments since it had the optimal concentration to provide enough resistance while maintaining a deformable surface that has enough cell-adhesive layers for cell growth and expansion of mouse myoblasts.

In summary, the optimized reinforced hollow fibers had ink proportions of 3/8 $\text{Alg}_{(H)}$ 4% (w/m) (structural ink), 3/8 GelMA/ $\text{Alg}_{(L)}$ (cell-loaded bioink), and 2/8 HEC (sacrificial ink). The optimized fiber had an elastic modulus of 12.8 kPa, consistent with the values of a mature muscle-like construct with void channels

(14.7 kPa) reported by Filippi et al. in 2023 [25]. Other reports that used chaotic bioprinting to fabricate skeletal muscle fibers did not report elastic modulus values [21],[14],[15].

4.3 Degradation of fibers under continuous agitation

To evaluate erosion under agitation, experimental and control hydrogel fibers were printed following chaotic printing protocols. Afterward, each fiber was placed inside the DIY bioreactor to simulate 3D culture conditions with continuous agitation to evaluate their degradation. To measure degradation, the remaining mass of each fiber was measured over a period of time. Decreasing values of the remaining mass indicates mass loss and, therefore, quantifies the degradation of the fibers over time. Each fiber had a different proportion of structural material, while the presence of hollow channels also varied. Both parameters influenced the loss of mass and, therefore, the degradation of the fibers.

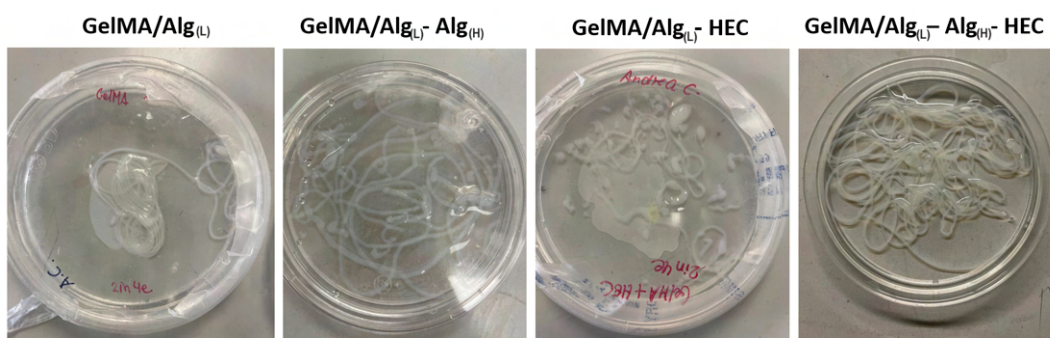


FIGURE 4.19: Printed fibers for degradation experiments. Left to right: unreinforced solid fibers (control 1), reinforced solid fibers (control 2), unreinforced hollow fibers (control 3), reinforced hollow fibers (treatment).

The experimental sample was the reinforced hollow fiber that was mechanically optimized after tensile assays. The control samples were unreinforced hollow

fibers (hollow fibers without $\text{Alg}_{(H)}$ layers), reinforced solid fibers (fibers without void microchannels but with $\text{Alg}_{(L)}$ layers), and unreinforced solid fibers (fibers made of just GelMA/ $\text{Alg}_{(L)}$). The experimental and control samples were printed successfully following chaotic printing protocols (Fig. 4.19).

The fibers containing alginate reinforcement (with at least one inlet with $\text{Alg}_{(H)}$ 4% (w/v) in the printhead) resisted more time in continuous agitation than solid and hollow fibers without alginate reinforcement. The hollow fibers without alginate reinforcement (GelMA/ $\text{Alg}_{(L)}$ -HEC) completely degraded after 24 h of continuous agitation submerged in PBS. Meanwhile, solid fibers without alginate reinforcement (GelMA/ $\text{Alg}_{(L)}$) completely degraded after 72 h of continuous agitation. The solid fibers with alginate reinforcement (GelMA/ $\text{Alg}_{(L)}$ - $\text{Alg}_{(H)}$) and hollow fibers with alginate reinforcement (GelMA/ $\text{Alg}_{(L)}$ - HEC- $\text{Alg}_{(H)}$) maintained more than 65% of their mass after 72 h of agitation.

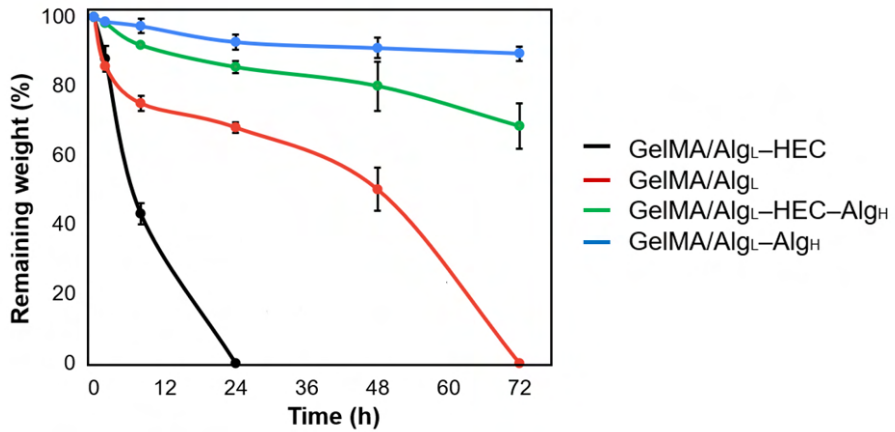


FIGURE 4.20: Remaining weight of fibers in the first 72 hours of agitation in a rocking bioreactor.

Despite having layers of structural hydrogel ($\text{Alg}_{(H)}$), reinforced hollow fibers lost more mass (remaining weight=68.5%) than reinforced solid fibers (remaining weight=89.4%). This could have happened due to the presence of void channels

inside the construct, which led to perfusion and erosion in the internal walls of the fiber. Additionally, reinforced solid fibers had a higher proportion of alginate ($1/2$ or $4/8$ Alg_(H)), while reinforced hollow fibers contained less alginate ($3/8$ Alg_(H)). A higher proportion of alginate resulted in better mechanical stability and a higher percentage of remaining mass after agitation. The remaining weight (%) curves can be shown in Fig. 4.20.

In summary, the reinforced solid fibers ((GelMA/Alg_(L)-Alg_(H)) had the most remaining mass after 72 h of continuous agitation compared to the rest of the printed fibers. Therefore, these fibers were chosen as a control for bioprinting experiments using cells.

4.4 Cell viability in static culture

Assessing cell viability is crucial in 3D bioprinting, as it is the primary indicator of whether the materials used, their composition, and their distribution support adequate cell growth. The cell viability experiments began with 2D cell culturing for cell expansion. Then, it involved the chaotic bioprinting of experimental and control samples containing cells. Both samples were cultured in static conditions in an incubator for 14 days. Finally, cell viability was assessed with live/dead staining. Live/dead staining provides qualitative information about the number of live (green) and dead (red) cells within the fibers. The use of ImageJ was necessary to convert this information from qualitative to quantitative. In this way, viability values were obtained in the form of percentages, which could then be statistically analyzed to identify differences in cell viability between samples.

4.4.1 Chaotic bioprinting

The C2C12 cells reached 70% confluence in 2D culture under the applied culture conditions. This is shown in Fig. 4.21, in which the cells show a significant expansion in the T25 12-well plate. The cell expansion was repeated after obtaining the necessary amount of cells (3 million cells per milliliter of cell-adhesive bioink). The experimental samples were reinforced hollow fibers with optimized mechanical properties. The control samples consisted of the fibers that withstood the agitation best in the degradation experiments best. They consisted of 1/2 Alg_(H) and 1/2 GelMA/Alg_(L). The detailed bioprinting strategy was consolidated after mechanical optimization. The conceptual crosssections of control and experimental samples are described in Fig. 4.22.

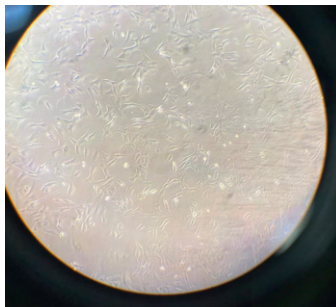


FIGURE 4.21: Mouse myoblasts at 70% confluence

The cells attached successfully to the optimized reinforced hollow fiber selected after tensile assays and degradation experiments (Fig. 4.23). The cells preserved their shape after printing and were unaffected by the chaotic flows.

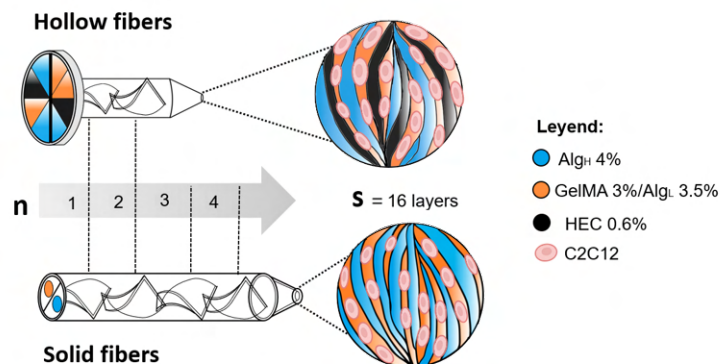


FIGURE 4.22: Bioprinting of the control sample (left). Bioprinting of the optimized-reinforced hollow fiber (right).

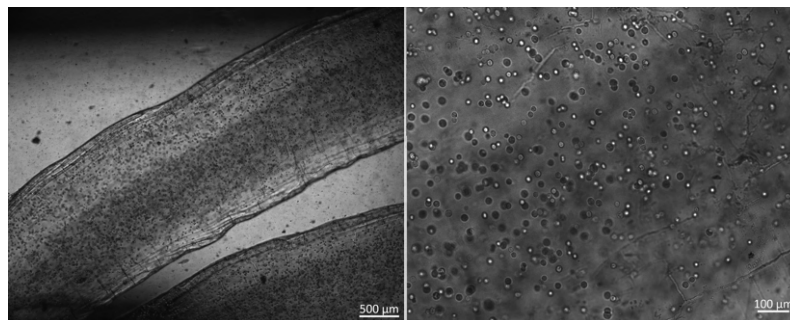


FIGURE 4.23: Chaotically bioprinted hydrogel fiber at day 1 (left). Embedded C2C12 cells in the hydrogel fiber (right).

4.4.2 Cell viability assessment

Fluorescence microscopy images for days 1, 7 and 14 showed live (green) and dead (red) cells (Fig. 4.24). Quantitatively, the number of live cells was higher on days 7 and 14. The sample with the highest number of dead cells was the solid fiber on day 1. The reinforced hollow fibers showed a cell viability of more than 90% compared to the solid fibers at days 7 and 14 of static culture (>80%). Moreover, cell viability improved between days 1, 7, and 14 in the hollow fibers in static culture. In the solid fibers, cell viability increased between days 1 and 7, but between days 7 and

14, the viability remained nearly the same (around 80-85%).

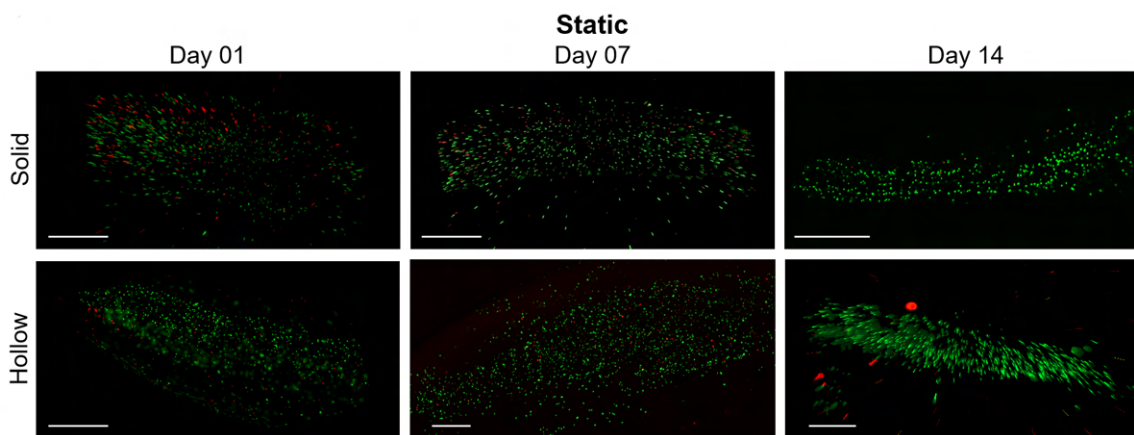


FIGURE 4.24: Live/Dead staining of solid and hollow fibers in static culture at days 1, 7, and 14. Scale bar: 500 μm .

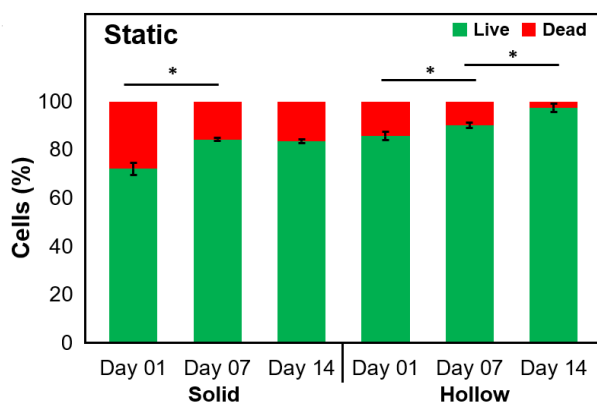


FIGURE 4.25: Statistical analysis of cell viability of fibers in static culture

These results indicated that void microchannels inside reinforced hollow fibers improve cell viability in static culture. These findings are consistent with Bolivar et al., who showed that the presence of hollowed microchannels enhances the viability of C2C12 cells due to improved mass transfer of nutrients and gases[15]. However, their fibers degraded after 7 days of static culture due to poor mechanical properties, which is not enough time to achieve skeletal muscle tissue maturation. The optimized

reinforced hollow fibers that were fabricated in this study withstood at least 14 days of static culture. Fan et al.[111] and Lee et al.[19] reported constructs with cell viability of >90%, but only for days 3 and 7 in tiny fibers (10-100 μm in width). Hwangbo et al. reported cell viability of >90% for days 1 and 3[22], but the cell viability of their constructs in the long term is unknown. Lee et al. reported cell viability of 86% in their constructs[23], which is less than the cell viability of the reinforced hollow fibers.

4.5 Cell alignment in static culture

Cell alignment was evaluated in the hydrogel fibers from the static culture. This assessment was done because the degree of alignment of the cells in the early stages of maturation can determine if the tissue will be functional. To evaluate cell alignment, fibers were printed with cells, as described in the previous section. Then, the actin filaments and the cell nucleus were visualized using actin/DAPI staining.

First, cell spreading was assessed to determine if the cells were attached and extended along the hydrogel fiber. Cell spreading was evaluated by observing actin filaments and cell flattening in the microscope. Actin filaments are more visible in cells that have adequately adhered to the biomaterial and are beginning to differentiate. The length of actin filaments serves as an indicator of the degree of adherence and differentiation of the myoblasts. Conversely, the nucleus undergoes expansion upon cell attachment and initiation of the differentiation process.

Although it is necessary to know the orientation in 2D images, it is also crucial to know the distribution of cells in 3D space. This is because the fibers have a diameter of 1 mm, and ideally, cell spreading should be visualized throughout the entire volume of the fiber. To know the distribution of cells inside the fiber, images

were taken using the z-stack. Z-stack is a functionality of the Zeiss microscope that takes images layer by layer until obtaining a single 3D image.

Finally, image processing tools help calculate the degree of orientation of actin filaments in 2D images. To indicate good cell alignment, it is preferred that the majority of filaments be oriented towards the 0° degree with respect to the hydrogel fiber.

4.5.1 Cell spreading

Cell spreading was evaluated to determine whether the C2C12 cells attached to the reinforced fibers' GelMA/Alg_(L) layers in static culture. The cells remained spherical during the first 7 days of culture in solid and hollow reinforced fibers. This was due to the Alg_(H) layers, which created a stiffer environment for this cell type and delayed their spreading processes. Consequently, there was a lack of actin filaments, and the actin fluorescence signal was low. Meanwhile, cell spreading in both fibers was finally observed after 14 days of culture. Actin/DAPI staining images that show the actin filaments (red) and cell nucleus (blue) are shown in Fig. 4.26.

It has not yet been elucidated whether the cells spread within the GelMA/Alg_(L) compartments in the core parts of the fiber or only at the surface. Although the solid fibers seemed to showcase improved cell spreading at day 14, this was not necessarily the case. The 2D images provided limited information about the volumetric distribution of the cells inside the fiber because they only showed the upper part of the fiber. Fig. 4.27 shows how the cell spread only on the surface of the reinforced solid fiber, and the layer formed by cells was not deeper than $50\ \mu\text{m}$. A 360° video of this fiber can be found in Appendix 4. Bolivar et al. reported similar results for reinforced solid fibers at day 28, where the cells spread just on the fiber's surface

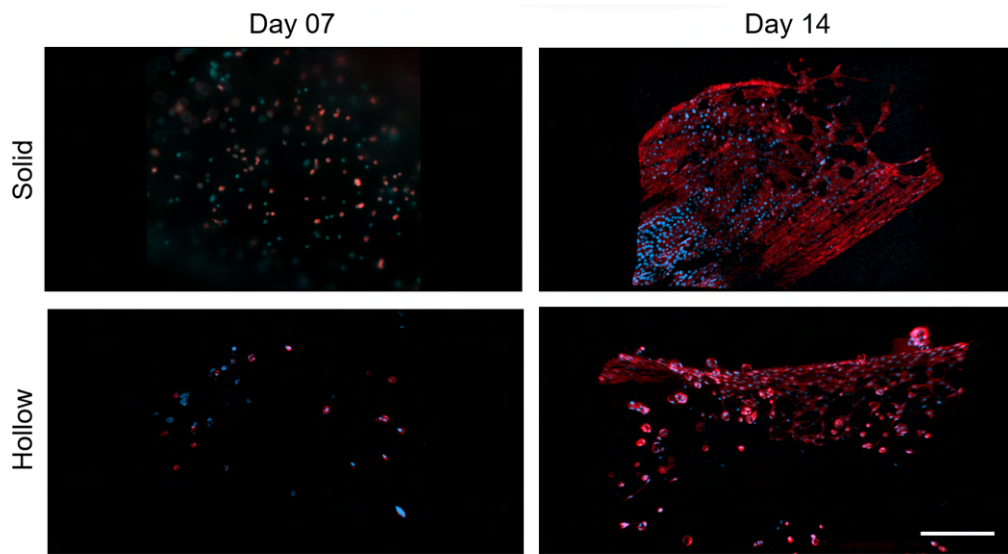


FIGURE 4.26: Actin/DAPI of reinforced hollow fibers at days 7 and 14

and resembled a crust.

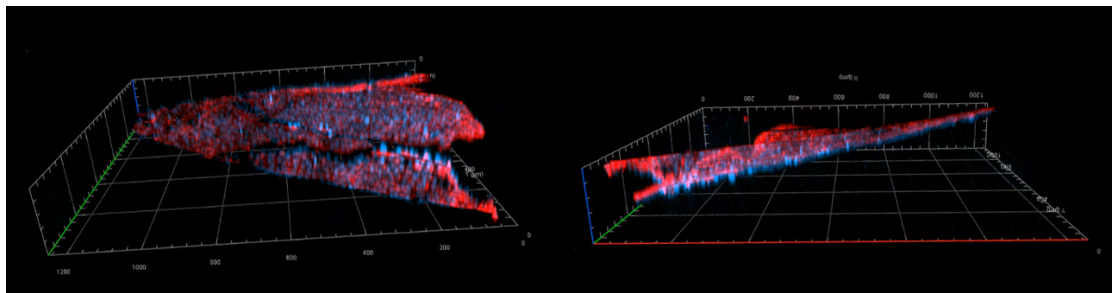


FIGURE 4.27: Actin/DAPI of solid fibers at day 14

Void microchannels improved the perfusion of nutrients to cells in the fiber, including the core. Therefore, Fig. 4.28 shows that spread cells were seen until 400 μm deep within the fibers' core on day 14. They surrounded a higher surface area than solid fibers, and the fiber's shape were distinguished in the Actin/DAPI images due to the spread cells along the surface. A 360° video of this fiber can be found in Appendix 5.

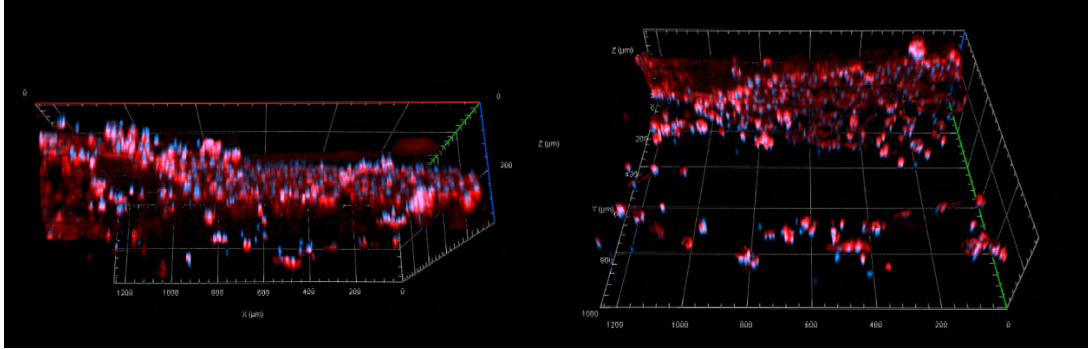


FIGURE 4.28: Actin/DAPI of reinforced hollow fibers at day 14

4.5.2 Cell orientation

Cell orientation of reinforced solid and hollow fibers was evaluated by extracting data from the Actin/DAPI staining images. Fig. 4.29 depicts polar diagrams showing the direction of the cells on each sample. The orientation of reinforced solid and hollow fibers was random at day 7 because there were not enough actin filaments to show a clear direction. Hollow fibers were not as dispersed as solid ones but did not have a clear direction. At least 10% of the cells of solid and hollow fibers were in random directions.

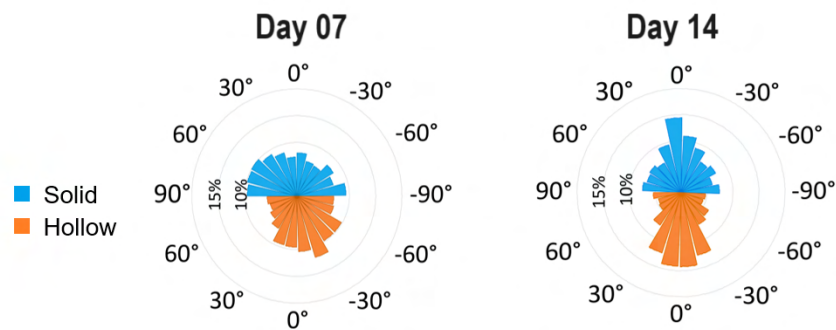


FIGURE 4.29: Actin/DAPI of reinforced hollow fibers at days 7 and 14

Both fibers had better alignment on day 14. Both fibers showed cell orientation between -30° and 30° . In solid fibers, 15% of cells orientated towards 0° .

However, that orientation is only on the fiber's surface, as shown by Fig. 4.27. On the other hand, hollow fibers had approximately 30% of cells orientated from -10° to 10° . Other cells (24%) were orientated on -30° or 30° .

4.6 Cell viability in agitated culture

The sixth specific objective seeks to describe whether culture with continuous agitation improves cell viability. To do this, the fibers were printed with cells and cultured with shaking for 7 days. Fibers that were cultured in static mode served as a control. Live/dead staining was performed on both samples. The photos were obtained in the microscope. Subsequently, image processing was carried out to determine the percentage of viable cells, followed by the application of relevant statistical analyses.

The live/dead images showed significant live cells (green) on days 1 and 7. Qualitatively, both fibers had more live cells on day 7. The number of live cells in all the images indicates a higher cell proliferation than in fibers in static culture. Cells had a considerable volumetric proliferation in all the fiber, including the surface and across $800\ \mu\text{m}$ deep. A 360° video of live and dead cells of reinforced hollow fibers is in Appendix 6. A similar video for reinforced solid fibers is in Appendix 7. Fig. 4.30 contains representative 2D images from all samples.

Generally, both fibers had higher cell viability when cultured under continuous agitation than when they were cultured in static mode. Cell viability in agitated culture ($>95\%$) was higher on days 1 and 7 than in static culture in both fibers. The statistical differences between static and agitated cultures were observed for solid fibers between days 1 and 7. The difference was only observed on day 7 for reinforced hollow fibers (Fig. 4.31).

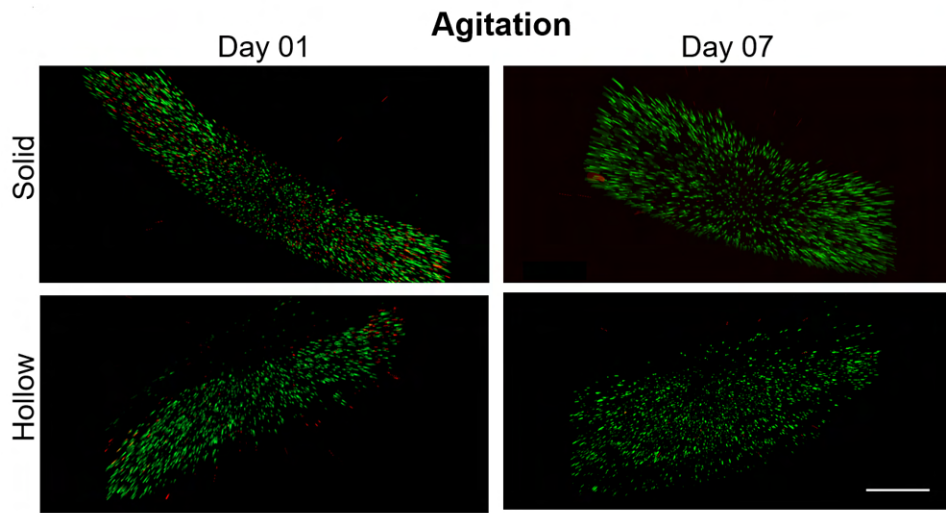


FIGURE 4.30: Live/Dead staining of solid and hollow fibers in agitated culture at day 1 and 7.

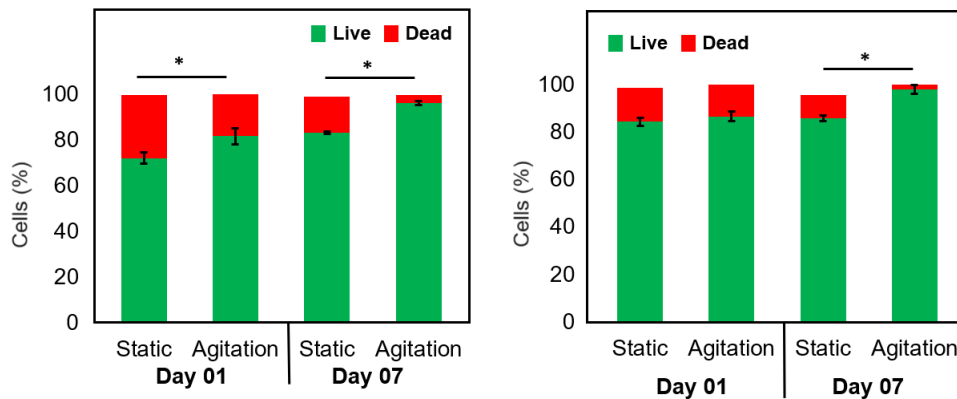


FIGURE 4.31: Statistical analysis of cell viability of fibers in culture under agitation

In summary, continuous agitation improved cell viability in both samples compared to cells grown in static culture. These results demonstrated again that culturing cells in a bioreactor enhanced cell growth. The seminal work of Freed and coworkers demonstrated the same by calculating the doubling time of cells and the proliferation rate inside a stirred tank bioreactor[31]. Subsequent works of Li et al. and Nguyen et al. demonstrated that the constant agitation induced better perfusion

of the medium inside the printed construct and improved cell viability[35],[34].

CONCLUSIONS

In brief, chaotic bioprinting could be optimized to create reinforced multichannel hydrogel fibers for skeletal muscle tissue maturation in a rocking bioreactor in an economical fashion and at high throughput. It was concluded that:

- Chaotic printing allowed to manufacture reinforced hollow fibers with three inks of different viscosity (structural, matrix, and sacrificial) using a KSM printhead that created chaotic flows in a predictable pattern. The distribution of layers in the hydrogel fibers was predictable since the computational cross-sections were similar to the experimental images.
- Tensile tests allowed the design of a reinforced hollow fiber with optimal mechanical properties. The optimal proportion of the number of voids, proportion of Alg_(H) layers, and Alg_(H) concentration was found to improve the mechanical properties without altering other characteristics of biological relevance. The optimized fiber had an elastic modulus of 12.8 kPa and was made of 3/8 Alg_(H), 3/8 GelMA/Alg_(L), and 2/8 HEC.
- Degradation tests demonstrated that the optimized reinforced hollow fibers could withstand continuous agitation in a rocking bioreactor for 3 consecutive days, retaining at least 65% of its mass.
- Reinforced hollow fibers had higher cell viability at day 14 (>90%) than reinforced solid fibers because they have void microchannels that simulate the functionality of native blood vessels in human tissues.
- Both solid and hollow fibers in static culture demonstrated a degree of alignment between -30° to 30° at day 14 of culture. This was a sign that the fibers would be functional once they had matured through extended culture processes.

- Culture under continuous agitation in a rocking bioreactor improved cell viability compared to static culture, reaching values of >95%. Agitation improved the cell viability of solid and hollow reinforced fibers.

For future research, the static and agitated cell culture time can be increased until day 28 to evaluate tissue maturation. One way to evaluate tissue maturation is through immunostaining to visualize specific biomarkers, such as sarcomeric actin, by fluorescence. A more quantitative way to evaluate tissue maturation is through qPCR. Specifically, reverse transcription qPCR (RT-qPCR) should be done to quantify the amount of messenger RNA (mRNA) that expresses specific differentiation genes. Each stage of muscle differentiation has associated genetic expression markers. In this way, the precise state of tissue maturation can be known.

RECOMENDATIONS

First, the proposed system for chaotic bioprinting provides little control for printing on the X, Y, and Z axes. This is because the printing position depends on the person manually manipulating the system. One solution to this problem is to adapt the KSM head to a commercial bioprinter like BioX. Second, the system is applicable only for printing fibers. Therefore, crosslinking the fibers after printing is recommended to obtain more elaborate, human-like tissues and organs with a clinically relevant size. Third, the diameter of the fibers is always 1 mm, as it directly depends on the diameter of the KSM nozzle. Nanopipettes connected to the KSM nozzle could be explored to decrease the fiber's diameter. By using nanopipettes, higher resolutions in printed constructs can be achieved. Moreover, the syringe pump should be automated, as it depends on the person operating it. This leads to more time-consuming and imprecise bioprinting processes. This could be solved by fabricating a DIY syringe pump with a control system. Agglomerations can appear in the fibers when three or more materials are used. Therefore, the rate of velocity should be decreased while printing with multiple hydrogels simultaneously.

BIBLIOGRAPHY

- [1] C. Mandrycky, Z. Wang, K. Kim, and D.-H. Kim, “3d bioprinting for engineering complex tissues,” *Biotechnology advances*, vol. 34, no. 4, pp. 422–434, 2016.
- [2] S. Mantha, S. Pillai, P. Khayambashi, A. Upadhyay, Y. Zhang, O. Tao, H. M. Pham, and S. D. Tran, “Smart hydrogels in tissue engineering and regenerative medicine,” *Materials*, vol. 12, no. 20, p. 3323, 2019.
- [3] B. Tan, S. Gan, X. Wang, W. Liu, and X. Li, “Applications of 3d bioprinting in tissue engineering: advantages, deficiencies, improvements, and future perspectives,” *Journal of Materials Chemistry B*, vol. 9, no. 27, pp. 5385–5413, 2021.
- [4] Z. Wang, Z. Wei, K. Sun, S. He, H. Wang, Q. Xu, and M. Chen, “Chaotic flows with special equilibria,” *The European Physical Journal Special Topics*, vol. 229, no. 6, pp. 905–919, 2020.
- [5] C. Chávez-Madero, M. D. de León-Derby, M. Samandari, C. F. Ceballos-González, E. J. Bolívar-Monsalve, C. Mendoza-Buenrostro, S. Holmberg, N. A. Garza-Flores, M. A. Almajhadi, I. González-Gamboa *et al.*, “Using chaotic advection for facile high-throughput fabrication of ordered multilayer micro-and nanostructures: Continuous chaotic printing,” *Biofabrication*, vol. 12, no. 3, p. 035023, 2020.

- [6] “Musculoskeletal health,” Jul 2022. [Online]. Available: <https://www.who.int/news-room/fact-sheets/detail/musculoskeletal-conditions>
- [7] S. Safiri, A.-A. Kolahi, M. Cross, C. Hill, E. Smith, K. Carson-Chahhoud, M. A. Mansournia, A. Almasi-Hashiani, A. Ashrafi-Asgarabad, J. Kaufman *et al.*, “Prevalence, deaths, and disability-adjusted life years due to musculoskeletal disorders for 195 countries and territories 1990–2017,” *Arthritis & Rheumatology*, vol. 73, no. 4, pp. 702–714, 2021.
- [8] Statista, “Peru: hospitalizations due to musculoskeletal diseases 2017, by gender and age,” 2017. [Online]. Available: <https://www.statista.com/statistics/835556/number-individuals-hospitalized-musculoskeletal-disease-peru-gender-age/#statisticContainer>
- [9] —, “Treatment of musculoskeletal diseases - peru — forecast,” 2024. [Online]. Available: <https://www.statista.com/outlook/hmo/hospitals/inpatient-care/treatment-of-musculoskeletal-diseases/peru>
- [10] X. Xu, K. J. Wilschut, G. Kouklis, H. Tian, R. Hesse, C. Garland, H. Sbitany, S. Hansen, R. Seth, P. D. Knott *et al.*, “Human satellite cell transplantation and regeneration from diverse skeletal muscles,” *Stem cell reports*, vol. 5, no. 3, pp. 419–434, 2015.
- [11] B. T. Corona, K. Garg, C. L. Ward, J. S. McDaniel, T. J. Walters, and C. R. Rathbone, “Autologous minced muscle grafts: a tissue engineering therapy for the volumetric loss of skeletal muscle,” *American Journal of Physiology-Cell Physiology*, vol. 305, no. 7, pp. C761–C775, 2013.
- [12] A. L. Rutz, P. L. Lewis, and R. N. Shah, “Toward next-generation bioinks: tuning material properties pre-and post-printing to optimize cell viability,” *MRS Bulletin*, vol. 42, no. 8, pp. 563–570, 2017.

- [13] C. M. Hwang, S. Sant, M. Masaeli, N. N. Kachouie, B. Zamanian, S.-H. Lee, and A. Khademhosseini, "Fabrication of three-dimensional porous cell-laden hydrogel for tissue engineering," *Biofabrication*, vol. 2, no. 3, p. 035003, 2010.
- [14] E. J. Bolivar-Monsalve, C. F. Ceballos-Gonzalez, K. I. Borrayo-Montano, D. A. Quevedo-Moreno, J. F. Yee-de Leon, A. Khademhosseini, P. S. Weiss, M. M. Alvarez, and G. Trujillo-de Santiago, "Continuous chaotic bioprinting of skeletal muscle-like constructs," *Bioprinting*, vol. 21, p. e00125, 2021.
- [15] E. J. Bolívar-Monsalve, C. F. Ceballos-González, C. Chávez-Madero, B. G. de la Cruz-Rivas, S. Velásquez Marín, S. Mora-Godínez, L. M. Reyes-Cortés, A. Khademhosseini, P. S. Weiss, M. Samandari *et al.*, "One-step bioprinting of multi-channel hydrogel filaments using chaotic advection: Fabrication of pre-vascularized muscle-like tissues," *Advanced Healthcare Materials*, p. 2200448, 2022.
- [16] A. Anand, S. P. Mallick, B. N. Singh, S. Kumari, D. K. Suman, S. Tripathi, D. Singh, and P. Srivastava, "A critical aspect of bioreactor designing and its application for the generation of tissue engineered construct: Emphasis on clinical translation of bioreactor," *Biotechnology and Bioprocess Engineering*, vol. 27, no. 4, pp. 494–514, 2022.
- [17] M. G. Sánchez-Salazar, R. Crespo-López Oliver, S. Ramos-Meizoso, V. S. Jerezano-Flores, S. Gallegos-Martínez, E. J. Bolívar-Monsalve, C. F. Ceballos-González, G. Trujillo-de Santiago, and M. M. Álvarez, "3d-printed tumor-on-chip for the culture of colorectal cancer microspheres: Mass transport characterization and anti-cancer drug assays," *Bioengineering*, vol. 10, no. 5, p. 554, 2023.

- [18] T. Fan, S. Wang, Z. Jiang, S. Ji, W. Cao, W. Liu, Y. Ji, Y. Li, N. Shyh-Chang, and Q. Gu, “Controllable assembly of skeletal muscle-like bundles through 3d bioprinting,” *Biofabrication*, vol. 14, no. 1, p. 015009, 2021.
- [19] H. Lee, W. Kim, J. Lee, K. S. Park, J. J. Yoo, A. Atala, G. H. Kim, and S. J. Lee, “Self-aligned myofibers in 3d bioprinted extracellular matrix-based construct accelerate skeletal muscle function restoration,” *Applied Physics Reviews*, vol. 8, no. 2, 2021.
- [20] S. Boularaoui, G. Al Hussein, K. A. Khan, N. Christoforou, and C. Stefanini, “An overview of extrusion-based bioprinting with a focus on induced shear stress and its effect on cell viability,” *Bioprinting*, vol. 20, p. e00093, 2020.
- [21] A. I. Frías-Sánchez, D. A. Quevedo-Moreno, M. Samandari, J. A. Tavares-Negrete, V. H. Sánchez-Rodríguez, I. González-Gamboa, F. Ponz, M. M. Alvarez, and G. Trujillo-de Santiago, “Biofabrication of muscle fibers enhanced with plant viral nanoparticles using surface chaotic flows,” *Biofabrication*, vol. 13, no. 3, p. 035015, 2021.
- [22] H. Hwangbo, H. Lee, E.-J. Jin, J. Lee, Y. Jo, D. Ryu, and G. Kim, “Bioprinting of aligned gelma-based cell-laden structure for muscle tissue regeneration,” *Bioactive materials*, vol. 8, pp. 57–70, 2022.
- [23] H. Lee, S. H. Kim, J. S. Lee, Y. J. Lee, O. J. Lee, O. Ajiteru, M. T. Sultan, S. W. Lee, and C. H. Park, “Functional skeletal muscle regeneration using muscle mimetic tissue fabricated by microvalve-assisted coaxial 3d bioprinting,” *Advanced Healthcare Materials*, vol. 12, no. 7, p. 2202664, 2023.
- [24] T. Li, J. Hou, L. Wang, G. Zeng, Z. Wang, L. Yu, Q. Yang, J. Yin, M. Long, L. Chen *et al.*, “Bioprinted anisotropic scaffolds with fast stress relaxation bioink for engineering 3d skeletal muscle and repairing volumetric muscle loss,” *Acta Biomaterialia*, vol. 156, pp. 21–36, 2023.

- [25] M. Filippi, O. Yasa, J. Giachino, R. Graf, A. Balciunaite, L. Stefani, and R. K. Katzschmann, “Perfusable biohybrid designs for bioprinted skeletal muscle tissue,” *Advanced Healthcare Materials*, p. 2300151, 2023.
- [26] J. Lee, H. Lee, E.-J. Jin, D. Ryu, and G. H. Kim, “3d bioprinting using a new photo-crosslinking method for muscle tissue restoration,” *NPJ Regenerative Medicine*, vol. 8, no. 1, p. 18, 2023.
- [27] R. Langer and J. P. Vacanti, “Tissue engineering,” *Science*, vol. 260, no. 5110, pp. 920–926, 1993. [Online]. Available: <https://www.science.org/doi/abs/10.1126/science.8493529>
- [28] R. Foresti, S. Rossi, S. Pinelli, R. Alinovi, M. Barozzi, C. Sciancalepore, M. Galetti, C. Caffarra, P. Lagonegro, G. Scavia *et al.*, “Highly-defined bio-printing of long-term vascularized scaffolds with bio-trap: Complex geometry functionalization and process parameters with computer aided tissue engineering,” *Materialia*, vol. 9, p. 100560, 2020.
- [29] Y.-J. Choi, Y.-J. Jun, D. Y. Kim, H.-G. Yi, S.-H. Chae, J. Kang, J. Lee, G. Gao, J.-S. Kong, J. Jang *et al.*, “A 3d cell printed muscle construct with tissue-derived bioink for the treatment of volumetric muscle loss,” *Biomaterials*, vol. 206, pp. 160–169, 2019.
- [30] H. Cui, W. Zhu, Y. Huang, C. Liu, Z.-X. Yu, M. Nowicki, S. Miao, Y. Cheng, X. Zhou, S.-J. Lee *et al.*, “In vitro and in vivo evaluation of 3d bioprinted small-diameter vasculature with smooth muscle and endothelium,” *Biofabrication*, vol. 12, no. 1, p. 015004, 2019.
- [31] L. Freed, G. Vunjak-Novakovic, and R. Langer, “Cultivation of cell-polymer cartilage implants in bioreactors,” *Journal of cellular biochemistry*, vol. 51, no. 3, pp. 257–264, 1993.

- [32] J. C. Silva, C. S. Moura, G. Borrecho, A. P. A. de Matos, C. L. da Silva, J. M. Cabral, P. J. Bártolo, R. J. Linhardt, and F. C. Ferreira, “Extruded bioreactor perfusion culture supports the chondrogenic differentiation of human mesenchymal stem/stromal cells in 3d porous poly (ε-caprolactone) scaffolds,” *Biotechnology journal*, vol. 15, no. 2, p. 1900078, 2020.
- [33] J. Liu, H. Zheng, X. Dai, P. S. Poh, H.-G. Machens, and A. F. Schilling, “Transparent pdms bioreactors for the fabrication and analysis of multi-layer pre-vascularized hydrogels under continuous perfusion,” *Frontiers in Bioengineering and Biotechnology*, vol. 8, p. 568934, 2020.
- [34] J. H. Nguyen, J. D. Chung, G. S. Lynch, and J. G. Ryall, “The microenvironment is a critical regulator of muscle stem cell activation and proliferation,” *Frontiers in cell and developmental biology*, vol. 7, p. 254, 2019.
- [35] N. Li, A. P. Rickel, H. J. Sanyour, and Z. Hong, “Vessel graft fabricated by the on-site differentiation of human mesenchymal stem cells towards vascular cells on vascular extracellular matrix scaffold under mechanical stimulation in a rotary bioreactor,” *Journal of Materials Chemistry B*, vol. 7, no. 16, pp. 2703–2713, 2019.
- [36] M. E. Carnes and G. D. Pins, “Skeletal muscle tissue engineering: biomaterials-based strategies for the treatment of volumetric muscle loss,” *Bioengineering*, vol. 7, no. 3, p. 85, 2020.
- [37] B. M. Sicari, R. Londono, and S. F. Badylak, “Strategies for skeletal muscle tissue engineering: seed vs. soil,” *Journal of Materials Chemistry B*, vol. 3, no. 40, pp. 7881–7895, 2015.
- [38] M. Akinrodoye and F. Lui. (2022) Neuroanatomy, somatic nervous system. <https://www.ncbi.nlm.nih.gov/books/NBK556027/>. Treasure Island, FL. Accessed: 17/10/2023.

- [39] H. Ömeroğlu and S. Ömeroğlu, “Skeletal muscle; structure, function, and repair,” in *Musculoskeletal Research and Basic Science*. Springer, 2016, pp. 443–451.
- [40] H. B. Sarnat, “Ontogenesis of striated muscle,” in *Fetal and neonatal physiology*. Elsevier, 2017, pp. 1430–1450.
- [41] H. Yin, F. Price, and M. Rudnicki, “Satellite cells and the muscle stem cell niche,” *Physiol Rev*, vol. 93, no. 1, pp. 23–67, 2013.
- [42] H. N. Chang and M. Moo-Young, “Estimation of oxygen penetration depth in immobilized cells,” *Appl. Microbiol. Biotechnol.*, vol. 29, no. 2–3, pp. 107–112, 1988.
- [43] O. Cleaver and P. A. Krieg, “Molecular mechanisms of vascular development,” in *Heart development*. Elsevier, 1999, pp. 221–252.
- [44] J. O. Hollinger, *An introduction to biomaterials*. CRC press, 2011.
- [45] D. S. Kohane and R. Langer, “Polymeric biomaterials in tissue engineering,” *Pediatric research*, vol. 63, no. 5, pp. 487–491, 2008.
- [46] D. Green and B. Ben-Nissan, “Biomimetics: bio-inspired engineering of human tissue scaffolding for regenerative medicine,” in *Biomaterials in Asia: in commemoration of the 1st Asian Biomaterials Congress. Tsukuba, Japan, 2008*, pp. 364–385.
- [47] K. H. Nakayama, M. Shayan, and N. F. Huang, “Engineering biomimetic materials for skeletal muscle repair and regeneration,” *Advanced healthcare materials*, vol. 8, no. 5, p. 1801168, 2019.
- [48] A. De Pieri, Y. Rochev, and D. I. Zeugolis, “Scaffold-free cell-based tissue engineering therapies: Advances, shortfalls and forecast,” *NPJ Regenerative Medicine*, vol. 6, no. 1, p. 18, 2021.

- [49] B. Kaczmarek, K. Nadolna, and A. Owczarek, “The physical and chemical properties of hydrogels based on natural polymers,” *Hydrogels based on natural polymers*, pp. 151–172, 2020.
- [50] K. Wang, Y. Hao, Y. Wang, J. Chen, L. Mao, Y. Deng, J. Chen, S. Yuan, T. Zhang, J. Ren *et al.*, “Functional hydrogels and their application in drug delivery, biosensors, and tissue engineering,” *International Journal of Polymer Science*, vol. 2019, pp. 1–14, 2019.
- [51] O. Okay, “General properties of hydrogels,” *Hydrogel sensors and actuators: Engineering and technology*, pp. 1–14, 2010.
- [52] X. Duan, J. Yu, Y. Zhu, Z. Zheng, Q. Liao, Y. Xiao, Y. Li, Z. He, Y. Zhao, H. Wang *et al.*, “Large-scale spinning approach to engineering knittable hydrogel fiber for soft robots,” *ACS nano*, vol. 14, no. 11, pp. 14 929–14 938, 2020.
- [53] H. A. Reed, C. E. White, V. Rao, S. A. B. Allen, C. L. Henderson, and P. A. Kohl, “Fabrication of microchannels using polycarbonates as sacrificial materials,” *Journal of Micromechanics and Microengineering*, vol. 11, no. 6, p. 733, 2001.
- [54] S. Li, J. Jin, C. Zhang, X. Yang, Y. Liu, P. Lei, and Y. Hu, “3d bioprinting vascular networks in suspension baths,” *Applied Materials Today*, vol. 30, p. 101729, 2023.
- [55] S. Y. Sonaye, E. G. Ertugral, C. R. Kothapalli, and P. Sikder, “Extrusion 3d (bio) printing of alginate-gelatin-based composite scaffolds for skeletal muscle tissue engineering,” *Materials*, vol. 15, no. 22, p. 7945, 2022.
- [56] Y. J. Shin, R. T. Shafranek, J. H. Tsui, J. Walcott, A. Nelson, and D.-H. Kim, “3d bioprinting of mechanically tuned bioinks derived from cardiac decellularized extracellular matrix,” *Acta biomaterialia*, vol. 119, pp. 75–88, 2021.

- [57] A. B. Kakarla, I. Kong, C. Kong, and H. Irving, “Extrusion-based bioprinted boron nitride nanotubes reinforced alginate scaffolds: mechanical, printability and cell viability evaluation,” *Polymers*, vol. 14, no. 3, p. 486, 2022.
- [58] R. L. P. Adams, *Cell culture for biochemists*. Elsevier, 1990.
- [59] M. Kapałczyńska, T. Kolenda, W. Przybyła, M. Zajaczkowska, A. Teresiak, V. Filas, M. Ibbs, R. Bliźniak, Ł. Łuczewski, and K. Lamperska, “2d and 3d cell cultures—a comparison of different types of cancer cell cultures,” *Archives of Medical Science*, vol. 14, no. 4, pp. 910–919, 2018.
- [60] K. Wierzchowski and M. Pilarek, “Microcarrier-supported culture of chondrocytes in continuously rocked disposable bioreactor,” in *Bioreactors in Stem Cell Biology: Methods and Protocols*. Springer, 2021, pp. 145–156.
- [61] W. W. Chan, F. Yu, Q. B. Le, S. Chen, M. Yee, and D. Choudhury, “Towards biomanufacturing of cell-derived matrices,” *International Journal of Molecular Sciences*, vol. 22, no. 21, p. 11929, 2021.
- [62] M.-Z. Ismadi, K. Hourigan, and A. Fouras, “Experimental characterisation of fluid mechanics in a spinner flask bioreactor,” *Processes*, vol. 2, no. 4, pp. 753–772, 2014.
- [63] B. Ahata, T. Kan, B. Serefoglu Gun, Y. Tanyeri, B. Oktay, A. Oktay, and R. Cakir Koc, “Bioreactors for tissue engineering,” in *Biomaterials and Tissue Engineering*. Springer, 2023, pp. 259–303.
- [64] C. D. Roche, R. J. Brereton, A. W. Ashton, C. Jackson, and C. Gentile, “Current challenges in three-dimensional bioprinting heart tissues for cardiac surgery,” *European Journal of Cardio-Thoracic Surgery*, vol. 58, no. 3, pp. 500–510, 2020.

- [65] D. Chimene, K. K. Lennox, R. R. Kaunas, and A. K. Gaharwar, “Advanced bioinks for 3d printing: a materials science perspective,” *Annals of biomedical engineering*, vol. 44, no. 6, pp. 2090–2102, 2016.
- [66] M. Rothbauer, C. Eilenberger, S. Spitz, B. E. Bachmann, S. R. Kratz, E. I. Reihls, R. Windhager, S. Toegel, and P. Ertl, “Recent advances in additive manufacturing and 3d bioprinting for organs-on-a-chip and microphysiological systems,” *Frontiers in Bioengineering and Biotechnology*, vol. 10, p. 837087, 2022.
- [67] F. R. de Gruijl, H. J. van Kranen, and L. H. Mullenders, “Uv-induced dna damage, repair, mutations and oncogenic pathways in skin cancer,” *Journal of Photochemistry and Photobiology B: Biology*, vol. 63, no. 1-3, pp. 19–27, 2001.
- [68] Z. Wang, R. Abdulla, B. Parker, R. Samanipour, S. Ghosh, and K. Kim, “A simple and high-resolution stereolithography-based 3d bioprinting system using visible light crosslinkable bioinks,” *Biofabrication*, vol. 7, no. 4, p. 045009, 2015.
- [69] V. B. Morris, S. Nimbalkar, M. Younesi, P. McClellan, and O. Akkus, “Mechanical properties, cytocompatibility and manufacturability of chitosan: Pegda hybrid-gel scaffolds by stereolithography,” *Annals of biomedical engineering*, vol. 45, no. 1, pp. 286–296, 2017.
- [70] Y. Gong, Z. Bi, X. Bian, A. Ge, J. He, W. Li, H. Shao, G. Chen, and X. Zhang, “Study on linear bio-structure print process based on alginate bio-ink in 3d bio-fabrication,” *Bio-Design and Manufacturing*, vol. 3, no. 2, pp. 109–121, 2020.
- [71] I. Matai, G. Kaur, A. Seyedsalehi, A. McClinton, and C. T. Laurencin, “Progress in 3d bioprinting technology for tissue/organ regenerative engineering,” *Biomaterials*, vol. 226, p. 119536, 2020.

- [72] S. Ji and M. Guvendiren, “Recent advances in bioink design for 3d bioprinting of tissues and organs,” *Frontiers in bioengineering and biotechnology*, vol. 5, p. 23, 2017.
- [73] F. J. Muzzio, M. M. Alvarez, S. Cerbelli, M. Giona, and A. Adrover, “The intermaterial area density generated by time-and spatially periodic 2d chaotic flows,” *Chemical Engineering Science*, vol. 55, no. 8, pp. 1497–1508, 2000.
- [74] J. Groll, J. A. Burdick, D.-W. Cho, B. Derby, M. Gelinsky, S. C. Heilshorn, T. Juengst, J. Malda, V. A. Mironov, K. Nakayama *et al.*, “A definition of bioinks and their distinction from biomaterial inks,” *Biofabrication*, vol. 11, no. 1, p. 013001, 2018.
- [75] S. Vanaei, M. Parizi, F. Salemizadehparizi, and H. Vanaei, “An overview on materials and techniques in 3d bioprinting toward biomedical application,” *Engineered Regeneration*, vol. 2, pp. 1–18, 2021.
- [76] M. Hospodiuk, M. Dey, D. Sosnoski, and I. T. Ozbolat, “The bioink: A comprehensive review on bioprintable materials,” *Biotechnology advances*, vol. 35, no. 2, pp. 217–239, 2017.
- [77] A. Fritschen, M. Acedo Mestre, S. Scholpp, and A. Blaeser, “Influence of the physico-chemical bioink composition on the printability and cell biological properties in 3d-bioprinting of a liver tumor cell line,” *Frontiers in Bioengineering and Biotechnology*, vol. 11, p. 1093101, 2023.
- [78] H. Yin, M. Zhu, Y. Wang, L. Luo, Q. Ye, and B. H. Lee, “Physical properties and cellular responses of gelatin methacryloyl bulk hydrogels and highly ordered porous hydrogels,” *Frontiers in Soft Matter*, vol. 2, p. 1101680, 2023.
- [79] K. Yue, G. Trujillo-de Santiago, M. M. Alvarez, A. Tamayol, N. Annabi, and A. Khademhosseini, “Synthesis, properties, and biomedical applications of

- gelatin methacryloyl (gelma) hydrogels,” *Biomaterials*, vol. 73, pp. 254–271, 2015.
- [80] S. Bupphathong, C. Quiroz, W. Huang, P.-F. Chung, H.-Y. Tao, and C.-H. Lin, “Gelatin methacrylate hydrogel for tissue engineering applications—a review on material modifications,” *Pharmaceuticals*, vol. 15, no. 2, p. 171, 2022.
- [81] S. Maharjan, J. Alva, C. Cámara, A. G. Rubio, D. Hernández, C. Delavaux, E. Correa, M. D. Romo, D. Bonilla, M. L. Santiago *et al.*, “Symbiotic photosynthetic oxygenation within 3d-bioprinted vascularized tissues,” *Matter*, vol. 4, no. 1, pp. 217–240, 2021.
- [82] M. Yoshida, H. Iwase, and T. Shikata, “Conformation and structure of hydroxyethyl cellulose ether with a wide range of average molar masses in aqueous solutions,” *Polymers*, vol. 14, no. 21, p. 4532, 2022.
- [83] K. Al Azzam, “A novel and simple dynamic coating capillary electrophoresis method for the chiral separation and quantification of mitoglinide enantiomers using hydroxyethyl cellulose as a dynamic coating agent,” *Die Pharmazie-An International Journal of Pharmaceutical Sciences*, vol. 77, no. 3-4, pp. 95–102, 2022.
- [84] M. Samandari, J. Quint, A. Rodríguez-delaRosa, I. Sinha, O. Pourquié, and A. Tamayol, “Bioinks and bioprinting strategies for skeletal muscle tissue engineering,” *Advanced Materials*, vol. 34, no. 12, p. 2105883, 2022.
- [85] H. Hecht and S. Srebnik, “Structural characterization of sodium alginate and calcium alginate,” *Biomacromolecules*, vol. 17, no. 6, pp. 2160–2167, 2016.
- [86] M. Efentakis and G. Buckton, “The effect of erosion and swelling on the dissolution of theophylline from low and high viscosity sodium alginate matrices,” *Pharmaceutical development and technology*, vol. 7, no. 1, pp. 69–77, 2002.

- [87] A. Homayouni, M. R. Ehsani, A. Azizi, M. S. Yarmand, and H. Razavi, “Effect of lecithin and calcium chloride solution on the microencapsulation process yield of calcium alginate beads,” *Iranian Polymer Journal*, 2007.
- [88] L. Lu, S. Yuan, J. Wang, Y. Shen, S. Deng, L. Xie, and Q. Yang, “The formation mechanism of hydrogels,” *Current stem cell research & therapy*, vol. 13, no. 7, pp. 490–496, 2018.
- [89] N. Joshi, K. Rawat, and H. Bohidar, “Influence of structure, charge, and concentration on the pectin–calcium–surfactant complexes,” *The Journal of Physical Chemistry B*, vol. 120, no. 18, pp. 4249–4257, 2016.
- [90] X. Bi and A. Liang, “In situ-forming cross-linking hydrogel systems: chemistry and biomedical applications,” *Emerging concepts in analysis and applications of hydrogels*, vol. 86, pp. 541–547, 2016.
- [91] A. Zennifer, S. Manivannan, S. Sethuraman, S. G. Kumbar, and D. Sundaramurthi, “3d bioprinting and photocrosslinking: emerging strategies & future perspectives,” *Biomaterials Advances*, vol. 134, p. 112576, 2022.
- [92] L. Shao, Q. Gao, C. Xie, J. Fu, M. Xiang, Z. Liu, L. Xiang, and Y. He, “Sacrificial microgel-laden bioink-enabled 3d bioprinting of mesoscale pore networks,” *Bio-design and manufacturing*, vol. 3, no. 1, pp. 30–39, 2020.
- [93] G. K. Batchelor, *An introduction to fluid dynamics*. Cambridge university press, 2000.
- [94] K. R. Symon, “Mechanics. addison,” 1971.
- [95] Y. Cengel and J. Cimbala, *Ebook: Fluid mechanics fundamentals and applications (si units)*. McGraw Hill, 2013.
- [96] A. Sommerfeld, *Ein beitrag zur hydrodynamischen erklärung der turbulenten fluessigkeitsbewegungen*. Elsevier, 1909.


- [97] D. Li, *Encyclopedia of microfluidics and nanofluidics*. Springer Science & Business Media, 2008.
- [98] H. Aref, J. R. Blake, M. Budišić, S. S. Cardoso, J. H. Cartwright, H. J. Clercx, K. El Omari, U. Feudel, R. Golestanian, E. Guillard *et al.*, “Frontiers of chaotic advection,” *Reviews of Modern Physics*, vol. 89, no. 2, p. 025007, 2017.
- [99] H. Aref, “Chaotic advection of fluid particles,” *Philosophical Transactions of the Royal Society of London. Series A: Physical and Engineering Sciences*, vol. 333, no. 1631, pp. 273–288, 1990.
- [100] S. Wiggins and J. M. Ottino, “Foundations of chaotic mixing,” *Philosophical Transactions of the Royal Society of London. Series A: Mathematical, Physical and Engineering Sciences*, vol. 362, no. 1818, pp. 937–970, 2004.
- [101] C. F. Ceballos-Gonzalez, E. J. Bolivar-Monsalve, D. A. Quevedo-Moreno, L. L. Lam-Aguilar, K. I. Borrayo-Montano, J. F. Yee-de Leon, Y. S. Zhang, M. M. Alvarez, and G. Trujillo-de Santiago, “High-throughput and continuous chaotic bioprinting of spatially controlled bacterial microcosms,” *ACS Biomaterials Science & Engineering*, vol. 7, no. 6, pp. 2408–2419, 2021.
- [102] C. F. C. GONZÁLEZ, E. J. B. MONSALVE, D. Dean, C. Rodriguez, M. M. Alvarez, and G. T. DE SANTIAGO, “Methods and systems for cell culture,” Sep. 15 2022, uS Patent App. 17/635,658.
- [103] C. F. Ceballos-Gonzalez, E. J. Bolivar-Monsalve, D. A. Quevedo-Moreno, C. Chavez-Madero, S. Velasquez-Marin, L. L. Lam-Aguilar, O. E. Solis-Perez, A. Cantoral-Sanchez, M. Neher, E. Yzar-Garcia *et al.*, “Plug-and-play multimaterial chaotic printing/bioprinting to produce radial and axial micropatterns in hydrogel filaments,” *Advanced Materials Technologies*, vol. 8, no. 17, p. 2202208, 2023.

- [104] A. Zaheri, J. S. Fenner, B. P. Russell, D. Restrepo, M. Daly, D. Wang, C. Hayashi, M. A. Meyers, P. D. Zavattieri, and H. D. Espinosa, “Revealing the mechanics of helicoidal composites through additive manufacturing and beetle developmental stage analysis,” *Advanced Functional Materials*, vol. 28, no. 33, p. 1803073, 2018.
- [105] E. Skliutas, M. Lebedevaite, S. Kasetaitė, S. Rekštytė, S. Lileikis, J. Ostrauskaite, and M. Malinauskas, “A bio-based resin for a multi-scale optical 3d printing,” *Scientific reports*, vol. 10, no. 1, pp. 1–9, 2020.
- [106] P. Shi, A. Laude, and W. Y. Yeong, “Investigation of cell viability and morphology in 3d bio-printed alginate constructs with tunable stiffness,” *Journal of Biomedical Materials Research Part A*, vol. 105, no. 4, pp. 1009–1018, 2017.
- [107] G. F. El Fawal, M. M. Abu-Serie, M. A. Hassan, and M. S. Elnouby, “Hydroxyethyl cellulose hydrogel for wound dressing: Fabrication, characterization and in vitro evaluation,” *International journal of biological macromolecules*, vol. 111, pp. 649–659, 2018.
- [108] C. G. Simon Jr, M. J. Yaszemski, A. Ratcliffe, P. Tomlins, R. Luginbuehl, and J. A. Tesk, “Astm international workshop on standards and measurements for tissue engineering scaffolds,” *Journal of Biomedical Materials Research Part B: Applied Biomaterials*, vol. 103, no. 5, pp. 949–959, 2015.
- [109] T. Yu, Z. Zhang, S. Song, Y. Bai, and D. Wu, “Tensile and flexural behaviors of additively manufactured continuous carbon fiber-reinforced polymer composites,” *Composite Structures*, vol. 225, p. 111147, 2019.
- [110] A. M. Collinsworth, S. Zhang, W. E. Kraus, and G. A. Truskey, “Apparent elastic modulus and hysteresis of skeletal muscle cells throughout differentiation,” *American Journal of Physiology-Cell Physiology*, vol. 283, no. 4, pp. C1219–C1227, 2002.

- [111] W. Fan, L. R. Jensen, Y. Dong, A. J. Deloria, B. Xing, D. Yu, and M. M. Smedskjaer, “Highly stretchable, swelling-resistant, self-healed, and biocompatible dual-reinforced double polymer network hydrogels,” *ACS Applied Bio Materials*, vol. 6, no. 1, pp. 228–237, 2022.
- [112] J. E. Pérez-Cortez, V. H. Sánchez-Rodríguez, S. Gallegos-Martínez, C. Chuck-Hernández, C. A. Rodriguez, M. M. Álvarez, G. Trujillo-de Santiago, E. Vázquez-Lepe, and J. I. Martínez-López, “Low-cost light-based gelma 3d bioprinting via retrofitting: Manufacturability test and cell culture assessment,” *Micromachines*, vol. 14, no. 1, p. 55, 2022.

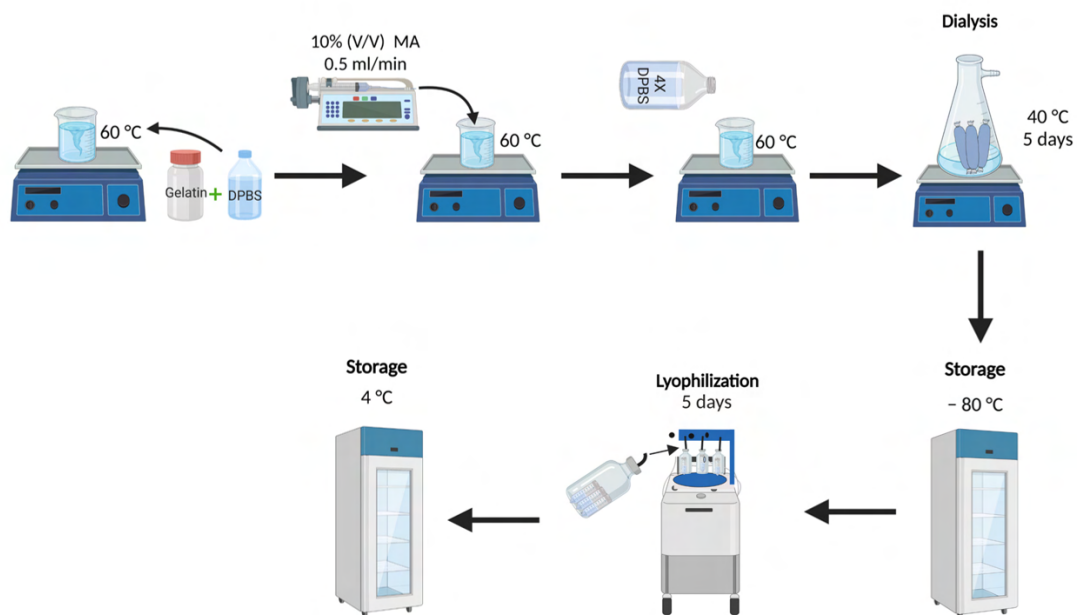
APPENDICES

Appendix 1 - Technical Specifications of the Form 3+ 3D Printer

Printer	 Form 3+
Technology	Low Force Stereolithography (LFS) TM
XY Resolution^a	25 microns
Laser Spot Size	85 microns
Laser Power	One 250 mW laser
Build Volume (W x D x H)	14.5 × 14.5 × 19.3 cm 5.7 × 5.7 × 7.6 in
Layer Thickness^b	25 – 300 microns .001 – .012 in

Obtained from <https://formlabs.com/3d-printers/form-3/tech-specs/>

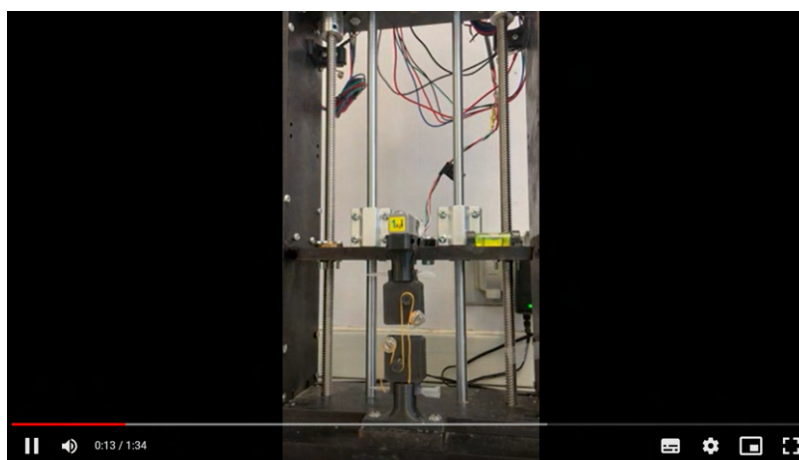
Appendix 2 - Protocol for Lyophilized GelMA Preparation



This image was adapted from [112]

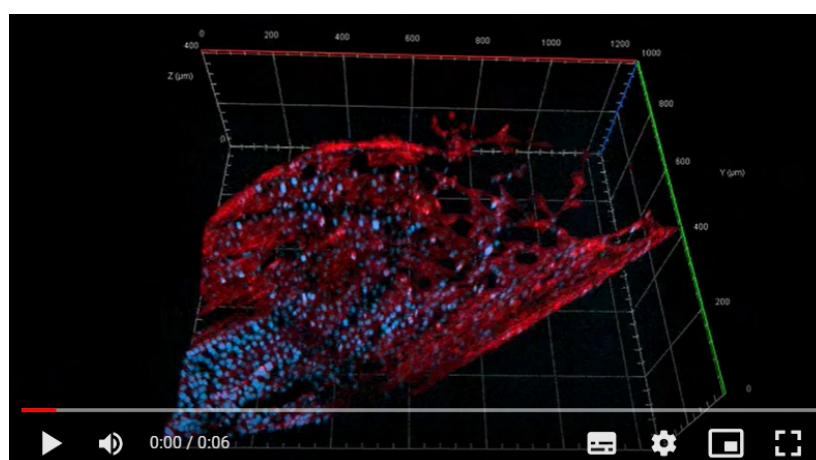
Appendix 3 - Video of a Tensile Test with a hydrogel fiber as a sample

[Click to watch full video](#)



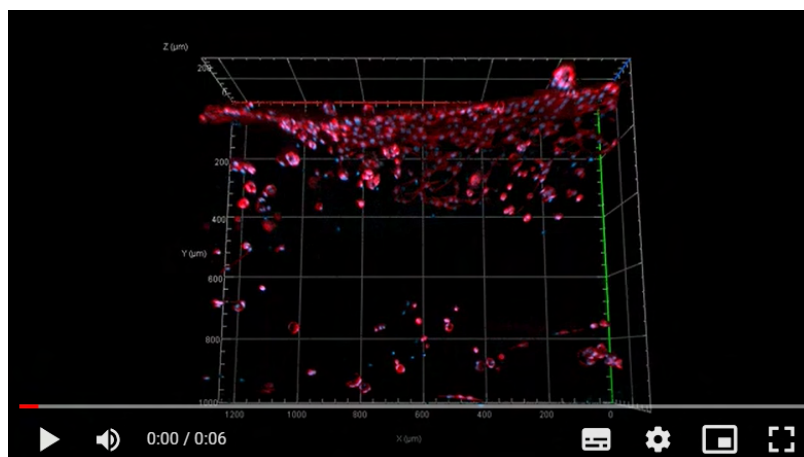
Appendix 4 - Video of Actin/DAPI staining of Solid Fibers in Static Culture (Day 14)

[Click to watch full video](#)



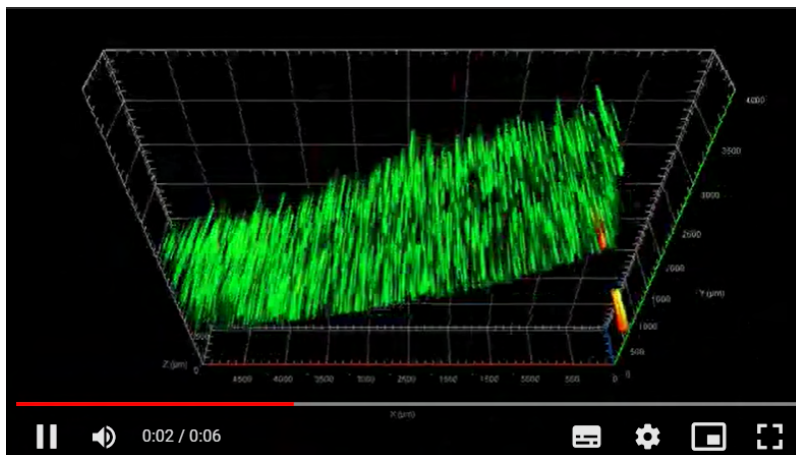
Appendix 5 - Video of Actin/DAPI staining of Hollow Fibers in Static Culture (Day 14)

[Click to watch full video](#)



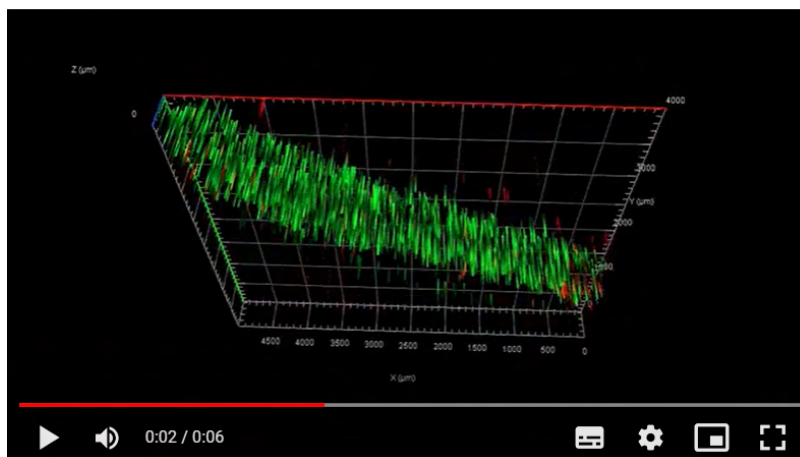
Appendix 6 - Video of Live/Dead Assay of Solid Fibers in Culture under Agitation (Day 07)

[Click to watch full video](#)



Appendix 7 - Video of Live/Dead Assay of Hollow Fibers in Culture under Agitation (Day 07)

[Click to watch full video](#)



Appendix 9 - Budget

	Supplier	Unit	Amount per unit	Required Units	Unit Cost (S/.)	Total Cost (S/.)	Unit Cost (USD)	Total Cost (USD)
BIOLOGICALS								
Mouse Myoblasts (C2C12 cell line)	ATCC	1 vial	1	1	2044,98	2044,98	541	541
REACTIVES								
Sodium alginate (high viscosity)	Sigma-Aldrich	1 bottle	1 kg	1	677,7162	677,7162	179,29	179,29
Sodium alginate (low viscosity)	Sigma-Aldrich	1 bottle	100 g	1	230,9202	230,9202	61,09	61,09
Hydroxyethylcellulose	Sigma-Aldrich	1 bottle	100 g	1	184,9932	184,9932	48,94	48,94
Calcium Chloride	Sigma-Aldrich	1 bottle	100 g	1	263,277	263,277	69,65	69,65
Lithium phenyl-2,4,6-trimethylbenzoylphosphinate (LAP)	CELLINK	1 bottle	1 g	1	567,3402	567,3402	150,09	150,09
Gelatin from porcine skin	Sigma-Aldrich	1 bottle	500 g	1	663,2388	663,2388	175,46	175,46
Methacrylic anhydride (MA)	Sigma-Aldrich	1 bottle	100 mL	1	218,1438	218,1438	57,71	57,71
Sodium citrate tribasic	Sigma-Aldrich	1 bottle	25 g	1	120,2418	120,2418	31,81	31,81
Trypsin (0.25)	Gibco	1 bottle	500 mL	1	314,685	314,685	83,25	83,25
PBS (10X)	Gibco	1 bottle	500 mL	1	261,0846	261,0846	69,07	69,07
DPBS	Gibco	1 bottle	500 mL	1	132,4134	132,4134	35,03	35,03
Antibiotic/Antimycotic (100X)	Gibco	1 bottle	100 mL	1	266,0364	266,0364	70,38	70,38
Fetal bovine serum	Gibco	1 bottle	50 mL	1	283,7268	283,7268	75,06	75,06
DMEM high glucose	Sigma-Aldrich	1 bottle	100 g	2	189,756	379,512	50,2	100,4
Sodium Pyruvate	Fisher Bioreagents	1 bottle	100 g	1	110,8674	110,8674	29,33	29,33
Live/Dead Cell imaging kits	Invitrogen	1 box	4x1mL vials	1	509,544	509,544	134,8	134,8
Phalloidin (iFluor 647)	Abcam	1 vial	100 mL	1	869,4	869,4	230	230
DAPI	Sigma-Aldrich	1 vial	1 mg	1	54,3186	54,3186	14,37	14,37
Paraformaldehyde	Sigma-Aldrich	1 vial	5 g	1	117,8604	117,8604	31,18	31,18
MATERIALS								
Syringes - 5 mL	BD Plastipak	1 box	100 units	1	102,4758	102,4758	27,11	27,11
Syringes - 10 mL	BD Plastipak	1 box	100 units	1	131,8842	131,8842	34,89	34,89
Micropipette tips - 1 ml	LUOXINMAO	1 package	500 units	1	113,3622	113,3622	29,99	29,99
Micropipette tips - 200 µL	LUOXINMAO	1 package	500 units	1	86,9022	86,9022	22,99	22,99
Micropipette tips - 10 µL	LUOXINMAO	1 package	500 units	1	56,6622	56,6622	14,99	14,99
Silicone Tubes (ID=2mm)	Uxcell	1 piece	1 meter	1	20,7522	20,7522	5,49	5,49
Falcon tubes - 15 mL	Corning	1 package	50 units	1	79,758	79,758	21,1	21,1
Falcon tubes - 50 mL	Corning	1 package	50 units	1	75,4866	75,4866	19,97	19,97
Eppendorf Tubes 1 mL	Eppendorf	1 package	50 units	1	23,5116	23,5116	6,22	6,22
Serological pipettes - 5 mL	CELLTREAT	1 package	200 units	1	279,72	279,72	74	74
T75 Flasks	Corning	1 package	50 units	1	533,3769	533,3769	141,105	141,105
Well Plates (12-well)	Corning	1 package	10 units	1	160,6122	160,6122	42,49	42,49
Filters (pore diameter=0.45 µm)	Whatman	1 box	45 units	1	337,554	337,554	89,3	89,3
TOTAL (S/.)						9934,8039	TOTAL (USD)	2628,255